On the Nordic Overturning Circulation

Dissertation
zur Erlangung des Doktorgrades
der Naturwissenschaften im Department
Geowissenschaften
der Universität Hamburg

vorgelegt von

Gunnar Voet

aus

Starnberg

Hamburg

2010

Als Dissertation angenommen vom Department Geowissenschaften der Universität Hamburg

Auf Grund der Gutachten von Prof. Dr. Detlef Quadfasel
und Prof. Dr. Jan Backhaus

Hamburg, den 29.06.2010

Prof. Dr. Jürgen Oßenbrügge
Leiter des Departments für Geowissenschaften

Abstract

This thesis consists of four studies that aim at understanding processes relevant for the Nordic Overturning Circulation. These processes are (1) the Nordic Seas circulation associated with water mass transformation, (2) the dense overflows across the Greenland-Scotland Ridge and (3) entrainment associated with the overflow plumes south of the ridge.

Trajectories of Argo floats, drifting at mid-depth in the Nordic Seas, are analysed to determine the pattern, strength and variability of the regional circulation. The mid-depth circulation is strongly coupled to the structure of the bottom topography of the four major basins and of the Nordic Seas as a whole. It is cyclonic, both on the large scale and on the basin scale, with weak flow ($< 1\,\mathrm{cm/s}$) in the interior of the basins and somewhat stronger flow (up to $5\,\mathrm{cm/s}$) at their rims. Wind forcing is shown to be the dominant driving force for the seasonal variability of the gyres in the Greenland Basin and the Norwegian Basin.

Using hydraulic control theory applied to historical hydrographic data, a dense water transport across the shallow Iceland-Faroe Ridge of $1 \pm 0.6 \times 10^6\,\mathrm{m^3/s}$ is estimated. Half of this overflow passes through the western valley of the ridge at the Icelandic continental slope while the other half crosses the ridge through its eastern gaps. For the western valley, an independent overflow transport estimated from recent mooring data is $0.5 \pm 0.3 \times 10^6\,\mathrm{m^3/s}$. The agreement of the two results for the western valley indicates that the dense overflows across the shallower parts of the Greenland-Scotland Ridge are indeed hydraulically controlled.

Two studies dedicated to mixing and stirring provide a coherent description of entrainment in the dense overflow plumes downstream of the Greenland-Scotland Ridge. (1) Stirring by meso-scale eddies causes lateral heat fluxes that can explain the warming of the Denmark Strait overflow plume in a region 200 km from the sill and beyond. (2) Using direct turbulence measurements, intense mixing and enhanced turbulent dissipation at the upper plume interface is observed in the Faroe Bank Channel overflow plume in a region between the sill and 120 km downstream. The two studies, together with previous entrainment studies, suggest two different entrainment regimes for the overflow plumes. Strong vertical mixing leads to entrainment close to the sill during high plume velocities while lateral stirring through meso-scale eddies causes entrainment further downstream.

Results of this thesis contribute to ongoing and upcoming studies of the interannual to decadal variability of the Nordic Meridional Overturning Circulation.

Zusammenfassung

Diese Arbeit besteht aus vier Studien, die zum Verständnis von Prozessen mit Relevanz für die Nordische Umwälzzirkulation beitragen sollen. Diese Prozesse sind (1) die Zirkulation im Europäischen Nordmeer, die eng verknüpft ist mit der Wassermassentransformation, (2) die Überströmung des Grönland-Schottland-Rückens von Wasser mit hoher Dichte sowie (3) die turbulente Vermischung in den Overflow-Plumes südlich des Rückens.

Trajektorien von Argo-Floats, die in mittleren Tiefen des Europäischen Nordmeers driften, werden im Hinblick auf Muster, Stärke und Variabilität der regionalen Zirkulation analysiert. Die Zirkulation in mittleren Tiefen ist stark an die Struktur der einzelnen Becken sowie des gesamten Europäischen Nordmeers gekoppelt. Sie ist sowohl auf großräumiger Skala als auch auf der Becken-Skala zyklonal mit schwacher Strömung im Innern der Becken ($< 1\,\mathrm{cm/s}$) und etwas stärkerer Strömung (bis zu $5\,\mathrm{cm/s}$) an deren Rändern. Als antreibende Kraft für einen beobachteten saisonalen Zyklus in der Stärke der Beckenwirbel im Grönland- und Norwegenbecken stellt sich der Wind heraus.

Ein Transport dichten Wassers über den flachen Island-Faroe-Rücken von $1\pm0.6\times10^6\,\mathrm{m^3/s}$ wird durch die Anwendung der Theorie hydraulischer Kontrolle auf historische hydrographische Daten abgeschätzt. Eine Hälfte des so bestimmten Transports strömt durch einen Einschnitt im Rücken nahe des Isländischen Kontinentalschelfs, während die andere Hälfte den Rücken durch tiefere Passagen im östlichen Teil quert. Aus kürzlich gewonnenen Verankerungsdaten kann für den westlichen Einschnitt eine weitere Transportabschätzung von $0.5\pm0.3\times10^6\,\mathrm{m^3/s}$ gewonnen werden. Die Übereinstimmung der beiden Ergebnisse für den westlichen Einschnitt deutet an, dass die Überströmung der flacheren Teile des Grönland-Schottland-Rückens in der Tat hydraulischer Kontrolle unterliegt.

Zwei Studien, die sich mit Vermischung auf unterschiedlichen Größenskalen beschäftigen, liefern eine schlüssige Beschreibung der turbulenten Vermischung in den Overflow-Plumes stromabwärts des Grönland-Schottland-Rückens. (1) Verrühren durch meso-skalige Wirbel führt zu lateralen Wärmeflüssen, die die Erwärmung der Overflow-Plume aus der Dänemarkstrasse im Bereich von 200 km und weiter stromabwärts der Schwelle erklären können. (2) Anhand von direkten Turbulenzmessungen werden intensive Vermischung und starke turbulente Dissipation an der oberen Plume-Grenzschicht der Overflow-Plume aus dem Färöer-Bank-Kanal im Bereich zwischen der Schwelle und 120 km stromabwärts beobachtet. Die beiden vorliegenden Arbeiten deuten, zusammen mit vorherigen Studien turbulenter Vermischung, auf zwei unterschiedliche Regime der turbulenten Vermischung in den Overflow-Plumes hin. Starke vertikale Vermischung findet nahe der

Schwellen während hoher Geschwindigkeiten der Plumes statt, während laterales Rühren durch mesoskalige Wirbel turbulente Vermischung weiter stromabwärts der Schwellen verursacht.

Die Ergebnisse dieser Arbeit tragen zu laufenden und kommenden Studien zur Variabilität der Nordischen Meridionalen Umwälzzirkulation auf interannualen bis dekadischen Zeitskalen bei.

Contents

Chapter 1

Summary

1.1 Motivation

The oceanic Meridional Overturning Circulation is an important element of the world's climate system that strongly influences the European climate. Projections from computer models simulating ocean and atmosphere for a future climate affected by increased anthropogenic greenhouse gas emissions predict a weakening of the Meridional Overturning Circulation of the North Atlantic, especially of its branch into the Nordic Seas. As global computer simulations still have coarse grids compared to the processes that affect the Meridional Overturning Circulation, a better understanding of these processes is crucial for improved climate predictions and the validation of these. This work aims at closing gaps in the understanding of processes associated with the Nordic Overturning Circulation.

The Nordic Seas are a site for the transformation of the water masses of the surface branch to the deep branch of the Meridional Overturning Circulation. The identification of important areas for this transformation within the Nordic Seas is currently an area of intense research efforts. Using position data of autonomous profiling floats, the mid-depth circulation of the Nordic Seas, its variability and forcing mechanisms are analysed in this thesis. This helps to understand the redistribution of different water masses within the Nordic Seas.

The export of dense water from the Nordic Seas is restricted by the shallow Greenland-Scotland Ridge. The overflows of dense water across the deeper passages in this ridge are well understood, monitored and modeled. In contrast, the part of the overflow across the shallow and wide opening between Iceland and the Faroe Islands is less investigated so far. Using recently recorded current data and historical hydrographic data, an estimate for the mean overflow across the Iceland-Faroe Ridge and its seasonal varia-

bility is obtained in this thesis. This aims at closing a gap in the budget of volume transport exchanges between the Nordic Seas and the North Atlantic, leading to better understanding and detectability of changes in the strength of the Nordic branch of the Meridional Overturning Circulation.

The dense water that has overflowed the Greenland-Scotland Ridge sinks to greater depths of the North Atlantic due to its high density compared to the ambient water masses. During this descent, the overflow plumes are subject to vigorous entrainment that changes the water mass properties and increases the volume transport of the dense current. Two studies within this work are dedicated to analysing the importance of turbulent vertical mixing and horizontal stirring by meso-scale eddies for the entrainment into the dense plumes. A better understanding of these processes may help parameterising them into coarse computer models, allowing for an improved representation of the Meridional Overturning Circulation in the models.

1.2 The Meridional Overturning Circulation and its branch into the Nordic Seas

The climate over northern Europe is exceptionally warm regarding its position at relatively high latitudes. Mean surface temperatures in this region are 5 to 10 K higher than the zonal mean (Figure 1.1). The main reason for this high temperature anomaly are baroclinic eddies in the atmosphere leading to large meridional heat transports as well as the combination of prevailing westerly winds at these latitudes and the large heat capacity of the ocean. Nevertheless, the oceanic circulation also plays an important role. The northward heat transport by ocean currents associated with the surface component of the Meridional Overturning Circulation helps to keep large areas of the northern North Atlantic free from ice in winter (Seager et al., 2002). The heat stored in the water can thus be released to the atmosphere in winter, thereby tempering the climate in winter over northern Europe. The Meridional Overturning Circulation thus is an important factor for living conditions here. Fundamental knowledge about driving mechanisms and possible future changes of the Meridional Overturning Circulation is therefore not only exciting in a pure scientific sense but also vital for human beings living in this region.

The main driver for the circulation of ocean and atmosphere is the energy input by the sun received as solar radiation. The spherical shape of the earth leads to a non-uniform distribution of the incoming solar radiation. The maximum of the solar energy is received around the equator, the minimum at the poles. The radiation of energy from the earth into space also has its maximum around the equator as it is proportional to the fourth power of the earth surface temperature, but the distribution with latitude is less variable than for the incoming solar radiation. Together, incoming and outgoing radiation lead to a net energy budget that results in a surplus of energy at low latitudes and a loss of energy at the poles (Figure 1.2). This meridional energy gradient leads to poleward heat transports in ocean and atmosphere which, in a steady state of the earth climate, balance the unequal meridional distribution of the radiation budget.

The density fluxes at the interface between ocean and atmosphere, generated by the incoming solar energy, create driving forces for the Thermohaline Circulation of the ocean. Cooling and sea ice formation at high latitudes transform surface water with relatively low density into intermediate and deep waters with high density. Mixing in the ocean interior, equatorwards from the deep water formation sites, and upwelling in the Southern Ocean, brings water with low density to greater depths. This leads to a density gradient between poles and equator at depth that results in a meridional current along the gradient (Stommel, 1961). The current at depth is bal-

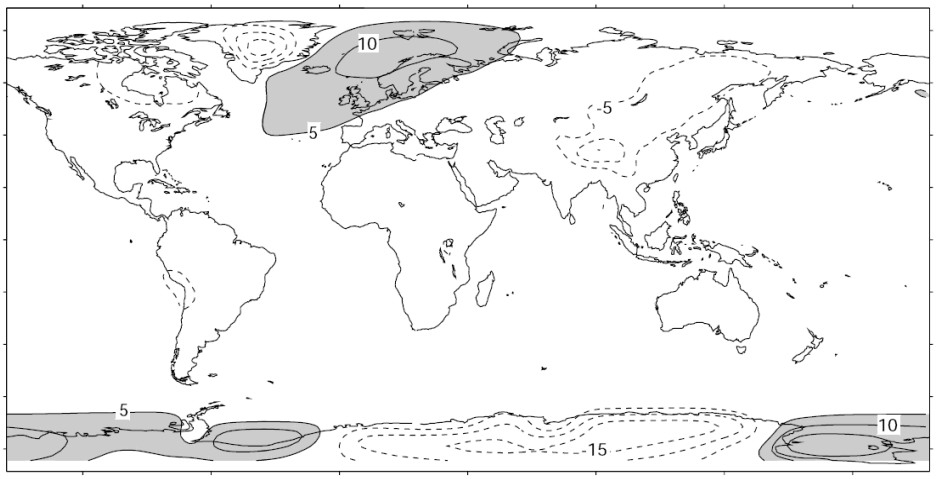

Figure 1.1: *Mean reginal surface air temperature anomalies relative to the zonal mean computed from NCAR air temperature climatology (from* Rahmstorf and Ganapolski*, 1999). The surface air temperature over northern Europe is 5 to 10 K warmer than the zonal average.*

anced by a flow of water with low density from low to high latitudes. These currents make up an overturning cell that leads to the large heat transports in the ocean mentioned above.

When measuring the overturning cell in the ocean, it cannot be distinguished between the purely density driven part of the overturning circulation, the Thermohaline Circulation, and the contribution of the wind, which induces mixing and upwelling that are essential for the maintenance of the overturning circulation. These are two different forces driving one observable circulation (Rahmstorf, 2003). The circulation integrated zonally over a whole ocean basin is called the Meridional Overturning Circulation (MOC).

The poleward oceanic heat transport accomplished by the MOC in the North Atlantic at 24°N is 1.3 PW (Ganachaud and Wunsch, 2000). This is much higher than in the North Pacific where the poleward oceanic heat transport at approximately the same latitude is only 0.5 PW. The reason for this difference is the much stronger mass transport associated with the MOC in the Atlantic due to enhanced water mass transformation between upper and lower part of the MOC as will be explained below.

The anthropogenic emission of greenhouse gases, leading to increasing levels of greenhouse gases in the atmosphere, induces a change in the forcing of atmosphere and ocean (Solomon et al., 2007). Both, globally and locally, the mean state and the variability of climate variables like temperature, precipitation, land and sea ice cover, sea level, ocean circulation and others are already changing or expected to change within this century. Climate

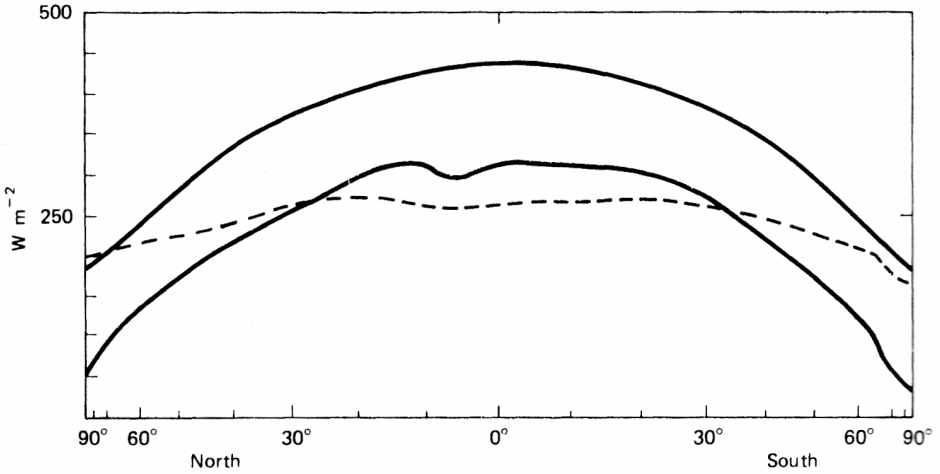

Figure 1.2: *Radiation balance of the earth (from* Gill, *1982). The upper solid curve gives the average incoming flux of solar radiation at the outer atmosphere. The lower solid curve shows the average amount of solar energy absorbed. The dashed line gives the average outgoing radiation. The misfit between the lower solid and the dashed line thus gives the average meridional imbalance of the global radiation budget. The x-axis is linear in the sine of the latitude to account for the decreasing area of zonal bands with increasing latitude.*

models, simulating the earths climate with a coupled system of ocean and atmosphere, are used for climate projections to predict changes in the mean state and variability of climate variables like those mentioned afore. The models use different scenarios of the anthropogenic greenhouse gas emission for the climate projections to reflect potential emission changes.

According to these climate projections, it is very likely that the Atlantic Meridional Overturning Circulation (AMOC) will slow down during the course of the 21st century (Schmittner et al., 2005; Meehl et al., 2007). The predicted strength of the AMOC at 30°N in different climate models is shown in Figure 1.3. The latitude band of 30°N is chosen as the AMOC has its maximum at about this latitude. The range of the projections is rather large with some models showing a weakening that is only within the natural variability of the AMOC while others predict a weakening of over 50% relative to the mean AMOC between 1960 and 1990.

Figure 1.3 shows that the model results do not only differ in the projected reduction of the AMOC, but also in the present mean strength of the AMOC, ranging from about 12 Sv to more than 20 Sv ($1\,\mathrm{Sv} = 10^6\,\mathrm{m}^3/\mathrm{s}$), and in its variability. This points out the high uncertainty of the coupled ocean-atmosphere models regarding the AMOC. One reason for this uncertainty

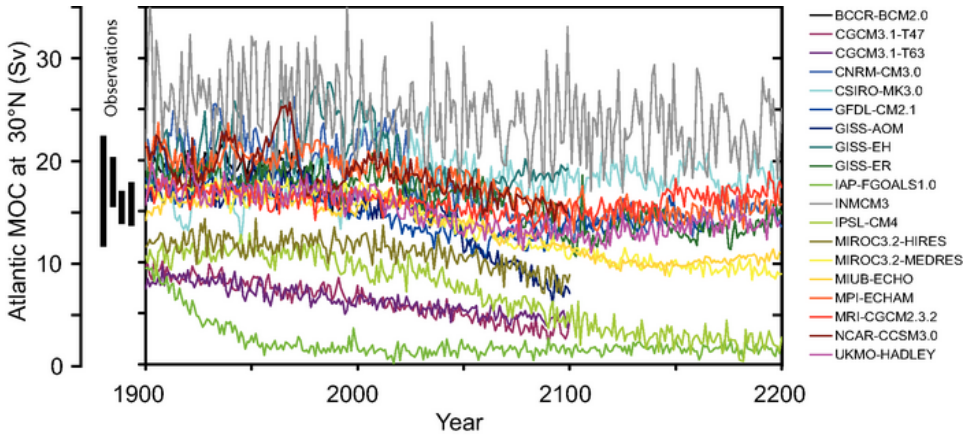

Figure 1.3: *Evolution of the strength of the Atlantic Meridional Overturning Circulation at 30°N in global climate projections. The strength of the overturning cell is given in Sverdrup ($1\,Sv = 10^6\ m^3/s$). The A1B emission scenario is used for the period 1999 to 2100. The scenario predicts increasing CO_2 emissions until around 2050 and decreasing CO_2 emissions after it. Some of the models continue the integration to year 2200 with the forcing held constant at the values of year 2100. Observationally based estimates of late-20th century MOC are shown as vertical bars on the left. Three simulations show a steady or rapid slow down of the MOC that is unrelated to the forcing; a few others have late-20th century simulated values that are inconsistent with observational estimates. Of the model simulations consistent with the late-20th century observational estimates, no simulation shows an increase in the AMOC during the 21st century; reductions range from indistinguishable within the simulated natural variability to over 50% relative to the 1960 to 1990 mean; and none of the models projects an abrupt transition to an off state of the AMOC. Figure and caption from* Meehl et al. *(2007), therein adapted from* Schmittner et al. *(2005) with additions.*

is the grid size of the models that, owing to computational limitations, is too large to resolve both small scale oceanic processes and local bottom topography. An example for small scale processes underrepresented in global climate models is the dense overflow across the Greenland-Scotland Ridge that will be discussed below. Measurements of the mean strength of the AMOC and its variability and the understanding of processes associated with the AMOC are thus crucial for the validation of the climate models to make their climate predictions more reliable.

In the past, the strength of the AMOC was estimated from hydrographic observations along transects. Bryden et al. (2005) calculated a weakening of the AMOC on decadal time scales based on five hydrographic sections across the North Atlantic within 50 years. The estimates have large errors,

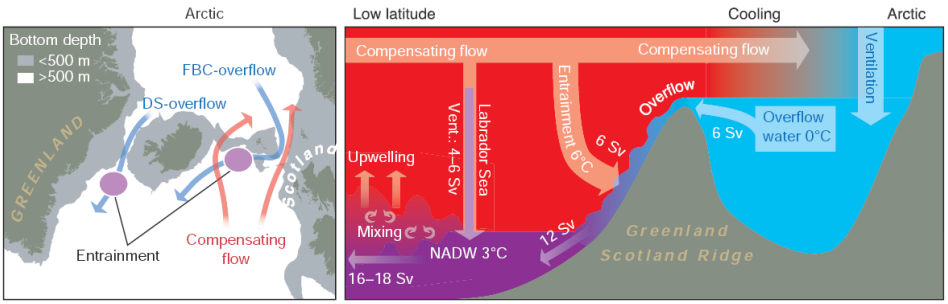

Figure 1.4: *Scheme of the Nordic Overturning Circulation (from* Hansen et al.*, 2004). Temperatures given in °C and volume transports given in Sv are only approximate values. For a detailed description see text.*

already indicating the large variability of the overturning circulation. Stimulated by this reported reduction of the AMOC, a large scale mooring array was installed across the Atlantic Ocean at 26.5°N (Cunningham et al., 2007) to validate the results of Bryden et al. (2005). The strength of the overturning cell as estimated from 4-year-long mooring time series at 26.5°N is so far stable at 18.7±5.6 Sv. Thus, the variability of the AMOC on intra-annual time scales is large. This natural variability led to an aliasing effect in the few hydrographic transects used in the analysis of Bryden et al. (2005) and hence the decreasing mean strength of the AMOC may not exist in reality. A study by Baehr et al. (2007) shows that the variability of the AMOC leads to a detection time for changes in the strength of the AMOC of about 30 years. This long detection time scale in turn calls for improved modelling efforts to predict changes in the AMOC.

The overturning cell in the North Atlantic is stronger than in the Pacific because of the ventilation regions situated in the northern North Atlantic, the Labrador Sea and the Nordic Seas. These are two of only few spots on the globe where orographic and atmospheric conditions are favourable for the transformation of the poleward flowing surface water into dense water that returns equatorwards at depth.

While the Labrador Sea is connected to the abyssal North Atlantic without any topographic constraints, the Nordic Seas are separated from the North Atlantic to the south by the Greenland-Scotland Ridge. The branch of the AMOC into and out of the Nordic Seas has to pass over this ridge.

Figure 1.4 shows a scheme of the exchange flow across the Greenland-Scotland Ridge and illustrates the associated processes. The warm Atlantic water flows into the Nordic Seas where it gains density and sinks. The processes leading to the density increase, cooling at the surface amongst others, are collectively termed ventilation. The ventilation in the Nordic Seas sustains a reservoir of dense water that feeds the overflows through the

deeper passages of the Greenland-Scotland Ridge. After crossing the crest of the Greenland-Scotland Ridge, the dense water descends to the greater depths of the North Atlantic. During the descent, warm ambient water is entrained into the cold overflow plume. This leads to an increase in plume temperature and volume transport. On its way towards the equator the water ventilated in the Labrador Sea joins the overflow water from the Nordic Seas and together they make up the North Atlantic Deep Water. The final amount of dense water leaving the subpolar North Atlantic equatorwards at depth is 16 to 18 Sv. Ventilation in the Nordic Seas, entrainment into the sinking overflow plumes and dense water formation in the Labrador Sea each contribute with about 1/3 or 6 Sv to the production of North Atlantic Deep Water. As mentioned above, mixing and upwelling further south is needed to maintain the density gradient at depth.

In this dissertation I aim at contributing to the understanding of the processes that determine the strength of the Northern part of the AMOC:

Ventilation The water mass transformation is not studied explicitly here, but the circulation internal to the Nordic Seas (Voet et al., 2010). The understanding of the redistribution of water masses within the Nordic Seas is important for the detection of deep water formation sites and the dynamics and variability of the ventilation.

Overflows In contrast to the two main overflows through Denmark Strait and the Faroe Bank Channel, the overflow across the shallow Iceland-Faroe Ridge is not very well understood and measured so far. Previous studies suggest that it makes up for about 20% of the total overflow across the Greenland-Scotland Ridge, but were based on sparse measurements. A hitherto unpublished study gives a new estimate for the mean overflow across the Iceland-Faroe Ridge with a focus on its western part using hydraulic control theory for dense overflows (Section 1.4.2).

Entrainment The entrainment into the dense overflow plumes leads to a doubling of the overflow volume transport from the Nordic Seas and thereby accounts for about 30% of the final amount of dense water leaving the subpolar North Atlantic at depth. The small and meso-scale processes leading to entrainment have not been investigated in detail yet. Two studies regarding entrainment in the Denmark Strait overflow (Voet and Quadfasel, 2010) and the Faroe Bank Channel overflow (Fer et al., 2010) show the importance of horizontal stirring by meso-scale eddies and vertical turbulence for the entrainment.

The geographic areas of the studies presented in this work are shown in Figure 1.5 together with the bathymetry of the Nordic Seas. The Nordic

Seas are a marginal sea that is confined to the west by Greenland and to the east by Norway. It is connected to the Arctic in the north via the Fram Strait opening with a depth of ∼2600 m (all depth readings in this paragraph from Blindheim and Østerhus, 2005) and the much shallower Barents Sea opening. In the south it is separated from the abyssal North Atlantic by the Greenland-Scotland Ridge that stretches from Greenland over Iceland and the Faroe Islands to Scotland. The Greenland-Scotland Ridge has a mean depth of less than 500 m. The deepest openings through the Greenland-Scotland Ridge are the Faroe-Bank Channel south of the Faroe Islands with a sill depth of ∼850 m and the deep part of the Denmark Strait between Greenland and Iceland with a sill depth of ∼620 m. The interior of the Nordic Seas is divided by oceanographic ridges into four deep basins. The eastern part of the Nordic Seas consists of the Norwegian Basin in the south with a depth between 3200 and 3600 m and the Lofoten Basin in the north with a depth of about 3200 m. They are split by the extension of the relatively shallow Vøring Plateau. The western part of the Nordic Seas has the Iceland Plateau in the south (∼2000 m depth) divided by the Jan Mayen Fracture Zone from the Greenland Basin (3400 to 3600 m depth) in the north. The Greenland Basin is confined to the east by the Mohn Ridge that is the extension of the Mid-Atlantic Ridge and to the north by the Greenland Fracture Zone. The Boreas Basin with a depth of ∼3200 m north of the Greenland Fracture Zone forms the natural entrance to the Fram Strait and is usually associated with the Greenland Basin.

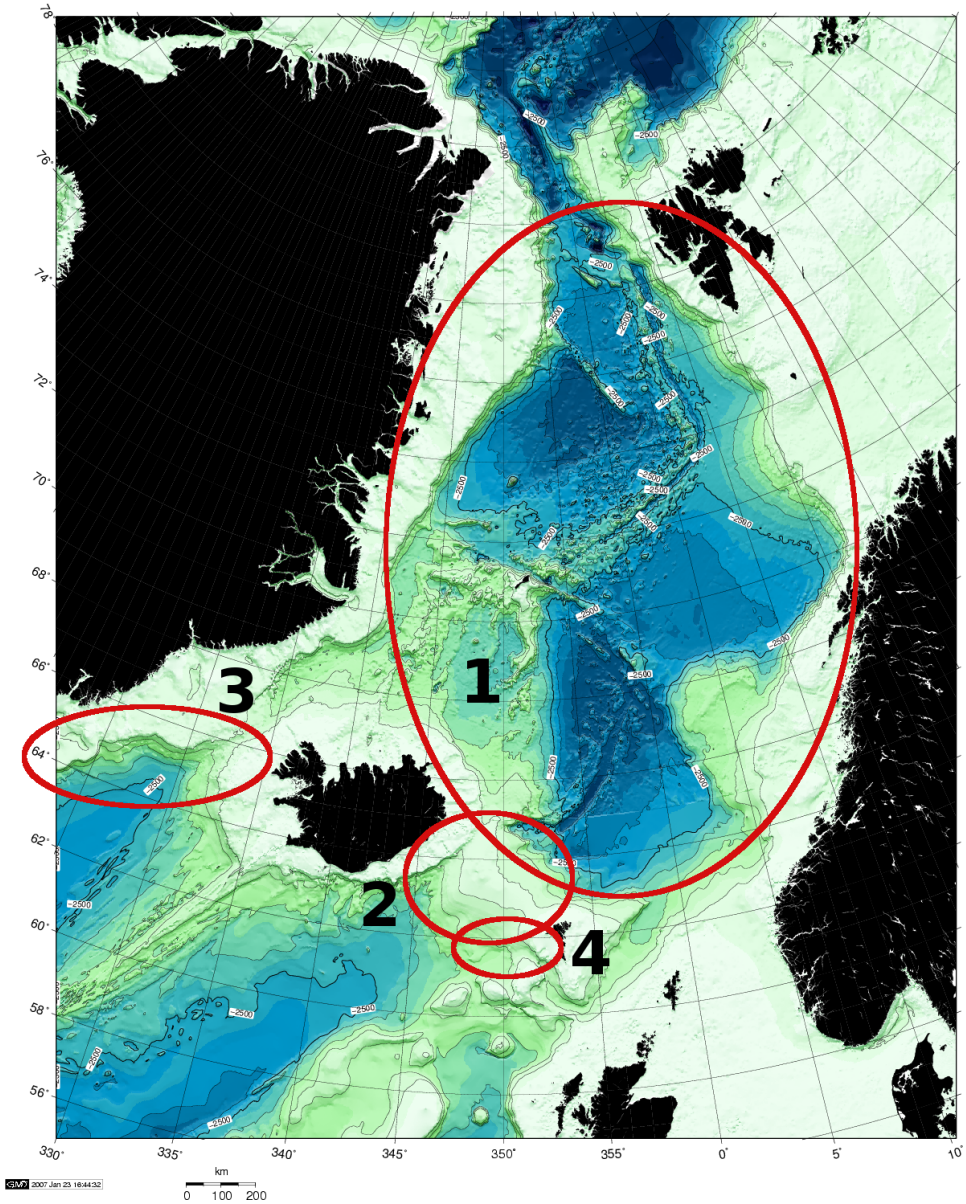

Figure 1.5: *Bathymetry of the Nordic Seas from the General Bathymetric Chart of the Oceans (GEBCO) with a resolution of one minute. The map was produced using the Generic Mapping Tools (GMT) software system (*Wessel and Smith*, 1991). Encircled areas denote the regions of the studies presented in this work. 1: The mid-depth circulation of the Nordic Seas (Paper I,* Voet and Quadfasel*, 2010). 2: Overflow across the Iceland-Faroe Ridge (Unpublished manuscript, section 1.4.2). 3: Entrainment in the Denmark Strait overflow (Paper II,* Voet et al.*, 2010). 4: Entrainment in the Faroe Bank Channel overflow (Paper III,* Fer et al.*, 2010).*

1.3 The circulation internal to the Nordic Seas

A widely studied question regarding the branch of the AMOC into the Nordic Seas is the location of the transformation between inflowing buoyant surface water and the dense water that is exported southward across the Greenland-Scotland Ridge. In the past, deep convection in the Greenland Sea and over the Iceland Plateau were regarded as the most important processes for the water mass transformation (Carmack and Aagaard, 1973; Swift et al., 1980). This thinking changed when Mauritzen (1996) presented an alternative circulation scheme where most of the transformation that is important for the water to be exported southward across the Greenland-Scotland Ridge already takes place in the northward flowing Norwegian Atlantic current in the eastern part of the Nordic Seas. Isachsen et al. (2007) show that production rates for the overflow water are particularly high over the Norwegian and Lofoten Basins.

In a recent study using Argo float data that provide a hitherto unresolved seasonal cycle of the Greenland Basin gyre, Latarius and Quadfasel (2010) emphasise the minor importance of the Greenland Basin for the production of overflow water. Despite the small relevance for the overflow water production, they find an exchange between the Atlantic layer in the edge current and the gyre in the Greenland Basin which they suggest to be driven by meso-scale eddy fluxes.

The regional differences in the production of the overflow water make the circulation internal to the Nordic Seas an important element of the Nordic overturning cell. Its description in the preceding section was only schematic in a two-dimensional frame. In reality, the bathymetry of the Nordic Seas, together with the rotation of the earth and the resulting Coriolis force, lead to a complex circulation that transports the inflowing surface water northward via distinct routes, redistributes the water within the Nordic Seas and determines the paths for the dense water that eventually supplies the dense overflows across the Greenland-Scotland Ridge. Together with the water mass transformation, the circulation sets up and maintains strong fronts. These may become instable and then provide the energy for meso- and submeso-scale eddy fluxes between the gyres and the boundary currents as suggested by Latarius and Quadfasel (2010).

The study presented in this section investigates the circulation at mid-depths in the Nordic Seas using position data from autonomous drifters (Voet et al., 2010). It addresses the mean circulation, its variability on seasonal time scales and forcing mechanisms for the variability.

1.3.1 Previous studies of the Nordic Seas circulation

The oceanographic features of the Nordic Seas were already studied in great detail by Helland-Hansen and Nansen (1909) considering the early stage of development of physical oceanography by that time. Figure 1.6 shows the circulation of the Nordic Seas derived from their hydrographic observations. It already gives a number of details of the circulation of the Nordic Seas still accepted today. The strong boundary currents to the east and to the west, the general cyclonic sense of the circulation and the internal circulation within the basins of the Nordic Seas known today can already be seen in their scheme. They also noted the strong topographic steering of the flow when stating:

> As the configuration of the sea-bottom, even at great depths, has a very great influence upon the directions of currents and the circulation of the sea, even near its surface, it is much to be regretted that a more detailed knowledge of the topography of the bottom of the Norwegian Sea has not been acquired, as such knowledge would have been most desirable in discussing the circulation of this sea. It would be reasonable to suppose that many features of this circulation which may now seem puzzling, would then have been easily explained (Helland-Hansen and Nansen, 1909).

Since then, the development of new instrumentation allowed the study of the Nordic Seas circulation in greater detail. Using satellite tracked surface drifters, Poulain et al. (1996) found the surface circulation of the Nordic Seas to be dominated by the barotropic component and therefore topographically steered. They found the general cyclonic circulation with strong and spatially confined current systems along the continental margins and smaller cyclonic circulation patterns in the basins of the Nordic Seas. The dominant topographic steering was also observed in studies with acoustically tracked subsurface RAFOS floats by Søiland et al. (2008) and Rossby et al. (2009), who showed that this leads to a structured spreading of the inflowing warm Atlantic water masses.

The topographic steering and the fact that many f/H contours (where f is the Coriolis parameter and H is the bottom depth) are closed within the Nordic Seas led Nøst and Isachsen (2003) to develop a simplified diagnostic model of the time-mean, large scale circulation. By assuming that f/H contours are streamlines of bottom geostrophic flow, they derived an analytical expression for the bottom geostrophic velocity on the f/H contours. Driving the model with climatological surface winds and ocean density fields, they calculated the time-mean circulation at the bottom of the Nordic Seas (Figure 1.7). This mean circulation scheme agreed with available current

Figure 1.6: *Circulation of the Nordic Seas from* Helland-Hansen and Nansen *(1909) derived from their observations.*

meter observations. A comparison between the forcing from wind and hydrography for the bottom flow showed that the Ekman pumping driven by the wind was more important for driving the flow than the divergence of the thermal wind shear resulting from the oceanic density field. Using a similar model but allowing for variable wind forcing, Isachsen et al. (2003) showed strong variability of the depth-averaged currents on a seasonal timescale, comparing well with mooring records in the Nordic Seas (Woodgate et al., 1999, see below). As the model of Isachsen et al. (2003) was wind-driven only, this suggests that the variability on monthly to annual timescales seen in the mooring records is driven by the wind rather than by the internal density field.

Following Poulain et al. (1996) with an enhanced surface drifter data set, Jakobsen et al. (2003) could not only construct a detailed mean surface circulation scheme for the northern North Atlantic including the Nordic Seas (Figure 1.8), but also had a reasonably large amount of data available to study the seasonal variation of the surface flow field. They found a modulation of the surface flow field with stronger currents in winter than in summer and interpreted this as being driven by the variability of the large-scale rotation of the wind field.

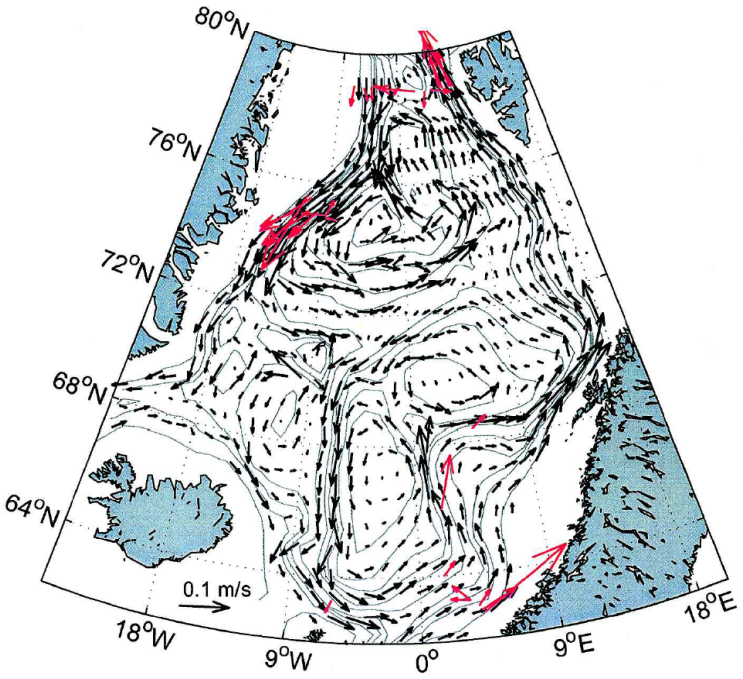

Figure 1.7: *Mean bottom geostrophic velocities (black arrows) in a model from* Nøst and Isachsen *(2003). A scale for the velocity vectors is given to the lower left. Red arrows show observed near-bottom currents from several other studies.*

This wintertime intensification of the flow field was also observed in current time series recorded by moored instruments at the east Greenland continental slope (Woodgate et al., 1999). Their results showed that the volume transport of the East Greenland Current varied from 11 Sv in summer to 37 Sv in winter. As the volume transports in Fram Strait and Denmark Strait, the entrance and exit for the East Greenland Current, respectively, do not show a significant seasonal signal, the seasonal variation observed here was attributed to the internal circulation of the Nordic Seas. Mooring observations in the Norwegian Current off the Norwegian continental slope also showed a wintertime intensification (Orvik et al., 2001). Again, as the inflow into the Nordic Seas across the Greenland-Scotland Ridge did not exhibit this behaviour (Hansen et al., 2008), the seasonal variation must be attributed to variations of the flow speed in the internal gyre.

Mork and Skagseth (2005) used altimeter data to study the annual variability of the sea surface height in the Nordic Seas. Combining these with the steric height estimates derived from hydrographic observations, they calculated seasonal averages of bottom current anomalies in the Nordic

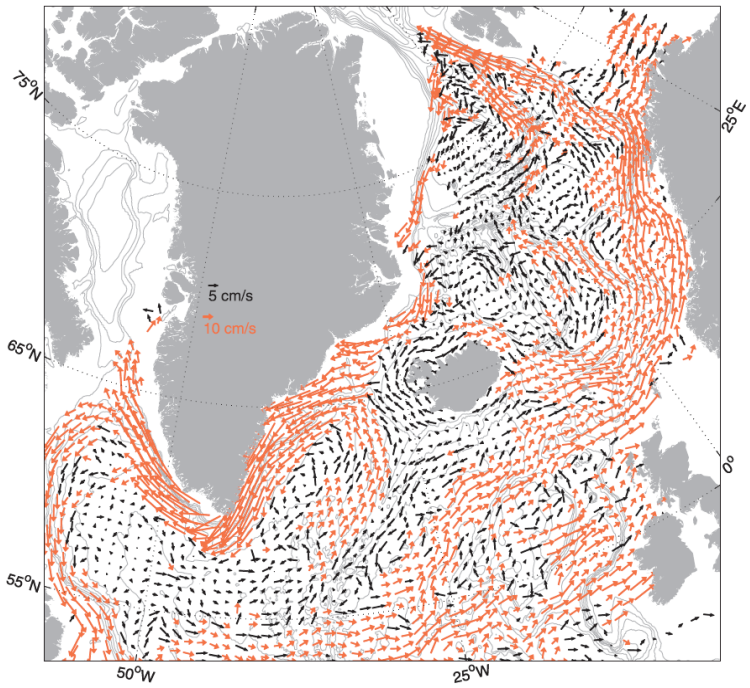

Figure 1.8: *Mean surface circulation of the northern North Atlantic inferred from surface drifter data from* Jakobsen et al. *(2003). Note the different scales for low velocity (black arrows) and high velocity currents (red arrows). The current vectors are derived from 18-day low pass filtered surface trajectories.*

Seas. Their results showed a general cyclonic circulation in the Nordic Seas that was strongest during spring and weakest during autumn. To analyse the forcing of this seasonal variability, the temporal change in the barotropic circulation integrated around a closed f/H contour was compared with the wind stress curl integrated over the area bounded by the f/H contour. The comparison showed that the phase of a harmonic fit to the temporal change of the circulation matches with the phase of an harmonic fit to the wind stress curl. This indicates that the variability of the circulation is driven by the variability of the wind stress curl. However, amplitudes between the two fits differ.

Summing up, the studies presented above give a picture of the Nordic Seas circulation that is characterised by strong topographic control of the flow field and a general cyclonic circulation. In contrast to the exchange across the Greenland-Scotland Ridge, the variability of the internal circulation is strong on a seasonal time scale. Both, model results and the analyses of observational data, suggest that the variability is primarily wind driven.

1.3.2 A study on the mid-depth circulation of the Nordic Seas

The study presented in section 2.1 (Voet et al., 2010) aims at investigating the mid-depth circulation of the Nordic Seas, its seasonal variability and the forcing mechanisms leading to this variability. In contrast to the studies presented above, it is the first investigation of the basin wide circulation of the Nordic Seas using direct observations at depth over a large spatial scale. These direct observations are the position data from Argo floats that provide an estimate of the currents at depth.

Trajectories of individual Argo floats in the Nordic Seas are strongly aligned with the local bottom topography (Gascard and Mork, 2008). The study shows that only few floats moved from one basin to another, indicating that the internal recirculation within the basins is by far dominating the larger-scale exchanges.

The mean circulation presented in Voet et al. (2010, their Figure 7) shows that the mid-depth circulation is generally cyclonic with strong internal gyres in the four major basins of the Nordic Seas. This confirms the model results from Nøst and Isachsen (2003) and matches with the current meter records shown in Figure 1.7. The flow is weak in the interior of the gyres with less than 1 cm/s and somewhat stronger at the rims of basins with up to 5 cm/s. The pattern of the circulation at depth compares with that at the surface in Figure 1.8, but the mean velocities at depth are about five times smaller than those at the surface.

The seasonal variability of the flow field is calculated by Jakobsen et al. (2003) as the difference between well resolved flow patterns for summer and winter. In contrast, monthly mean gyre velocities are defined in this study that do not resolve a spatial pattern but show the seasonal cycle in the strength of each basin gyre. The resulting seasonal variability is compared with the seasonal cycle of the wind forcing. Contrary to Mork and Skagseth (2005), this comparison is not reduced to one location in one single gyre but takes into account observations at many different locations around the rim of each of the four gyres. The comparison between gyre velocity and wind forcing is not reduced to the phase of their seasonal cycle but also takes its amplitude into account.

The results show seasonal cycles in the gyre strengths with minima in summer in the Greenland Basin, the Norwegian Basin and over the Iceland Plateau. For the Lofoten Basin no such seasonal cycle could be observed. The seasonal variation of the gyre speeds ranges from less than 1 cm/s over the Iceland Plateau to more than 4 cm/s in the Greenland Basin. The wind is the dominant driving force for the seasonal variability in the Greenland and Norwegian Basin while for the Lofoten Basin and Iceland Plateau less

than 50% of the variability on seasonal time scales can be explained by the wind.

1.4 The dense overflows across the Greenland-Scotland Ridge with a focus on the Iceland-Faroe Ridge overflow

The deep passages in the Greenland-Scotland Ridge may be seen as a bottleneck for the very northern part of the Meridional Overturning Circulation in the North Atlantic as it forces the dense water into very restricted pathways. This makes the deep passages excellent points for measuring the Nordic branch of the overturning circulation. An exception is the overflow across the Iceland-Faroe Ridge. It is the least known for its overflow transports as it is very wide and the overflow seems to be more sporadic than at the other locations (Østerhus et al., 2008).

In the following, an overview of the two main overflows across the Greenland-Scotland Ridge will be followed by a review of previous studies on the Iceland-Faroe Ridge overflow. Then a study on the Iceland-Faroe Ridge overflow is presented. Using recent year long current observations from the western part of the Iceland-Faroe Ridge together with shipboard hydrographic measurements, the results of my analyses provide a new estimate for the mean overflow transport rate across the Iceland-Faroe Ridge.

1.4.1 The dense overflows at the ridge crest

The dense water accumulated at depth in the Nordic Seas passes over the Greenland-Scotland Ridge and feeds the deep southward flowing branch of the overturning circulation in the North Atlantic. The Greenland-Scotland Ridge, stretching from Greenland over Iceland and the Faroe Islands to Scotland, has an average depth of only about 500 m. Two deeper passages, the Faroe Bank Channel and the Denmark Strait, cut through it east and west of Iceland with sill depths of 620 m and 840 m. About 80 % of the total southward dense water transport from the Nordic Seas crosses the ridge via these two deep passages while the remaining 20 % of the dense water export occurs across the Iceland-Faroe Ridge and over the Wyville-Thomson Ridge (Quadfasel and Käse, 2007).

The overflow through the Faroe Bank Channel has been studied extensively, resulting in a consistent picture of its conditions at the sill. The temperature distribution of the water column is dominated by the deep overflow waters with temperatures below 0°C and the overlying Atlantic waters, warmer than 7°C, with a relatively sharp interface between them. The cold bottom layer is on average 250 m thick. Mean velocities at the sill exceed 1 m/s in a layer that is approximately 100 m thick with the velocity core 100 m off the bottom (Hansen and Østerhus, 2007). The volume transport of cold overflow water at the sill has been monitored continuously

with moored acoustic doppler current profilers (ADCP) from 1995 until now (Figure 1.9). The kinematic overflow flux, i.e. the volume transport determined from the ADCP velocity profiles only, was 2.1 Sv when averaged over a whole decade of measurements. When the overflow water is defined as water with a potential density anomaly higher than 27.8 kg/m^3, the density criterion that is commonly referred to as overflow water (e. g. Dickson and Brown, 1994), the mean volume flux is 1.9 Sv, while the mean transport of water colder than 3℃ is 1.7 Sv (Hansen and Østerhus, 2007). The overflow volume transport does not exhibit any significant trend over a period of ten years, whereas on shorter time scales a considerable amount of variability was found. Fluctuations of velocity and hydrographic parameters are coherent across the channel, not a surprising result as the channel width of 15 km at the sill is close to the baroclinic Rossby radius. Daily transport values vary between 0.7 and 4.5 Sv, monthly averages range from 1.5 to 2.9 Sv. In some years, the overflow flux has a clear seasonal cycle with a maximum in late summer when also the lowest bottom temperatures are observed. On average, the seasonal cycle explains 28 % of the overall transport variance and has an amplitude of 0.22 Sv (Hansen and Østerhus, 2007). For further details about the overflow at the sill of the Faroe Bank Channel the reader is also referred to review articles by Hansen and Østerhus (2000), Saunders (2001), Borenäs and Lundberg (2004) and Østerhus et al. (2008).

The Denmark Strait between Iceland and Greenland is dominated by three major currents. Very cold water with low salinity is transported southward over the Greenland shelf. On the eastern side of the Denmark Strait over the Icelandic shelf, the Irminger Current flows northward as a warm and saline current deriving from the North Atlantic Current. The deeper part of the Denmark Strait is dominated by the outflow from the Nordic Seas with water temperatures below 0°C and a salinity around 34.9. The greater width of the Denmark Strait, compared to the Faroe Bank Channel, leads to a horizontal separation of the inflowing warm surface current and the cold overflow at depth. In addition, the width of the strait that is greater than the baroclinic Rossby radius allows the jet to develop eddies at the sill of the Denmark Strait. Velocities of the overflow jet at the sill are on average 0.5 m/s and may exceed 1 m/s (Macrander et al., 2007). The vertical velocity structure is similar to the Faroe Bank Channel overflow jet, but with an overall barotropic southward component. The overflow transport in the layer below the maximum current shear is around 3 Sv with a variability of about 0.7 Sv on up to interannual timescales (Macrander et al., 2005). However, on longer time scales the transport estimates from moored ADCPs suggest a stable Denmark Strait overflow (Figure 1.9). Further details about the Denmark Strait overflow can be found in review articles by Saunders (2001), Quadfasel and Käse (2007) and Dickson et al. (2008).

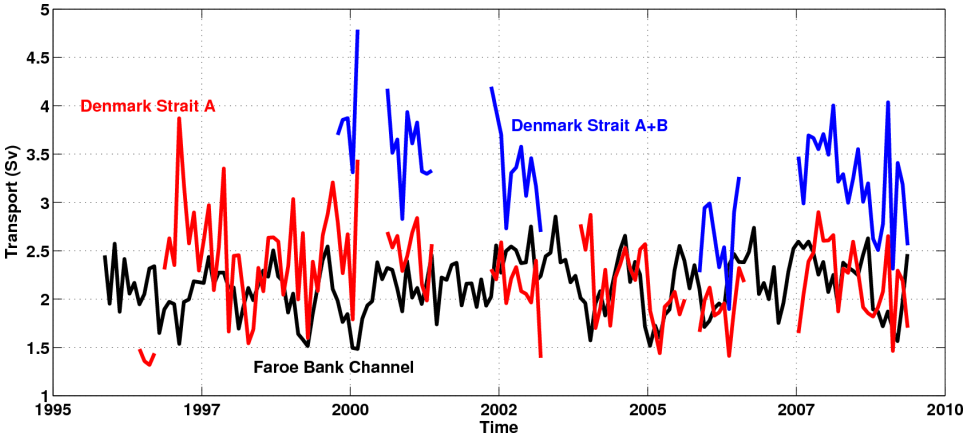

Figure 1.9: *Time series of the dense overflow volume transport in the Faroe Bank Channel (black) and Denmark Strait (red and blue). For both overflows, the volume transport time series were constructed from moored acoustic doppler current profiler (ADCP) measurements. In the Faroe Bank Channel, one ADCP is sufficient to estimate the overflow transport with adequate accuracy (*Hansen and Østerhus*, 2007). For the Denmark Strait, two different volume transport time series have been constructed for periods with two moored ADCP'S available (blue curve) and for the whole period where at least one mooring was deployed (red curve). In the latter case, measurements from only one mooring are used even when more mooring data is available. For positions of the the moorings at the sill of Denmark Strait and the method of estimating the overflow transport see* Macrander et al. *(2005).*

The two main overflows are thus relatively well studied with the Faroe Bank Channel overflow transports, owing to its narrow sill width, being observed with a higher accuracy than the Denmark Strait overflow. Hydraulic control theory has shown to be useful for the study of both overflows (Whitehead, 1998; Käse and Oschlies, 2000; Käse et al., 2003; Girton et al., 2006). The parameterisation of hydraulic control for dense overflows also led to an improved representation of the Meridional Overturning Circulation in models of the ocean circulation (Kösters et al., 2005; Käse, 2006; Köller et al., 2010).

The stability of the total overflow across the Greenland-Scotland Ridge is crucial for the stability of the whole AMOC, as a reduction of the southward dense water export will be accompanied by a reduced inflow of warm Atlantic water into the Nordic Seas. An understanding of overflow processes and overflow variability is important for the detection of trends in the overflows from the Nordic Seas into the North Atlantic that would indicate a weakening Nordic branch of the AMOC as predicted by climate projections.

An example for the importance of understanding natural variability is the study of Bryden et al. (2005) and the following discussion as explained in Section 1.2.

The results of an ensemble hindcast experiment with a general ocean circulation model by Olsen et al. (2008), showing convincing agreement with the overflow volume transports estimated from measurements shown in Figure 1.9, indicate no significant trend for the dense Nordic overflows for the period 1948-2005. This implies a stable branch of the AMOC into the Nordic Seas on decadal time scales for more than 60 years. The Olsen et al. (2008) study however depends on the stability of the overflows across the Iceland-Faroe Ridge and the Wyville-Thomson Ridge. These shallow and wide gaps in the Greenland-Scotland Ridge are not explicitly resolved in the coarse resolution of the model and are thus treated as a constant overflow with a strength of 1.3 Sv. What if the small overflows are not as stable as assumed? How can their mean transport and, maybe more important, the associated variability be estimated? These are important questions regarding both, the results of Olsen et al. (2008) and the general detectability of a changing strength of the Nordic AMOC branch.

The overflow volume transport across the Wyville-Thomson Ridge was estimated in a recent study by Sherwin et al. (2008). Results from ADCP deployments over several years show that the mean overflow volume transport of undiluted water from the Nordic Seas is up to 0.3 Sv with larger flows in summer than in winter. For the confirmation of a persistent seasonal cycle a longer mooring record is needed, though. This holds also for variability on longer time scales from interannual to decadal.

The large width of the Iceland-Faroe Ridge makes it the most demanding overflow to measure. The commonly cited mean overflow transport of 1 Sv is based on a few hydrographic sections recorded over the ridge (Hermann, 1967). Only little is known about the variability of the Iceland-Faroe Ridge overflow on any time scale. It is the least known part of the overflow across the Greenland-Scotland Ridge even though it accounts for almost 20% of it.

1.4.2 An estimate for the dense water transport across the Iceland-Faroe Ridge from observations applying hydraulic control theory

This section is based on my own analysis of moored current and synoptic hydrographic observations. The results have been presented at several conferences, but so far only a draft of a manuscript does exist.

Introduction

The Iceland-Faroe Ridge stretches from Iceland to the Faroe Islands. It has a mean depth of about 400 m and slopes from west to east. Several deeper gaps cut through the sill crest. A passage close to the Icelandic continental slope with a sill depth of about 450 m is called *western valley* throughout this study. Several gaps are located further to the east with a maximum depth of about 500 m close to the Faroe Islands.

The existence of an overflow across the Iceland-Faroe Ridge has been known for more than a century (Knudsen, 1898). The first transport calculations for the Iceland-Faroe Ridge overflow were carried out by Dietrich (1956). His estimate for the overflow volume transport from hydrographic data amounts to 5.8 Sv. However, he did not consider the geostrophic effect of turning the flow from across-slope to along-slope. This leads to an overflow transport estimate that is probably almost an order of magnitude too large.

The only reasonable documented estimate for the total overflow volume transport across the Iceland-Faroe Ridge is provided by Hermann (1967) with data from the Overflow '60 expedition. In his study, a method for the calculation of the fraction of different water masses is developed. By integrating the fraction of the overflow water over depth, an equivalent thickness of the overflow layer is calculated. Hydrographic cross sections over the ridge were run three times with only a few days in between. By tracing anomalies from the mean equivalent overflow thickness, the speed of the overflow plumes were estimated. For most cases this compared well with direct current measurements recorded in the vicinity of the cross sections. By combining the velocities and equivalent thicknesses, an overflow volume transport estimate of 1.1 Sv was obtained for the Iceland-Faroe Ridge.

The commonly cited literature source for an overflow transport of 1 Sv across the Iceland-Faroe Ridge is the review paper by Meincke (1983). He shows a scheme with an overflow of 0.5 Sv through the western valley close to Iceland and another 0.5 Sv that is distributed over the eastern part of the ridge. It is not clear from the paper where these transport estimates originate from, but probably the value is just the 1.1 Sv from Hermann (1967) rounded down to 1.0 Sv.

Several studies were dedicated to the intermittent character of the overflow through notches in the eastern part of the ridge. Müller et al. (1974) observed an overflow event through a gap of the Iceland-Faroe Ridge using temperature, salinity, light attenuation and current measurements. The flow field indicated that a perturbation leads to a spill-over of cold water through the channel. After such an event, the cold water on both sides is driven away from the sill by gravity. Hansen and Meincke (1979) used hydrographic

data to demonstrate the existence of eddies and meanders over the Iceland-Faroe Ridge. The eddies can contribute to the transport of dense water across the ridge. As soon as they move cold and dense water over the crest, gravity will act on the water and it will descent southwards. Observations with bottom mounted ADCPs at the eastern part of the ridge also showed frequent occurrence of overflow water with a transition from stronger to weaker overflow in winter, but no transport estimate for the eastern part of the ridge is given (Østerhus et al., 2008). At the western part of the Iceland-Faroe Ridge, Perkins et al. (1994) observed an overflow event that had a pulsating character.

Despite this intermittency of overflow at single locations over the eastern part of the ridge, the accumulated overflow current measured with moored current meters close to the Icelandic slope indicated that the total overflow is remarkably stable (Perkins et al., 1998). The accumulated transport in their study is calculated from two hydrographic sections at the Icelandic slope and amounts to 0.7 Sv of pure overflow water. As not all of the flow was covered, this is underestimating the total Iceland-Faroe Ridge overflow transport. Surprisingly, Perkins et al. (1998) do not find evidence for significant flow of cold water from the Nordic Seas through the western valley.

Data from a moored ADCP at the Icelandic slope south of the ridge crest from 2005-2007 gives the opportunity to revisit the question of overflow through the western valley. Is there a steady overflow in the western valley and if yes, does it show any sign of seasonal variability, i. e. would it contradict the assumption of a steady Iceland-Faroe Ridge overflow as assumed by Olsen et al. (2008)?

In this study, historical hydrographic data is used together with the recently recorded ADCP data to obtain an estimate for the overflow of dense water through the western valley of the Iceland-Faroe Ridge. It is shown that hydrographic conditions upstream of the western valley can explain the observed overflow using hydraulic control theory. This method is then applied to the overflow across the whole Iceland-Faroe Ridge.

Data

A mooring equipped with an upward looking ADCP and a microcat measuring temperature, conductivity and pressure near the bottom was deployed at the Icelandic slope south of the Iceland-Faroe Ridge in September 2005 and recovered in October 2007. Figure 1.10 gives the position of the mooring. The bottom depth at the mooring site was about 610 m. The ADCP provided a time series of current speed within bins of 10 m with a length of more than two years. The microcat stopped recording in May 2007 but still

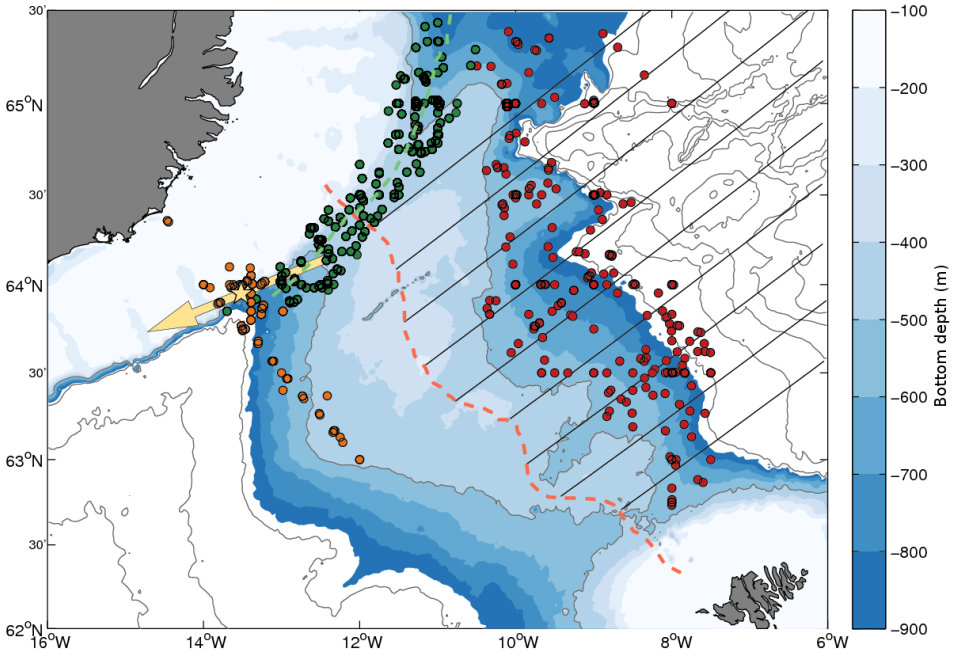

Figure 1.10: *The bathymetry of the Iceland-Faroe Ridge and positions of data used in this study. Grey lines show depth contours every 500 m, the blue colour scale gives detailed depth levels between 100 and 900 m bottom depth. The yellow star marks the mooring site at the Icelandic slope, the yellow arrow gives the mean flow direction near the bottom where the flow of dense water has its maximum velocity. Orange dots show positions of temperature profiles that are used to construct a temperature section across the mooring site. Green dots show positions of temperature profiles used to calculate a temperature section along the western valley, i. e. the deep part of the ridge close to the Icelandic slope. The dashed green line shows the path along which the profiles were selected. The red dashed line approximately gives the crest of the Iceland-Faroe Ridge. Diagonal black lines mark upstream bins where the upstream temperature profiles (red dots) are sorted into for the calculation of an upstream temperature section. All temperature profiles are taken from the NISE data collection (see text for details).*

provided time series of near-bottom temperature and salinity with a length of almost two years.

In addition to the mooring data, hydrographic data extracted from the NISE data collection is used. NISE (Norwegian Iceland Seas Experiment) is a joint project of research institutions from Iceland, the Faroe Islands and Norway combining hydrographic measurements of the northern North Atlantic and the Nordic Seas from more than one hundred years (Nilsen et al., 2008). In the following, only temperature data from the NISE data set will be used as there is a very tight temperature-density relation in the water masses. The positions of temperature profiles from the NISE data set used for the calculation of climatological temperature sections in this study are shown in Figure 1.10. The spatial distribution of all available temperature profiles over the Iceland-Faroe Ridge can be seen in Figure 1.11 which shows mean near-bottom temperatures and their standard deviations over the Iceland-Faroe Ridge. Mean temperatures are calculated on a grid with a cell size of 11×11 km. Temperature profiles are available at every bin giving a mean temperature. The near-bottom mean temperatures clearly show the reservoir of cold water in the Nordic Seas northeast of the ridge. Warm water is located over shallow bottom depths around the Faroe Islands and south of Iceland. The cold water flowing through the Faroe Bank Channel is clearly visible as well as its warming downstream of the sill due to entrainment (compare Section 1.5.2). Both warm and cold water masses are present along the Iceland-Faroe Ridge. The high standard deviation in bottom temperature over the ridge shows the strong local variability in the overflow across the Iceland-Faroe Ridge as described in the earlier studies.

Overflow through the western valley

The velocity profile calculated by averaging over velocity time series recorded at the Icelandic slope mooring site at different depth levels is shown in Figure 1.12. The velocities were rotated to the mean direction of the near-bottom flow (see Figure 1.10). The maximum average velocity is 0.53 m/s at a height of 50 m above the bottom. The mean velocity profile along the mean direction is typical for a dense plume with reduced velocity close to the bottom in the Ekman layer due to bottom friction, a velocity maximum above the Ekman layer and decreasing velocity with height. The profile compares very well with the mean velocity profile of the Faroe Bank Channel overflow plume (Hansen and Østerhus, 2007), with the magnitude of the velocities being half of that in the Faroe Bank Channel. The flow reverses its direction at a depth of about 350 m, showing the inflow of water originating from the North Atlantic into the Nordic Seas at the surface as shown by Perkins et al. (1998).

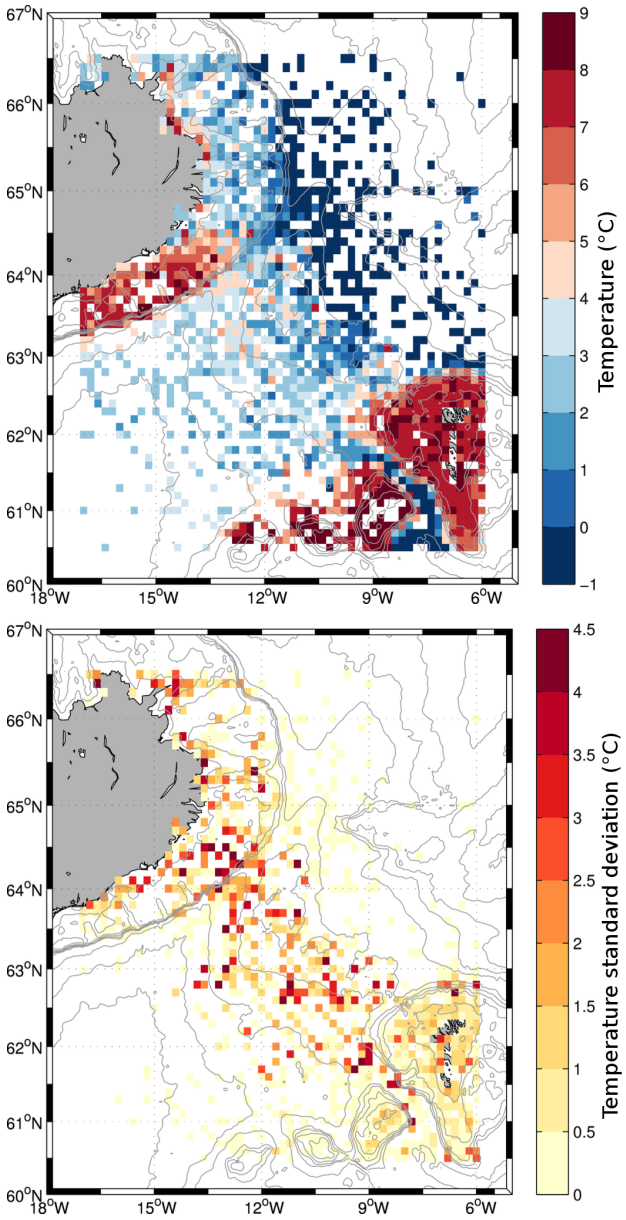

Figure 1.11: *Top: Mean near-bottom temperature calculated from the NISE data on a grid with a rectangular bin size of 11 km. Only temperature profiles with a measurement not farther away than 50 m off the bottom were used for the calculation. The colour scale gives the near-bottom temperatures in °C. Bottom: Standard deviation of the near-bottom temperature on the same grid and with the same data as in the top figure. The colour scale gives the standard deviation in °C. The bottom depth is taken from the ETOPO2 bathymetry and contours give the [-3000 -2000 -1500 -1000 -400 -300 -200 -100] m depth levels.*

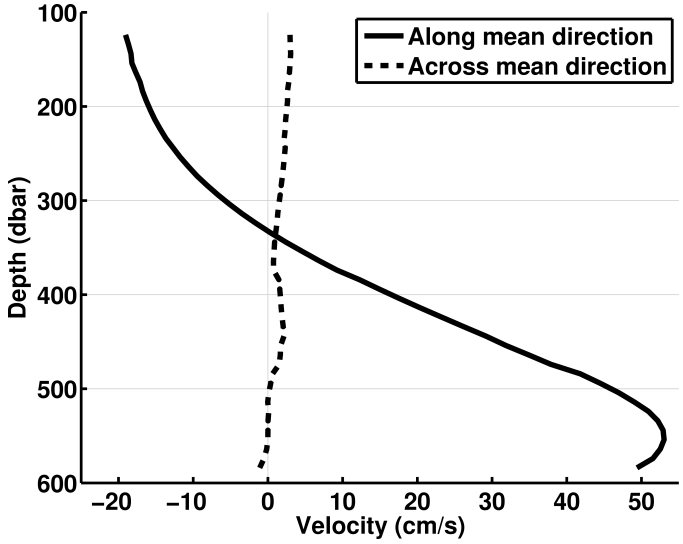

Figure 1.12: *Mean velocity profile calculated from the two year long ADCP record at the mooring site shown in Figure 1.10. Velocities were rotated to the mean direction at the velocity maximum at about 550 m depth. The full line shows the mean current velocity in the mean direction, the dashed line gives the mean velocity perpendicular to the mean direction.*

The time-mean near-bottom temperature at the mooring as recorded by the microcat is 3.9°C. This temperature is about half way between that of the Nordic source water (0°C) and the overlying Atlantic water (8°C). Thus, assuming that the dense plume partly consists of water that overflowed the Iceland-Faroe Ridge from the Nordic Seas, entrainment of Atlantic water into the overflow plume has occurred on the way to the mooring site. The result is a one to one mixture of overflow water and entrained Atlantic water.

Both near-bottom velocity and temperature have a clear seasonal cycle. Figure 1.13 shows a harmonic fit to low passed time series of velocity and temperature. The seasonal maximum of the velocity time series is in early summer, the minimum of the temperature time series occurs in spring. The seasonal variation is 0.09 m/s (0.48 to 0.57 m/s) for the velocity and 1.2 K (3.4 to 4.6°C) for the temperature time series. Thus, the seasonal period of high current velocity coincides approximately with the seasonal period of low plume temperatures.

We calculate the mean volume transport $\overline{T}$ of the dense current as

$$\overline{T} = \overline{v} \cdot \overline{w} \cdot \overline{h} \cdot \overline{f} \tag{1.1}$$

with the plume velocity $\overline{v}$, the plume width $\overline{w}$, the plume height $\overline{h}$ and the fraction of pure overflow water $\overline{f}$. Overlines denote the time-mean of the variables.

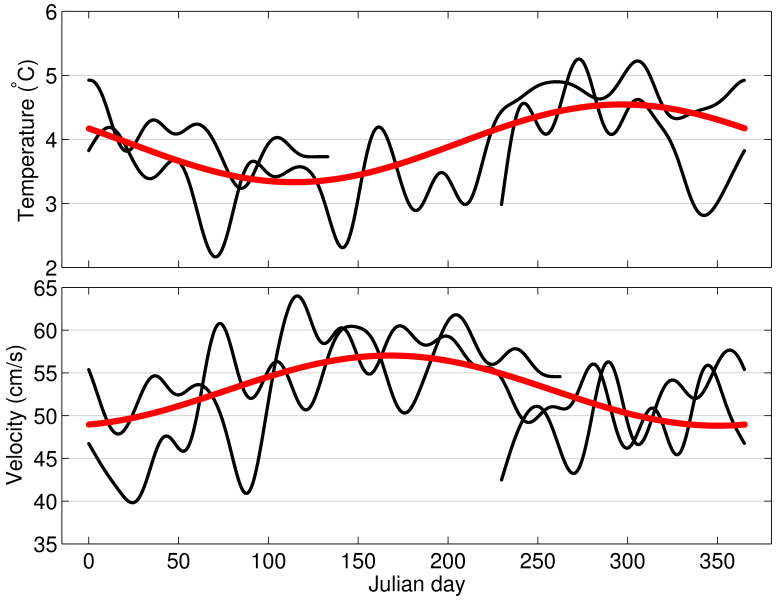

Figure 1.13: *Top: Thirty day low-passed time series from the mooring at the Icelandic slope of near-bottom temperature (black line) and a harmonical seasonal fit (red line). The temperature time series was split at the end of the year, leading to two measurements for almost each day of the year. Bottom: Thirty day low-passed time series of near-bottom velocity in the mean flow direction (black line) and harmonical seasonal fit (red line). The time series was split as in the upper figure.*

The mean velocity $\overline{v}$ can be calculated from the mean velocity profile shown in Figure 1.12 by taking the mean velocity between bottom and upper interface.

To get an estimate for the upper interface height $\overline{h}$ we have the possibilities to using the mean velocity profile again or the hydrographic data as an alternative. (1) Following Hansen and Østerhus (2007), the interface height is defined as the height where the mean velocity profile has decreased to half the maximum mean velocity. (2) The NISE data can be used to construct a climatological temperature section perpendicular to the mean flow direction of the current. Figure 1.10 gives the location of the profiles used to calculate this temperature section shown in Figure 1.14. The interface height of the plume at the slope is taken as the height of an isotherm from the temperature section. The selected isotherm determines the fraction of original overflow water, i. e. chosing the 4°C isotherm results in an $\overline{f}$ larger than that for the 6°C isotherm.

The mean width $\overline{w}$ of the dense plume is the factor for the volume transport calculation that is the most difficult to determine. The velocity was

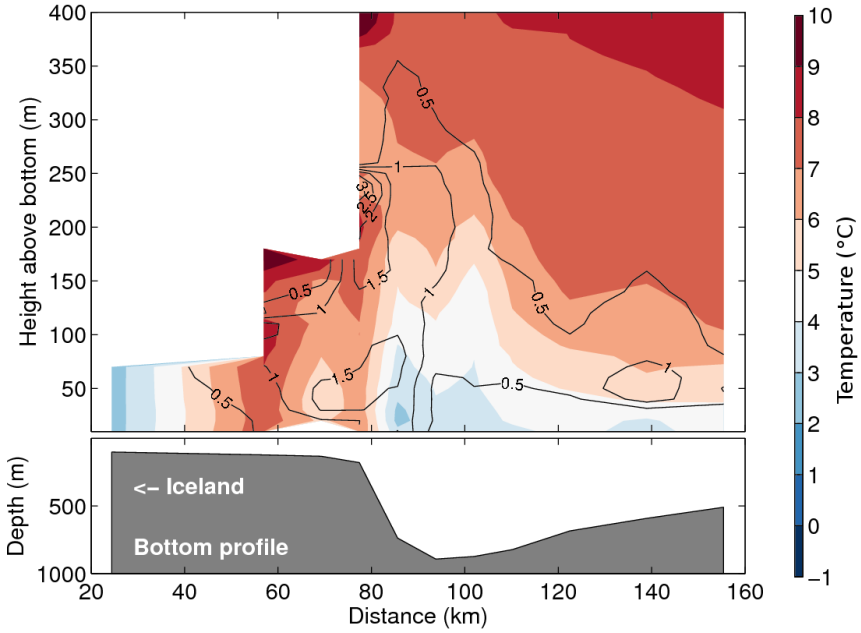

Figure 1.14: *Top: Climatological temperature section across the Icelandic slope. Positions of individual temperature profiles used to calculate the section are shown in Figure 1.10. The profiles were averaged into bins with a size of 6 km over the slope (between kilometer 70 and 110 on the x-axis) and 12 km elsewhere. The position of the moored ADCP is approximately at kilometer 85 on the x-axis. The colour scale gives the mean temperature in °C, black lines show the standard deviation of the mean temperature in °C. Note that the y-axis gives the height above bottom. Bottom: Bottom depth along the temperature section. The left side of the section is directed towards the Icelandic slope.*

only measured at one location at the slope and thus contains no information about the plume width. The temperature section in Figure 1.14 may be used to read the plume width, but the bin size chosen to calculate the section at the slope is only about 6 km. The Rossby radius of deformation Ro, giving the length scale at which rotational effects become important, serves as a lower boundary for the plume width if the overflow current is in geostrophic balance. The Rossby radius of deformation is calculated as

$$Ro = \frac{\sqrt{g'H}}{f} \tag{1.2}$$

where $g' = g\frac{\delta\rho}{\rho}$ is the reduced density, H is the depth of the water layer and f is the Coriolis parameter. Using a height of 200 m and densities of 1027.3 kg/m^3 in the Atlantic water and 1028.0 kg/m^3 in the overflow water, the Rossby radius of deformation is about 9 km.

	$\overline{v}$	$\overline{h}$	$\overline{w}$	f	$\overline{T}$
Average	0.45 m/s	200 m	10 km	0.5	0.45 Sv
Minimum	0.5 m/s	150 m	5 km	0.6	0.23 Sv
Maximum	0.4 m/s	250 m	20 km	0.4	0.80 Sv

Table 1.1: *Factors used for the calculation of the volume transport of dense water at the mooring site.*

Estimates for the factors used in Equation 1.1 and the resulting volume transports are given in Table 1.1. The factors for the average case were obtained as follows. The interface height as calculated from the velocity profile is about 200 m. This results in a mean velocity of 0.45 m/s. The average temperature of the lower 200 m of the water column in the temperature section in Figure 1.14 is 4°C. This implies a mixture of 50% overflow water of 0°C and 50% entrained Atlantic water of 8°C as pointed out above. Thus, the factor for the fraction of pure overflow water $\overline{f}$ is 0.5. The width was estimated from the hydrographic section to 10 km which is in agreement with the Rossby radius scaling.

The minimum and maximum values in Table 1.1 are lower and upper estimates for the height and the width of the plume. Reducing the height in the minimum case increases the mean velocity because less of the upper part of the plume with lower velocities is included in the calculation of $\overline{v}$. The lower plume height also increases the mixing factor $\overline{f}$ as there is colder water in the lower part of the water column. In the maximum case, an increased height of 250 m and a broader plume with 20 km width is used.

The resulting volume transport of pure overflow water, i. e. water of 0°C, is about 0.5±0.3 Sv. The seasonal variability of velocity and temperature shown in Figure 1.13 translate into a seasonal variability of the cold water transport of about ±0.1 Sv.

The mooring is situated not far away from the mooring of Perkins et al. (1998). They argue that the overflow water observed at this site must have crossed the ridge over its eastern part as they do not find any sign for significant overflow through the western valley. However, the high current speeds we observe indicate local acceleration of the plume, i. e. the dense water seems to have descended from the western valley.

Another indicator for the western valley being a source of the dense water at the mooring site is the occurrence of a cold core at the continental slope in the temperature section in Figure 1.14 that has no counterpart further to the east. If the dense water was coming from the eastern part of the Iceland-Faroe Ridge as assumed by Perkins et al. (1998), it were to follow the isobaths closely to maintain its depth level. Thus, it would have to travel through the southern exit of the western valley, thereby passing through

the eastern part of the temperature section in Figure 1.14. Entrainment of warmer water during the turn around the western valley exit should even lead to a temperature increase when the water arrives at the slope. As this is not the case, it is likely that at least part of the overflow water observed at the mooring site derives from the western valley.

A further sign for a connection between the dense water transport at the mooring and overflow through the western valley is the variability of the temperature time series on time scales from 2 to 7 days. Cold events seem to pass by the mooring. These might be connected with the overflow event at the sill of the western valley with a time scale of four days observed by Perkins et al. (1994).

To test the assumption of overflow water deriving from the western valley, the height of the dense water reservoir upstream of the western valley is calculated from the hydrographic data. The reservoir height can then be used to determine the maximum possible overflow through the western valley using hydraulic control theory.

The maximum exchange flow Q through a strait, if the flow is hydraulically controlled, is given as

$$Q = \frac{g' h_u^2}{2f} \tag{1.3}$$

with the reduced density g' defined as in Equation 1.2, the upstream height of the dense water h_u and the Coriolis parameter f (Whitehead et al., 1974). This gives the maximum volume flux through a rectangular opening. An adjustment to a parabolic sill shape leads to an improved estimate (Borenäs and Lundberg, 1988), but for the sake of simplicity we use the formula for a rectangular shaped opening.

The mean temperature structure along the western valley as calculated from the historical hydrographic data is shown in Figure 1.15. It shows the typical structure of the dense water reservoir in the Nordic Seas, sloping isotherms over the Iceland-Faroe Ridge and the vanishing of the cold water layers as mixing takes place during the descent of water at the southern side of the ridge.

If hydraulic control were to apply to the overflow through the western valley, the maximum possible volume transport could be calculated using Equation 1.3 by getting the upstream reservoir height from Figure 1.15 and using the density difference between the reservoir source water and the downstream ambient water. Upstream height and density difference are not independent from each other. Choosing the 0°C isotherm instead of the 1°C isotherm results in a stronger density difference. Applying Equation 1.3 results in a maximum possible overflow transport between 0.4 Sv for an upstream height of 150 m and a density contrast $\delta\rho/\rho$ of $5{\times}10^{-4}$ and

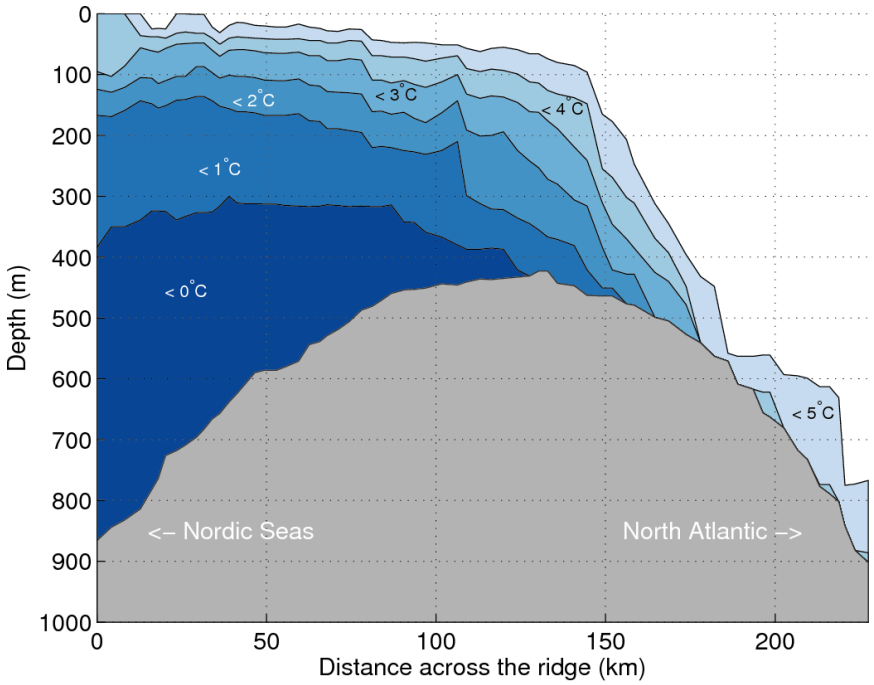

Figure 1.15: *Mean temperature structure along the western valley calculated from historical hydrographic data. The positions of temperature profiles and the path along the valley used to extract the bottom depths are shown in Figure 1.10.*

0.95 Sv for an upstream height of 250 m and a density contrast of 4×10^{-4}. Thus, the hydraulic control estimate for the transport is about 0.7 ± 0.3 Sv. This is of the same magnitude as the transport estimated from the velocity measurements downstream of the western valley, but somewhat larger.

The temperature profiles of the upstream region are divided into two seasons to investigate a possible seasonal cycle of the upstream reservoir height. The seasons for this division are chosen to match with the seasonal cycle of the current velocity observed downstream (Figure 1.13). Hence, they are sorted into the periods April-September and October-March. The result is a depth of the 0°C isotherm that varies by about 50 m between summer and winter with a greater depth in winter. The seasonal cycle in reservoir height and the resulting seasonal cycle of the overflow transport thus agree with the seasonal cycle seen in the mooring records. It indicates the connection between the flow observed at the mooring and an hydraulically controlled overflow through the western valley.

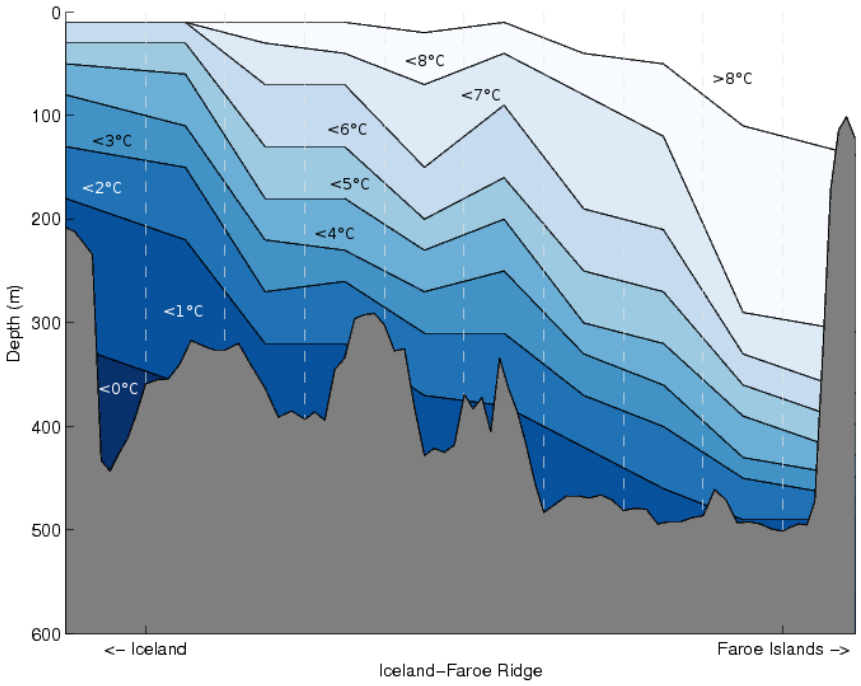

Figure 1.16: *Mean temperature structure upstream of the Iceland-Faroe Ridge crest. See Figure 1.10 for positions of the profiles used to calculate the mean temperatures. The bottom depth shown in grey gives the bottom depth at the sill crest associated with the upstream bins as shown in Figure 1.10. Dashed white lines divide the different bins.*

A hydraulic estimate for the overflow across the eastern part of the Iceland-Faroe Ridge

As the use of hydraulic control theory for an estimate of the dense water transport through the western valley has proven to produce realistic results, we now apply this method to the eastern gaps that cut through several parts of the Iceland-Faroe Ridge. Temperature profiles upstream of the ridge crest between the 530 m and 1300 m isobaths are sorted into bins (Figure 1.10) to calculate the mean upstream temperature structure (Figure 1.16). The isotherms slope from the Icelandic side of the ridge to the Faroe side. The difference in the depth of the isotherms between the two ends of the ridge is about 300 m. This matches with the overall slope of isotherms along the Greenland-Scotland Ridge with a high cold water reservoir level on the Greenland side and a relatively low reservoir level on the Scotland side (Wilkenskjeld and Quadfasel, 2005).

Figure 1.17 shows the transport range resulting from two different density contrasts and the upstream reservoir height as given in Figure 1.16

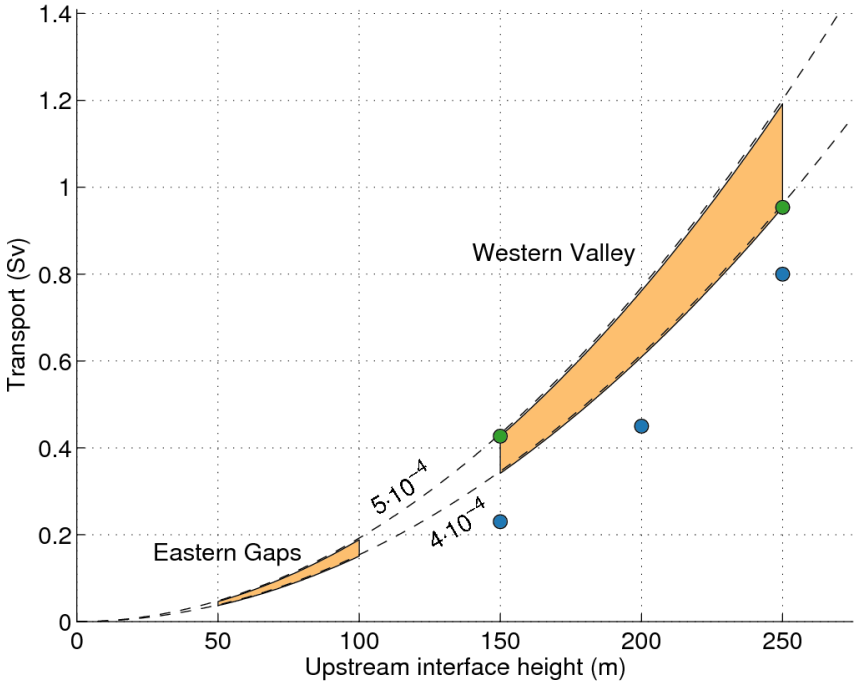

Figure 1.17: *Dependency of the dense water volume transport on the upstream interface height and the density contrast between source water in the Nordic Seas and ambient water as given by Equation 1.3. The coloured areas show the parameter range for the western valley and for each of the eastern gaps in the Iceland-Faroe Ridge. Green dots show the volume transport estimates for the western valley used in the text. Blue dots give the volume transport estimates calculated from the mooring data for different plume heights as shown in Table 1.1.*

when applying Equation 1.3. The density contrast is the same along the whole Iceland-Faroe Ridge with values between $4{\cdot}10^{-4}$ and $5{\cdot}10^{-4}$, but the upstream reservoir height decreases from west to east. Each of the eastern gaps has a transport ranging between 0.05 and 0.2 Sv. With four main gaps besides the western valley, these eastern gaps could thus add up to a minimum of 0.2 Sv and to a maximum of 0.8 Sv. According to Figure 1.17, the complete range for the dense water transport in the western valley is between 0.35 and 1.2 Sv. In the preceding section, it was argued that the choice of a higher isotherm leads to a reduced density contrast, thus the resulting range was between 0.4 and 0.95 Sv.

Summary and conclusions

The temperature and velocity time series recently measured by a mooring south of the Iceland-Faroe Ridge at the Icelandic continental slope show a strong bottom-intensified current with a substantial fraction of overflow water that originates from the Nordic Seas. The volume transport of pure overflow water at the mooring is estimated to be 0.5 ± 0.2 Sv. A seasonal cycle both in velocity and temperature translates into a seasonal variation of the dense water volume transport of ± 0.1 Sv that peaks in early summer.

Using the mean hydrographic conditions upstream of the western valley, an estimate for the overflow volume transport through the western valley applying hydraulic control theory is calculated. The range of the resulting volume transport estimate (0.4 to 0.95 Sv) is of the same magnitude as estimated from the mooring data. The approximate match between the two independent volume transport estimates shown here indicates that the dense water at the mooring site passed the Iceland-Faroe Ridge through the western valley. The slightly higher hydraulic control estimate does not come as a surprise, given that Equation 1.3 was derived to give the maximum transport for a rectangular opening in the ridge. It thus leads to an overestimate of the volume transport and a parabolic shape may be more appropriate (Borenäs and Lundberg, 1988).

Given that hydraulic control theory is applicable, it is also used to calculate an estimate of the dense water volume transport across the eastern part of the Iceland-Faroe Ridge. This results in a volume transport for the eastern gaps that ranges between 0.2 and 0.8 Sv. The total dense water volume transport across the whole Iceland-Faroe Ridge adds up to about 1 Sv with an uncertainty of about ± 0.6 Sv.

The results of this study do not reject the assumption by Olsen et al. (2008) of an overflow volume transport of 1 Sv across the Iceland-Faroe Ridge. This study does not resolve the variability of the total overflow transport across the Iceland-Faroe Ridge, but the seasonal variation of the overflow volume transport through the western valley of 20% suggests that it may not be as stable as assumed by Olsen et al. (2008).

Although the hydraulic control theory seems to produce realistic results when applied to the Iceland-Faroe Ridge, it is questionable whether it really does describe the physics of the overflow, especially in the eastern part. Overflow transport by cold-core meso-scale eddies or meanders of the Iceland-Faroe Front (Hansen and Meincke, 1979) is at odds with a hydraulically controlled overflow.

The peak of the seasonal cycle of the dense water transport at the mooring site approximately matches with the seasonal cycle of the other two overflows east of Iceland. Sherwin et al. (2008) show transport time

series of the Wyville-Thomson Ridge that are greater in summer than in winter but also state that a longer record is needed for confirmation. The peak of transports through the Faroe Bank Channel is in late summer with a variation of 10% from the mean (Hansen and Østerhus, 2007). Thus, the complete dense overflow east of Iceland seems to have a seasonal cycle superimposed. An explanation for this could be the weakening of the internal gyre circulation in the Nordic Seas in summer (Voet et al., 2010), that implies a relaxation of tilted isopycnals due to geostrophy and would lead to a decreased height of the dense water level at the rim of the gyre. This would directly affect hydraulic estimates for the overflow transport.

1.5 Downstream mixing and entrainment of the dense overflow plumes

After crossing the sills of the Greenland-Scotland Ridge, the dense overflow plumes are accelerated by gravity to high flow speeds while they slowly descend to greater depths. During this phase, the overflow plumes are subject to strong mixing and entrainment. The volume transport of the plumes is approximately doubled, while the entrainment of surrounding water masses leads to a modification of temperature and salinity of the overflow water (see scheme in Figure 1.4).

Different processes can drive the entrainment of surrounding water into a fast flowing plume. The vertical velocity shear between ambient water and a plume of high velocity can lead to vertical instabilities that result in breaking internal waves. These lead to turbulent mixing between plume and ambient water. When meso-scale eddies are present in the plume, they can induce lateral stirring, which horizontally transports ambient water into the overflow plume. Figure 1.18 shows examples from experiments with rotating tanks to illustrate these two processes. Other processes that may be considered when studying entrainment are instabilities caused by horizontal velocity shear and Ekman pumping caused by bottom friction of a plume with high velocities close to the bottom.

The processes driving the entrainment have a very small spatial scale. They are not resolved in large scale computer simulations of the ocean circulation and have to be parameterised in the models to aim for the right volume transports and dense water properties of the overturning circulation (Legg et al., 2009). A deeper insight into the processes underlying the entrainment into the overflow plumes is thus essential for the development of parameterisation schemes that significantly improve models of the global ocean circulation.

Two studies within this thesis are dedicated to the understanding of mixing processes and the quantification of their relative importance for the entrainment into the overflow plumes. While the first study aims at the quantification of the contribution of stirring by meso-scale eddies to the entrainment into the Denmark Strait overflow plume (Voet and Quadfasel, 2010), the second study focuses on vertical turbulent mixing in the overflow plume downstream of the Faroe Bank Channel (Fer et al., 2010). After giving an overview of the downstream development of both overflow plumes, the results of these studies will be presented and discussed.

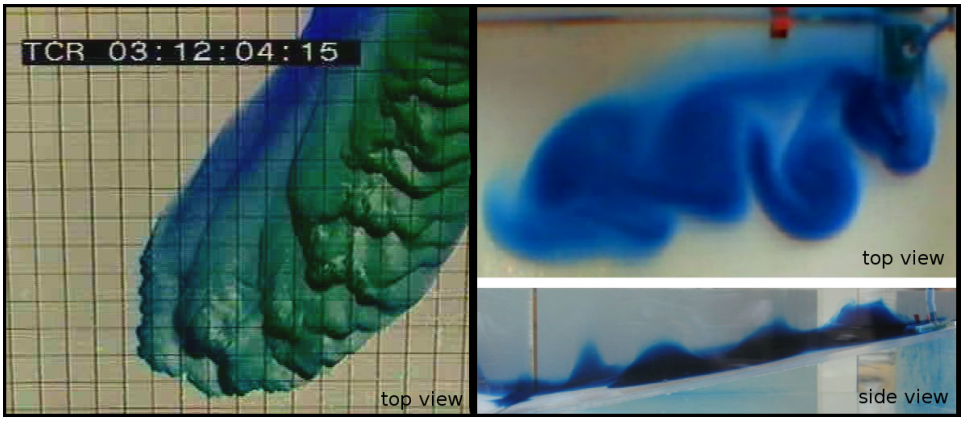

Figure 1.18: *Rotating tank experiments with dense gravity currents on a sloping plane. Left: Water with a high density contrast to the ambient water enters a sloping plane at the upper right. The plane slopes such that it is high at the upper image border and low at the lower image border. The inflowing dense water is dyed to make it distinguishable from the surrounding water. Internal waves at the boundary between the dense plume and the ambient water are visible through variations in the plume colour. Right: Water with a weak density contrast to the ambient water enters a sloping plane. The upper image gives the top view of the plane, the lower image shows a side view to give an impression of the vertical structure of the plume. The slope of the plane seen in the top view is as in the left image. The dense plume breaks up into vortices that stir ambient water into the dense plume.*

1.5.1 Downstream development of the overflow plumes

Downstream of the sill of Denmark Strait, the overflow plume is accelerated by gravity due to its high density contrast to the ambient water. From measurements with expendable profiling instruments, Girton and Sanford (2003) find the maximum overflow speed of about 0.7 m/s approximately 125 km downstream of the sill. This coincides with the region where the overflow plume encounters the steepest bottom topography. If a perfect balance between Coriolis force and gravity was achieved, the plume would approximately follow a line of constant bottom depth. However, bottom and interfacial stresses lead to a downslope migration of the overflow plume with increasing distance from the sill. 500 km downstream of the sill the plume has descended to a depth of about 2000 m.

Current measurements and temperature records of the Denmark Strait overflow plume show a high variability on timescales of 2-5 days close to the sill (Ross, 1984) and 1-12 days about 500 km downstream (Dickson and Brown, 1994). The plume has the structure of pulses that are characterised by strong current velocity and an increase in overflow plume height. These

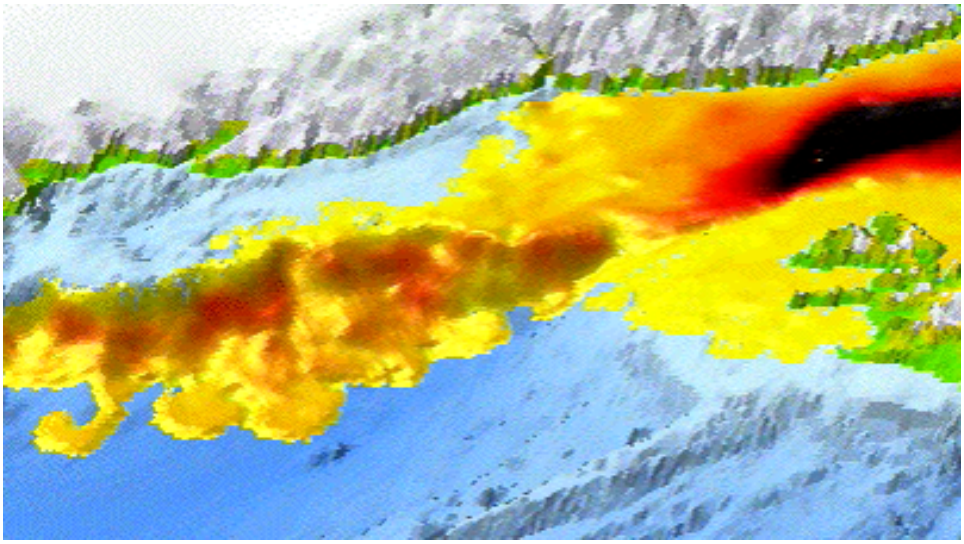

Figure 1.19: *Simulated Denmark Strait overflow plume from* Käse et al. *(2003). Yellow/red/black colouring (in increasing order) indicates the thickness of the dense water layer. The Greenland coast is at the top, Iceland is shown to the right.*

domes of cold water are in rotation and connected to surface eddies observed in satellite infrared imagery (Bruce, 1995; Krauss, 1996) and satellite altimetry (Høyer and Quadfasel, 2001). Regional models of the Denmark Strait overflow with realistic bottom topography are able to reproduce the eddies in the overflow plume and explain their formation with a combination of both baroclinic instability and vortex stretching (Jiang and Garwood, 1996; Krauss and Käse, 1998; Jungclaus et al., 2001; Käse et al., 2003). Figure 1.19 gives an impression of the pulsating and eddying character of the plume downstream of the sill from the model simulation of Käse et al. (2003).

Entrainment into the Denmark Strait overflow plume was first discussed by Smith (1975) who showed a decreasing density contrast between overflow plume and ambient water with increasing distance from the sill. The amount of entrainment becomes apparent in the overflow transport increase from about 3 Sv at the sill to 5.2 Sv at a mooring array located about 300 km downstream from the sill (Dickson and Brown, 1994). Two different entrainment regimes were identified by Girton and Sanford (2003) with weaker entrainment between the sill and 125 km downstream and stronger entrainment thereafter up to a distance of 200 km from the sill. Rudels et al. (1999) observed a low salinity lid of the overflow plume that survived the initial descent after the sill, implying weak vertical mixing as this would destroy the low salinity capping.

After crossing the sill of the Faroe Bank Channel, the overflow plume is still constricted on both sides by the flanks of the Faroe Bank Channel for about 30 km before the channel opens and the bathymetry steepens to the deeper levels of the Iceland Basin. Here, the structure, characteristics and dynamics of the overflow plume change dramatically. It flows as a bottom trapped current along the slope of the Iceland-Faroe Ridge, descends to deeper levels and accelerates locally over steep topography before it decelerates further downstream. Mauritzen et al. (2005) observe velocities that are higher than those at the sill at a section about 100 km downstream of the sill. Several current meters and thermometers moored close to the bottom have shown the mean width of the plume to increase with distance from the sill (Geyer et al., 2006) which is in agreement with studies using hydrographic sections (Duncan et al., 2003; Mauritzen et al., 2005).

The plume is not a steady flowing current as a simple streamtube approximation would suggest (Price and Baringer, 1994). The mooring records of Geyer et al. (2006) have shown highly regular oscillations of velocity and temperature in the overflow plume with a period of 88 hours. Measurements of the vertical plume structure with a thermistor string 100 km downstream from the sill show the plume splitting up into boluses of cold water with a mean height of 200 m that coincide with high velocities (Geyer et al., 2006). This type of variability is also a prominent feature in models by Ezer (2006) and Riemenschneider and Legg (2007). Geyer et al. (2006) and Ezer (2006) identify the oscillations with the wave regime observed in laboratory experiments by Cenedese et al. (2004). In a study by Høyer and Quadfasel (2001) the oscillations about 140 km downstream from the sill were interpreted as meso-scale eddies, observable through enhanced sea level variability in satellite altimeter data. The eddy kinetic energy of the flow was found to be highest 100 km downstream of the sill in their study.

During its descent, the Faroe Bank Channel overflow plume is subject to strong mixing and entrainment. Expressed in plume core temperature, the entrainment results in an increase from below 0°C at the sill to more than 2°C downstream (Quadfasel and Käse, 2007). The overflow plume is situated just beneath the Atlantic layer resulting in a sharp temperature gradient. Thus, entrainment can be very efficient in changing the properties of the overflow water. The geostrophic volume transport increase of the plume calculated from hydrographic sections is 1.1 Sv in a study by Van Aken and Becker (1996). Combining hydrographic and lowered ADCP measurements, Mauritzen et al. (2005) calculate volume transports in different density classes throughout the Faroese Channels and downstream of the sill. They find that the transports downstream are higher and occur in lighter density classes than at the sill. Mauritzen et al. (2005) conclude that entrainment is sufficient to cause an approximate doubling of

the overflow volume transport within 150 km from the sill, a result that is confirmed in high resolution model runs by Riemenschneider and Legg (2007). The hydrographic properties of the plume 150 km downstream already resemble those of the Iceland-Scotland Overflow Water (Mauritzen et al., 2005) that can be traced throughout the Iceland Basin into the Irminger Sea (Swift, 1984).

1.5.2 Two studies on entrainment into the dense overflow plumes

Inspired by the importance of entrainment for the AMOC and the strong eddies observed and modeled in the Denmark Strait overflow plume, the study in Section 2.2 (Voet and Quadfasel, 2010) seeks to answer the question of the contribution of stirring by meso-scale eddies to the overall entrainment in the Denmark Strait overflow plume. Data from mooring arrays at the sill and three different locations downstream are used together with shipboard hydrographic measurements of the overflow plume to calculate integral heat transport balances within the overflow plume and between the overflow plume and the ambient water.

It is found from both, moored thermometers and shipboard temperature measurements, that the mean temperature increase of the overflow plume on the first 200 km from the sill (0.4-0.5 K/100 km) is five to ten times larger than the mean plume temperature increase further downstream (0.05-0.1 K/100 km). The plume temperature increase is associated with entrainment as there is no other heat source for the plume than the inclusion of warmer ambient water. In the area farther away from the sill, mean lateral heat fluxes driven by meso-scale eddies cause a plume warming that is of the same magnitude as the observed plume warming. This leads to the conclusion of an eddy entrainment regime beyond 200 km from the sill where the stirring by meso-scale eddies can explain the total entrainment. It also implies that here little or no vertical mixing is needed to close the balance between observed plume warming and the processes leading to this warming. In the region between the sill and 200 km downstream, the lateral eddy heat fluxes are not large enough to explain the stronger plume warming. It is concluded that here vertical mixing has to play an important role for the entrainment. Taking into account the different entrainment regimes on the first 200 km as found by Girton and Sanford (2003), the regime of vertical mixing can be split up into a region close to the sill with little entrainment and a hot spot region for entrainment between ∼125 and ∼200 km downstream from the sill.

Different regimes of a descending dense plume on a sloping plane, as shown in Figure 1.18, were studied in greater detail in tank experiments by

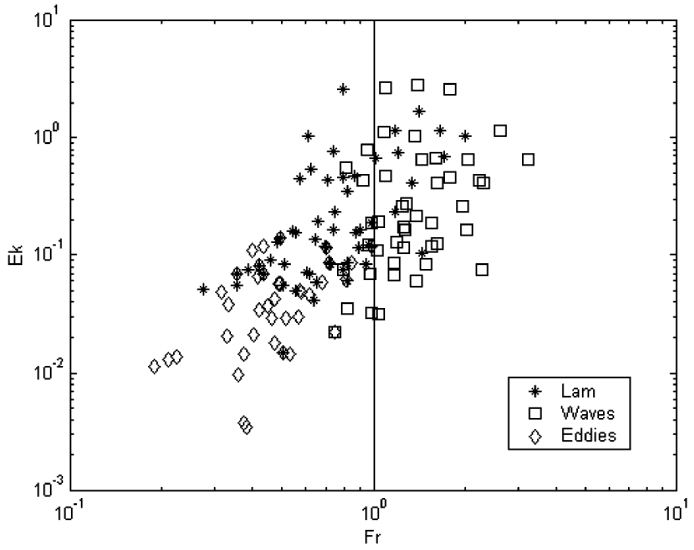

Figure 1.20: *Different regimes (laminar, wave and eddy) for the development of a dense plume on a sloping plane depending on Ekman and Froude number from* Cenedese et al. *(2004). The Ekman number gives the ratio of viscous forces to the forces arising from planetary rotation. The Froude number is a measure for the importance of stratification versus flow speed.*

Cenedese et al. (2004). They observe laminar flow, a wave regime and an eddy regime depending on Ekman and Froude numbers (Figure 1.20). This supports the idea of different entrainment regimes for the Denmark Strait overflow plume. As the plume decelerates due to friction further away from the sill, the Froude number decreases and the driving for the entrainment changes from the wave regime to the eddy regime.

During a survey in June 2008, the entrainment in the Faroe Bank Channel overflow was studied with regard to vertical turbulent mixing (Fer et al., 2010). The study is presented in Section 2.3. The survey concentrated on entrainment into the overflow plume during the first 120 km downstream from the sill. Thus, when translating the results from the Denmark Strait to the Faroe Bank Channel, the survey was carried out in the region where vertical mixing should be more important for the entrainment than stirring by meso-scale eddies.

Six sections of temperature, conductivity, pressure and vertical velocity shear were recorded downstream from the sill of the Faroe Bank Channel with a vertical microstructure profiler (VMP) measuring at very high frequency. The VMP is a free falling instrument that was operated at a profiling speed of about 0.6 m/s. The measurements show enhanced vertical turbulent dissipation in the bottom layer and in a thick interfacial layer which

border the relatively quiescent plume core. The strongest entrainment is found at a distance of about 75 km from the sill. The measurements also show an internal circulation of the overflow plume transverse to the mean flow direction. This internal circulation may lead to lateral entrainment into the plume that could affect the bottom layer while the vertical turbulence can only induce entrainment in the interfacial layer. It is concluded that, due to the high lateral variability and a thick plume interface, neither a bulk parameterisation nor a traditional turbulence closure model will be adequate in representing mixing of the dense plume downstream of the Faroe Bank Channel sill.

1.6 Conclusions and Outlook

This four studies presented in this thesis were aimed at closing some gaps in the understanding of the Nordic Overturning Circulation. In the following I point out the relevance of my results related to processes important for the Nordic Overturning Circulation. The connection with present and upcoming research projects regarding the interannual to decadal variability of either components or the total Nordic Overturning Circulation is shown. These are the time scales relevant for the detection of changes in the AMOC as predicted by climate projections.

Ventilation The study of the mid-depth circulation internal to the Nordic Seas shows a strong topographic steering of the flow field. The internal recirculation observed in the deep basins is at least twice as strong as the exchange with the subpolar North Atlantic. Wind forcing is suggested to be the dominant driving force for the seasonal variability of the gyre strengths in the Greenland and Norwegian Basin.

What is the implication of the dominating wind forcing over the Greenland and Norwegian Basin for the long term variability of the circulation? How could this affect the production of overflow water? An increasing wind stress curl would speed up the gyres, leading to an increase in energy available for the exchange between gyres and rim current. Thus, more dense water feeding the overflows across the Greenland-Scotland Ridge could be produced in this case, although it may then not be as dense as presently.

The research of hydrography and circulation in the Nordic Seas, and of the dynamics and budgets of the water mass transformation, will be fostered by the sustained deployment of Argo floats. The floats are provided within the framework of Euro-Argo, a project of the European Union with the objective to deploy, maintain and operate a large array of profiling floats. Results of Voet et al. (2010) have contributed to the deployment strategy for floats in the Nordic Seas. Longer time series available from the floats will in the future allow (1) to extend the analysis of this study from seasonal to decadal time scales and (2) to apply the method of Latarius and Quadfasel (2010) to all four basins of the Nordic Seas to explicitly study their contribution to the overflow water production in the Nordic Seas.

Overflows Using hydraulic control theory, a dense water volume transport of about 1 Sv was found in the study on the overflow across the Iceland-Faroe Ridge. Approximately half of the overflow water passes through the western valley that cuts through the Iceland-Faroe Ridge at the Icelandic continental slope, the other half crosses the ridge through

the eastern gaps. While the uncertainty of this new estimate for the overflow transport across the Iceland-Faroe Ridge is still large with ±0.6 Sv, it confirms the commonly cited mean transport of 1.1 Sv that was based on few hydrographic observations in the 1950's (Hermann, 1967). In contrast, the present study is based on two-year long current measurements and a large number of hydrographic profiles collected over several decades.

Apart from the seasonal variation of about 20% found for the overflow transport through the western valley, the data set is still not sufficient for a quantification of the variability of the total Iceland-Faroe Ridge overflow transport. How could the mean overflow across the Iceland-Faroe Ridge and especially its variability be assessed in greater detail? A monitoring of the Iceland-Faroe Ridge overflow using moored instrumentation along the ridge crest would be a labour-intensive and expensive undertaking, given the large width of the passage. Repeat surveys with sea gliders along the southern slope of the ridge have proven to be useful for estimating mean overflow transports downstream of the Faroe-Bank Channel. The gliders were also operated over the Iceland-Faroe Ridge (Nick Beaird, personal communication), but their low speed makes them unsuitable for a monitoring of the Iceland-Faroe Ridge overflow. As the overflow transport through the Faroe Bank Channel and its associated entrainment downstream are quantified to a high degree, an integral measurement of both overflows at the continental slope south of Iceland may be suited to reveal the strength of the Iceland-Faroe Ridge overflow.

The measurement of interannual up to decadal variability remains an open question for all overflows across the Greenland-Scotland Ridge. Elucidating this issue is one amongst other objectives of the EU project THOR (Thermohaline Overturning - at Risk?). One part of THORs observational component is the deployment of instruments to investigate key features of the shallow overflows across the Wyville-Thomson Ridge and the Iceland-Faroe Ridge. A suggestion resulting from my study is a deployment of an ADCP closer to the sill of the western valley where less entrainment has occurred than at the mooring whose data was analysed here. This could tighten the conclusion of overflow water passing through the western valley with a magnitude that can be predicted from upstream hydrographic conditions.

Entrainment Both studies regarding mixing in the dense overflows give a consistent picture of the downstream evolution of the dense overflow plumes in Denmark Strait and the Faroe Bank Channel. The initial descent and the region of high plume velocities is accompanied by strong vertical mixing. Farther away from the sills the plumes break

up into eddies that can cause entrainment by lateral stirring. While the two studies were carried out for two different overflow plumes, they suggest these different regimes to be general features of their associated entrainment. The results of both studies show that a simple parameterisation of entrainment that is only based on vertical velocity shear and density difference is not sufficient.

The contribution of eddies to the entrainment into the Faroe Bank Channel overflow plume has not been quantified yet, but several mooring arrays were deployed downstream the sill during a cruise in June 2008, whose data could be used for a study similar to Voet and Quadfasel (2010). Likewise, during a cruise in Denmark Strait in 2009, microstructure measurements have been performed that allow a study of turbulent mixing similar to Fer et al. (2010). First results (Paka et al., 2010) indicate strong vertical turbulent mixing in the area predicted by Voet and Quadfasel (2010).

An important question is the relationship between overflow transport at the sill and associated entrainment downstream. A comparison between overflow transport time series from the Denmark Strait sill and a mooring array approximately 500 km downstream shows that the two time series differ significantly on time scales up to annual, but are correlated on interannual time scales (Dickson et al., 2008). This suggests that entrainment varies together with the overflow strength on long time scales. It might not hold for lower transports, e. g. one may think of lower plume velocities or density thresholds below which vertical instabilities do not occur.

The interannual variability of entrainment in the Denmark Strait overflow plume is the topic of a Diploma thesis that is underway. It builds upon the results of Voet and Quadfasel (2010) and Høyer and Quadfasel (2001). The latter show the connection between eddies in the overflow plume and sea surface height variability visible in satellite data. The thesis aims at the relation between meso-scale kinetic energy in the overflow plume, entrainment and sea surface height variability over a period of more than ten years.

Chapter 2

Papers

2.1 Paper I: The mid-depth circulation of the Nordic Seas from profiling float observations

Tellus SERIES A DYNAMIC METEOROLOGY AND OCEANOGRAPHY
PUBLISHED BY THE INTERNATIONAL METEOROLOGICAL INSTITUTE IN STOCKHOLM

Tellus (2010)

TELLUS

The mid-depth circulation of the Nordic Seas derived from profiling float observations

By G. VOET[1]*, D. QUADFASEL[1], K. A. MORK[2] and H. SØILAND[2], [1]*Institut für Meereskunde, KlimaCampus, University of Hamburg, Bundesstr. 53, 20146 Hamburg, Germany;* [2]*Institute of Marine Research and Bjerknes Centre for Climate Research, Bergen, Norway*

(Manuscript received 10 July 2009; in final form 10 March 2010)

ABSTRACT

The trajectories of 61 profiling Argo floats deployed at mid-depth in the Nordic Seas—the Greenland, Lofoten and Norwegian Basins and the Iceland Plateau—between 2001 and 2009 are analysed to determine the pattern, strength and variability of the regional circulation. The mid-depth circulation is strongly coupled with the structure of the bottom topography of the four major basins and of the Nordic Seas as a whole. It is cyclonic, both on the large-scale and on the basin scale, with weak flow ($<1\,\mathrm{cm\,s^{-1}}$) in the interior of the basins and somewhat stronger flow (up to $5\,\mathrm{cm\,s^{-1}}$) at their rims. Only few floats moved from one basin to another, indicating that the internal recirculation within the basins is by far dominating the larger-scale exchanges. The seasonal variability of the mid-depth flow ranges from less than $1\,\mathrm{cm\,s^{-1}}$ over the Iceland Plateau to more than $4\,\mathrm{cm\,s^{-1}}$ in the Greenland Basin. These velocities translate into internal gyre transports of up to $15 \pm 10 \times 10^6\,\mathrm{m^3\,s^{-1}}$, several times the overall exchange between the Nordic Seas and the subpolar North Atlantic. The seasonal variability of the Greenland Basin and the Norwegian Basin can be adequately modelled using the barotropic vorticity equation, with the wind and bottom friction as the only forcing mechanisms. For the Lofoten Basin and the Iceland Plateau less than 50% of the variance can be explained by the wind.

1. Introduction

The Nordic Seas, comprising the area between Greenland, Spitsbergen, Norway, Iceland and the Faroe Islands, are a marginal sea with great importance for the Atlantic Meridional Overturning Circulation. Atmospheric conditions in this area lead to a transformation of inflowing warm and buoyant surface water into cold and dense deep water masses (Mauritzen, 1996) that eventually feed the overflows across the Greenland–Scotland Ridge into the subpolar North Atlantic (Hansen and Østerhus, 2000). The circulation within the Nordic Seas is essential for the deep water formation as it transports the inflowing surface water northwards, redistributes the water within the Nordic Seas and supplies the overflows with the dense water to be exported.

The near-surface circulation of the Nordic Seas was studied with drogued surface drifters by Poulain et al. (1996), Orvik and Niiler (2002) and Jakobsen et al. (2003). They find a general cyclonic circulation with meridional boundary currents and additional cyclonic circulation patterns in the Greenland Basin, the Norwegian Basin and the Iceland Plateau. The surface drifters confirm the tight link between surface circulation and bottom topography that was already noted by Helland-Hansen and Nansen (1909) in their fundamental study of the Nordic Seas.

Our knowledge about the mid-depth and deep circulation of the Nordic Seas stems mainly from water mass analyses, current observations with moored instrumentation and model studies. The basin structure of the Nordic Seas (Fig. 1) with closed f/H contours and the weak stratification leads to a strong topographic steering of the flow field. This led Nøst and Isachsen (2003) to develop a simplified diagnostic model for the Nordic Seas and the Arctic Ocean that is driven by climatological wind forcing and a climatological density field. It solves for a bottom flow field which compares well with available direct current observations. The number of these direct current measurements at depth is limited for the interior of the Nordic Seas as most current meter studies concentrated on the in- and outflows to and from the Nordic Seas. An exception is the study of Woodgate et al. (1999) who deployed moorings at the continental slope east of Greenland that extended into the deeper parts of the Greenland Basin. They find evidence for a recirculation internal to the Greenland Sea that is intensified towards the edge of the basin.

Several studies show an intensification of the Nordic Seas' internal circulation in winter. This seasonal variability is found

*Corresponding author.
e-mail: gunnar.voet@zmaw.de
DOI: 10.1111/j.1600-0870.2010.00444.x

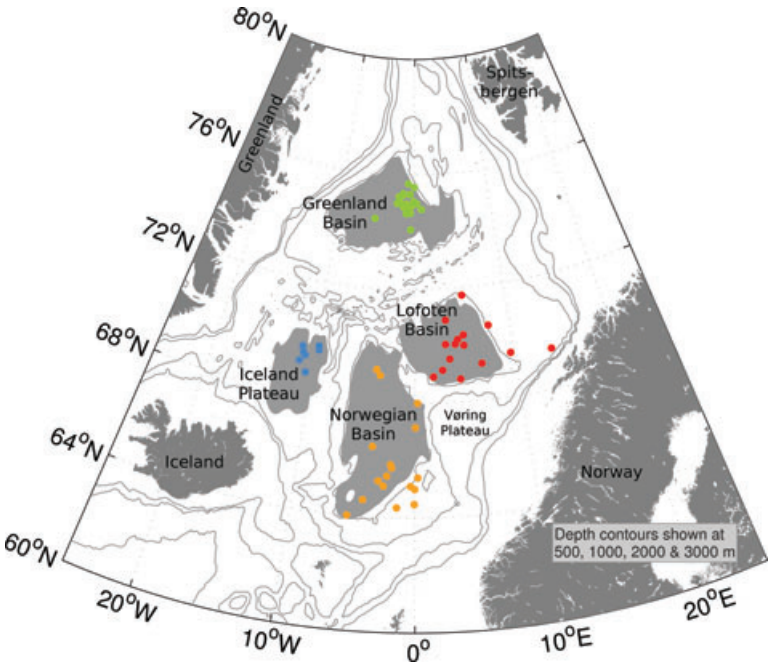

Fig. 1. Float deployment positions in the four major basins of the Nordic Seas. Deployments took place between 2001 and 2008. The area of closed bottom contours is shown in grey for each basin. The encircling depth contours are about 1600 m for the Iceland Plateau and about 3000 m for the Greenland, Lofoten and Norwegian Basins.

in the surface circulation (Jakobsen et al., 2003), in current meter records at the Greenland shelf break (Woodgate et al., 1999), in the steric height of the water column (Mork and Skagseth, 2005) and in a diagnostic model by Isachsen et al. (2003). Contrary to these indications for a strong seasonal variability of the Nordic Seas circulation, the dense overflows across the Greenland–Scotland Ridge are remarkably stable on time scales longer than a few weeks. No seasonal variability was found in the overflow through Denmark Strait and it is only intermittent in the Faroe Bank Channel (Quadfasel and Käse, 2007).

Since 2001 current measurements have been made in the Nordic Seas by use of profiling Argo floats. The floats drift at depths of 1000 and 1500 m and this allows one to study the mid-depth flow below the upper Atlantic and Polar layers in detail. The main questions we want to answer are (1) What is the mean pattern of the circulation at mid-depth? (2) Is there a seasonal cycle in the strength of the deep circulation—similar to that in the surface layer—that contrasts the stability of the dense overflows? and (3) What are the driving mechanisms for the mid-depth circulation of the Nordic Seas?

The paper is structured as follows. Section 2 gives an overview over the data used in this study, the method for calculating the deep drift of the floats and an error estimate thereof. In Section 3, we analyse the topographic steering of the flow field before we calculate the time-mean circulation scheme at depth in Section 4. The seasonal variability of the gyres in the basins and forcing mechanisms are analysed in Section 5. Conclusions are drawn in Section 6.

2. Data and methods

2.1. Float data set

Within the Argo project a total of 61 profiling floats have been deployed in the Nordic Seas through February 2009. The aim of Argo is to establish a global array of profiling floats in the world oceans providing hydrographic data to estimate the large-scale geostrophic flow field (Roemmich et al., 1999). Profiling floats are autonomous drifters equipped with sensors to record vertical profiles of temperature, conductivity and pressure and in certain cases even more parameters like oxygen and fluorescence (Gould, 2005). Floats are passive drifters in the horizontal, but they can adjust their buoyancy to control their vertical movements. Most of the time the floats stay at a parking depth that is set prior to their deployment. The floats deployed in the Nordic Seas were programmed for a parking depth of 1000 m except for seven floats in the Norwegian and Lofoten Basin that were set to a parking depth of 1500 m. After drifting at their parking depth for around 9 d, the floats descend to 2000 m, ascend to the surface while recording a profile of the water column, stay at the surface for 5 h to transfer their data and position to a satellite until they descend back to the parking depth. This whole cycle takes 10 d and is repeated by the floats until eventually the lifetime of their batteries is reached.

Profiling floats were deployed in all basins of the Nordic Seas (Fig. 1). The deployments started in summer 2001 and more than 4100 profiles were obtained by these floats through the last data update for this study in February 2009. The positions of

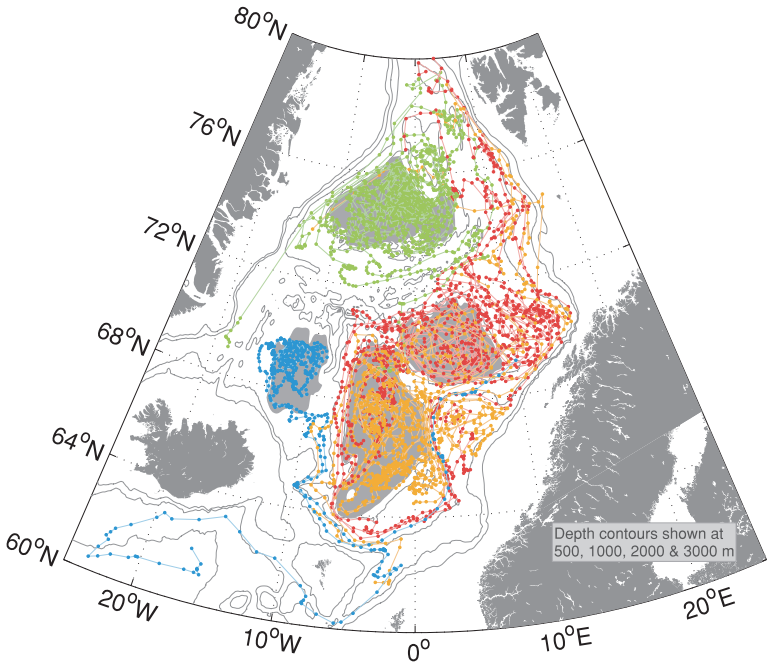

Fig. 2. Positions of all profiles recorded by the floats in the Nordic Seas. The colours of the profile positions correspond to the basin they were deployed in (see Fig. 1).

all profiles recorded by the floats are shown in Fig. 2. With the growing number of floats in the Nordic Seas the data density increased from around 15 profiles per month in the early years to around 70 profiles per month at present (Fig. 3).

We use the surface position data of the floats to estimate the flow field at mid-depth. In principle, these measurements are not truly Lagrangian, due to the surfacing of the floats every 10 d and the inability of the floats to follow vertical motion, but the drift of a float during one cycle is still a sound measurement of the water mass pathway integrated over 10 d. This is shown in a comparison between drifts measured by acoustically tracked RAFOS floats and profiling floats by Machín et al. (2006). Their study shows no significant difference between the

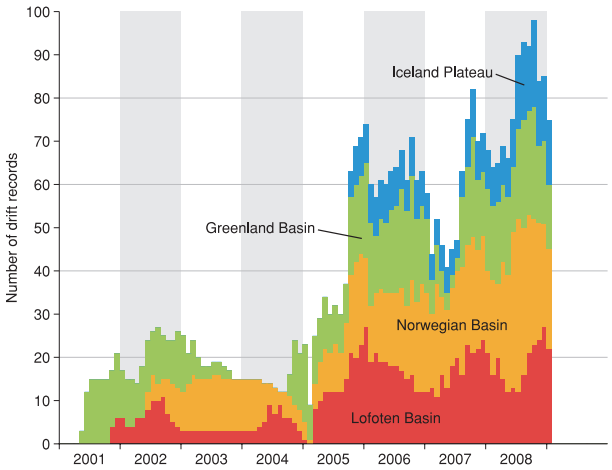

Fig. 3. Number of profiles per month recorded by the floats for each basin of the Nordic Seas.

results from the two instrument types, the only drawback of the profiling floats being that eddy variability at short time scales is not resolved. The surfacing of the floats even has an advantage. It improves statistics compared to the RAFOS floats as it leads to a decorrelation of the single displacements at depth and thereby increases the number of degrees of freedom (Davis, 1998).

All observations deriving from the two different float parking depths were treated as mid-depth and no recalculation of the 1500 m data has been done to lift them up to 1000 m. Below the relatively warm and saline Atlantic and the cold and fresh Arctic water masses at the surface, the stratification in the Nordic Seas is weak. The largest depth reached by the Atlantic water masses is found in the Lofoten Basin with approximately 800–900 m (Orvik, 2004). Thus, below 900 m geostrophic shear should be weak. Calculations with the float profile data from the Nordic Seas confirm that between 1000 and 1500 m the velocity difference is less than 0.3 cm s^{-1} except for a small area in the Lofoten Basin where it can be up to 0.7 cm s^{-1}. We therefore treat both parking depths as one level.

In certain cases of shallow bathymetry the floats may hit the bottom and get stuck when attempting to descend to the profiling depth of 2000 m. This happened only after the drift at the parking depth and in all cases the sensors showed no sign of a delayed ascent to the surface thereafter, indicating that no trapping of floats at the seafloor occurred.

2.2. *Estimating the deep drift from surface positions*

To calculate the drift of a float at depth, we take the last surface position before its descent to the parking depth, the first

surface position after the ascent back to the surface and the time interval between these two positions. The drift velocity then is the distance between the two positions divided by the time interval. We define the location and time of the velocity observation as the mid-point between the diving and surfacing points. Two main error sources have to be considered when the surface positions of the floats are used to infer the drift at depth. These are the uncertainty of the position fix and the velocity shear the float encounters on its passage between surface and depth.

The uncertainty of the position fix is influenced by two factors, the technically limited accuracy of the satellite positioning system and the non-continuous measurement of the surface position. The accuracy of the CLS-Argos positioning system is always better than 1500 m with a mean uncertainty of 800 m for all position data used in this study. This corresponds to a velocity error of less than 0.2 cm s^{-1}. The mean distance that a float covers within one subsurface cycle is 35 km, the median is 28.5 km (Fig. 4). Thus, the error arising from positioning inaccuracy is less than 5% for most of the measurements, except for very low drift velocities and hence short drift distances. The measurement interval of the surface position depends on the frequency of satellite overpasses. A long time interval between the position measurements can lead to a considerable time lag between the real surfacing position of the float and the first position fix by the satellite. The same holds for the diving position. Park et al. (2005) developed a routine that extrapolates the surfacing and diving positions from the positions fixed by the satellite and thereby increases the accuracy of the deep drift estimate. We do not use this method for two reasons. First, the large satellite coverage at the high latitudes of the Nordic Seas reduces the mean time interval between single position fixes to only 14 min. This results in an uncertainty of the real diving and surfacing position that is smaller than the spatial uncertainty of the position fix itself. Second, the method of Park et al. (2005) requires the exact surface arrival time that usually is part of the metadata. Unfortunately, this data set is incomplete for our Nordic Seas floats. We therefore simply use the first and last position fix, treating them as the real surfacing and diving points.

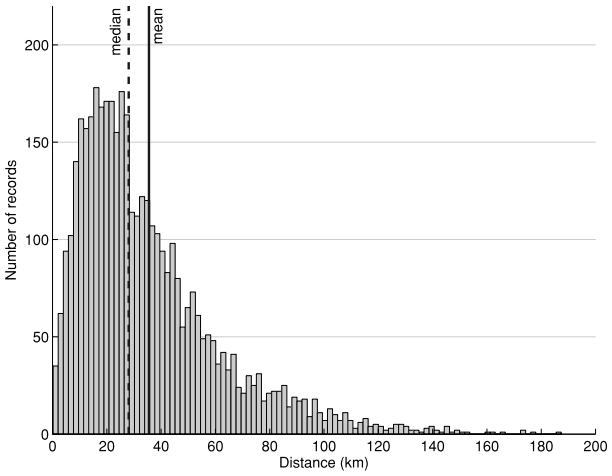

Fig. 4. Histogram of the distances covered by the floats during individual cycles. The straight line shows the mean of the distribution, the dashed line gives the median.

A simple approach for estimating the influence of the velocity shear between surface and depth on the calculation of the drift velocity at depth is a linear interpolation between surface and deep velocity (Lebedev et al., 2007). The mean surface velocity during the time interval the float stays at the surface, calculated by a least squares fit to the surface positions, is 20 cm s^{-1}. The mean velocity at depth, calculated from all float displacements, is about 4 cm s^{-1}. Thus, during the 2 × 7 h of ascent and descent between surface and parking depth the mean velocity is 12 cm s^{-1}. With the mean vertical velocity of a float of 0.08 dbar s^{-1} this results in a maximum displacement of about 5 km during the round-trip between depth and surface. This is the upper limit for the error deriving from velocity shear which may not be reached in all cases.

Surface velocities are dominated by Ekman drift and inertial currents that influence only the upper part of the water column. As the float is at the surface for only five hours the contribution of inertial currents to the surface flow is random in its direction. An analysis of the wind direction over the Nordic Seas shows that it is randomly distributed over the Norwegian and Lofoten Basins while over the Greenland Basin and the Iceland Plateau winds from the north are dominating. Consequently, the Ekman drift is also randomly directed in the Norwegian and Lofoten Basins while it is expected to have a preferred direction in the Greenland Basin and Iceland Plateau. When averaging over a number of records, the influence of inertial currents and, at least for the Norwegian and Lofoten Basins, the Ekman drift is expected to cancel out.

We tested the influence of the surface velocity on the deep velocity estimate by omitting the surfacing completely, i.e. by only taking one random surface position per surfacing. With the deep drifts calculated from these positions only, the results reported in this paper are only slightly altered. This supports the assumption of the surface velocities being, at least to some extent, random noise that averages out when calculating mean values from a larger number of observations.

There is another factor that may systematically decrease our velocity estimate. We assume the deep drift to be a straight line between the two surface position fixes. The topographic steering of the flow in the Nordic Seas (see below) should lead to a more complex path of the flow that can only be of equal length or longer than a straight line. We cannot account for this underestimate in our velocity calculation as we are lacking any position information between the surface position fixes. When comparing the float measurements with Eulerian measurements from moorings this effect has to be kept in mind.

2.3. Wind stress data

To estimate the atmospheric wind forcing over the Nordic Seas, NCEP/NCAR-reanalysis data (Kalnay et al., 1996) are used. The NCEP/NCAR-reanalysis assimilates a multitude of observations into a model to produce a homogeneous data set of many atmospheric and oceanic variables. A comparison with QuikSCAT wind fields, a data set derived from active radar measurements of the sea surface roughness, has shown that the NCEP/NCAR-reanalysis data represents the surface winds over the Nordic Seas well in terms of low- and high-frequency variability (Kolstad, 2008). We use the 6-hourly momentum flux data set to calculate the wind stress curl over the Nordic Seas.

2.4. Bottom topography

The ETOPO2 bathymetry with a resolution of two minutes is used to assign bottom depths and topographic gradients to the float displacements. For the region of the Nordic Seas, ETOPO2 consists of the Smith and Sandwell bathymetry (Smith and Sandwell, 1997) south of 64°N and the International Bathymetric Chart of the Arctic Ocean (IBCAO, Jakobsson et al., 2000) north of 64°N. For the calculation of bottom gradients we smoothed the topography at the length scale of the float displacements (Thomson and Freeland, 2003). The mean displacement for all Nordic Seas floats is about 30 km and we remove scales smaller than 40 km.

3. Topographically influenced mean flow

The floats have the tendency to stay in the basin where they were deployed in (Fig. 2). On average 75% of all float positions stem from the deployment basin while the remaining 25% are located in one of the other basins. There is some organized exchange through the opening between the Norwegian and Lofoten Basin with floats leaving the Norwegian Basin with the rim current in the southern part of the opening. Floats only transfer from the Lofoten into the Norwegian Basin in the northern part of the opening. Furthermore, some floats leave the Lofoten Basin in the rim current towards Fram Strait, one float leaves the Greenland Basin southward in the rim current. The floats' stay in the Iceland Plateau is rather short, and most of them escape towards the southeast into the Norwegian Basin within one to 2 yr. One float from the Iceland Plateau even made its way through the Faroe Bank Channel into the subpolar North Atlantic. However, the Iceland Plateau is an exception and the floats mostly stay in the basin they were deployed in.

In general the floats follow lines of constant bottom depth. Examples for single trajectories can be found in Gascard and Mork (2008) and Søiland et al. (2008). In Fig. 2 the positions of two floats above the only 1000–1500 m deep Vøring-Plateau off the Norwegian coast between the Lofoten and Norwegian Basin show that they were trapped there. This indicates again the topographic steering of the flow field as the floats and thus the water cannot move away from the relatively shallow plateau into deeper areas.

Given the strong topographic steering we project the measured drift velocities onto the bathymetry. This gives us velocity components along and across the local topography instead of north and east components. The convention here is that for the along bathymetry component, positive values have the shallow bottom on the left side irrespective of the basin.

Figure 5 shows the distributions of the along and across bathymetry velocity components of all drift records, both for regions of strong and weak topographic gradients. They differ in two aspects. First, the distribution of the along component is broader compared to that of the across component. Thus the variation of the along topography flow is larger than that of the across component. Mesoscale variability is expected to be isotropic and the variance of the currents in both along and across bathymetry direction should be equal. The larger along topography variance indicates that another process is acting on this component. Below we will show, that the increase of variance is due to the seasonal cycle of the flow. Second, while the across component is distributed around zero, the along component is shifted towards negative velocities, most pronounced in the rim currents. This negative shift of the along bathymetry component corresponds to a mean cyclonic circulation. The corresponding distributions for the individual basins show the same structure in each of the four basins.

The dependence of the along bathymetry velocity component on the size of the bottom slope is shown in Fig. 6. While single data points exhibit a large variability, the bin-averaged values show an increase of the velocity with steeper bottom slope. The

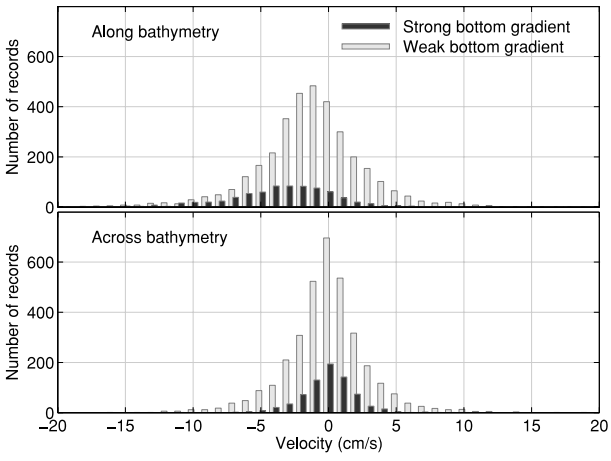

Fig. 5. Histogram of the velocity components along bathymetry (upper panel) and across bathymetry (lower panel) with distinction between velocities over strong (>0.015) and weak bottom gradient (≤0.015). The mean values for both distributions of the across component are not significantly different from zero while for the along component the mean values are -3.5 cm s^{-1} over strong and -1.3 over weak bottom gradient.

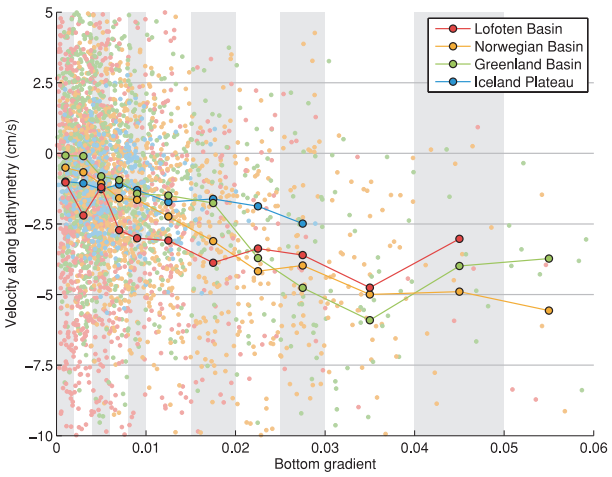

Fig. 6. Dependency of the along bathymetry velocity component on the bottom gradient for the four basins. Individual observations are marked with small dots. Not all individual data points are shown in this figure. The individual observations averaged into bottom gradient bins are shown with bold markers. For weak bottom gradients, where many observations are available for averaging, the width of the bins is smaller than for strong bottom gradient, where the data is sparse.

velocity is negative which stands again for cyclonic flow. The intensification of the flow with increasing bottom gradient is evident in all four basins of the Nordic Seas. The average over all basins shows a linear increase of the velocity with the bottom gradient until a maximum value is reached at a gradient of about 0.03. From thereon, the mean velocity is approximately constant.

The dependence of the current velocity at depth on the size of the local bottom gradient confirms the results of Nøst and Isachsen (2003). They show that within closed f/H contours the bottom velocity is dependent on the local slope of the f/H field and on the integrated forcing within that contour. We will come back to the latter point when analysing the forcing of the seasonal variability of the circulation.

4. Time-mean mid-depth circulation

4.1. Mean circulation scheme

For the construction of a mean circulation map at the float parking depth the data set is averaged over the whole period 2001–2009. The map is calculated by assigning each float observation to the nearest point of a rectangular grid with the size of one degree latitude, i.e. about 110 km. The calculation of the distance between observation and grid point takes the topographic steering of the flow into account. It thus models the longer correlation scales along bottom topography. Following Davis (1998), the effective distance r between float observation and grid point is calculated as

$$r^2 = |\mathbf{x}_a - \mathbf{x}_b|^2 + \left| 3\lambda \frac{H_a - H_b}{H_a + H_b} \right|^2, \qquad (1)$$

where the first term on the right-hand side gives the geographical distance between observation and grid point. Here $\mathbf{x}_a$ denotes the position of the grid point and $\mathbf{x}_b$ the position of the mid-depth observation. The second term with the bottom depths H_a and H_b at the points $\mathbf{x}_a$ and $\mathbf{x}_b$ increases the effective distance according to the difference in bottom depth between observation and grid point. The topography parameter λ was chosen to be 100 km as in Lavender et al. (2005). The bottom depths for the calculations were obtained from the smoothed ETOPO2 bathymetry data set. After assigning each observation to its nearest grid point, the mean velocity and direction at each grid point are calculated as the mean over all observations the grid point comprises.

The resulting pattern of the mid-depth circulation is shown in Fig. 7. Velocity vectors are only shown at grid points where at least five data points are available. Figure 8 gives the number of observations that were used in the calculation of the mean velocity vectors. Cyclonic gyres are found in each of the basins. They are intensified towards the rims. In the centre of the basins the velocities are relatively small and more randomly directed. The largest variability (not shown) is found at the rim while it is low in the centre of the basins. An exception is the Lofoten Basin where the variability in the centre is almost as high as at the rims. As already indicated in Fig. 2, we do not find a strong mean advection between the basins of the Nordic Seas. Exceptions are the export of floats from the Iceland Sea to the Norwegian Basin and some exchange between Lofoten and Norwegian Basin due to gaps in the topographic barrier between these two basins. The small exchange of floats between the basins does not mean that there is no exchange of water masses between the basins though. Transports can happen in narrow, jet-like currents that floats are not capable of covering adequately.

The circulation at mid-depth generally has the same pattern as the surface circulation shown in the study by Jakobsen et al. (2003). They also find cyclonic recirculation in the Greenland Basin, the Iceland Plateau and the Norwegian Basin. Their surface flow pattern in the Lofoten Basin is directed northwards at the eastern and western edge of the basin and thus has both a cyclonic and anticyclonic component. This is in contrast to our finding of a strong cyclonic gyre at mid-depth and implies a considerable shear between surface and mid-depth flow in the western part of the Lofoten Basin. The mid-depth circulation found here is also very similar to the model results of Nøst and Isachsen (2003) who show a scheme of the bottom-near circulation in the Nordic Seas. This confirms their simple and elegant model and also agrees with the few mooring current measurements they used to validate their model output. The small and randomly directed velocities in the centre of the gyres agree with the mooring records from the Greenland Basin of Woodgate et al. (1999).

For an estimate of the statistical robustness of the mean circulation scheme we calculate the statistical uncertainty of the mean velocities following Lavender et al. (2005) as the covariance of each average divided by the number of degrees of freedom in

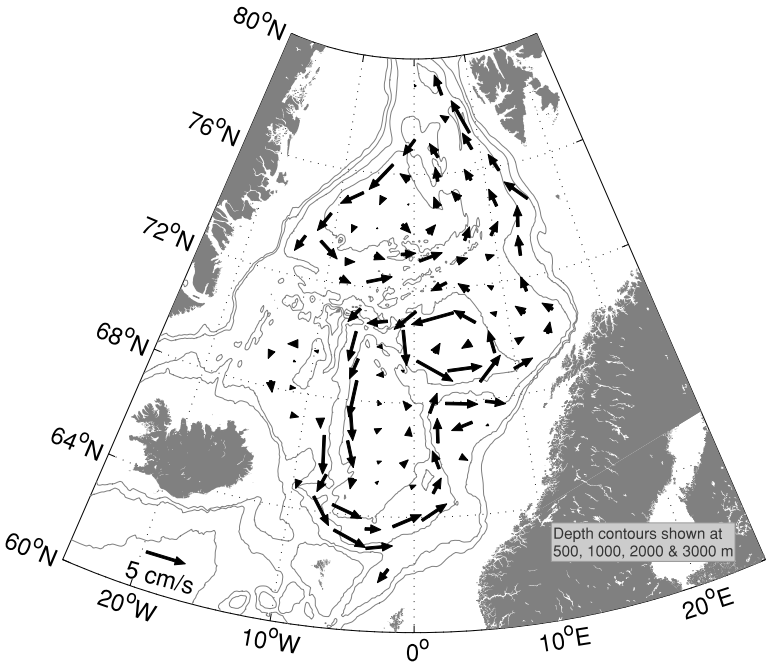

Fig. 7. Time-mean mid-depth circulation of the Nordic Seas on a rectangular grid with a size of 110 km. Only mean values calculated from more than five observations are shown.

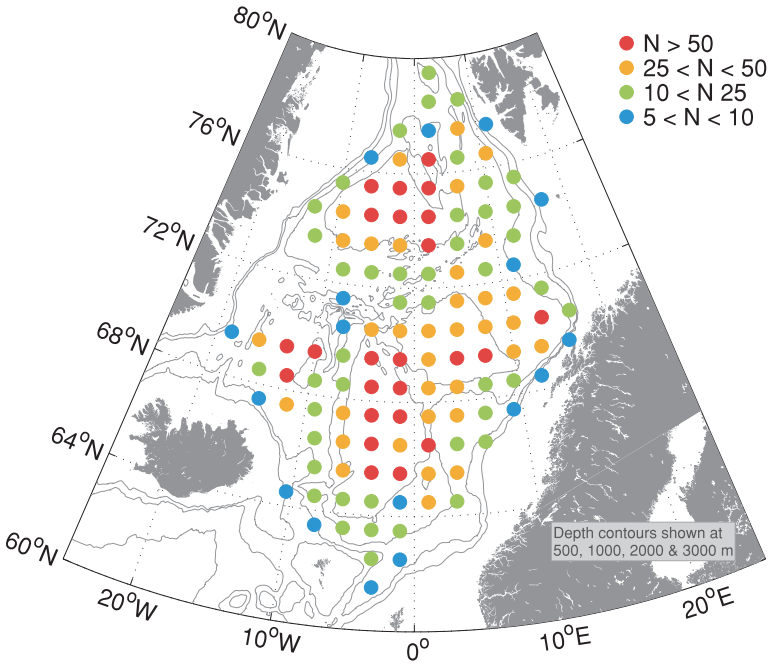

Fig. 8. Number of observations per grid cell used for the calculation of the mean velocities.

the average. Each observation contributes a degree of freedom unless it is correlated with another observation in the same grid cell. For different floats there is no correlation as the floats did not encounter each other close enough in time and space. For a single float, successive observations may very well be correlated with each other. However, the time lagged autocorrelation for single floats in our data set shows that the observations are decorrelated after about 10 d, indicating that consecutive subsurface drifts are essentially uncorrelated. A conservative estimate of the Lagrangian integral time scale is to take the decline in the autocorrelation in both directions. This results in a time scale of about 20 d. Dividing the time a single float spends in a grid cell by this decorrelation time scale gives the degrees of freedom it contributes. A decorrelation time scale of 20 d is consistent with the results of Lavender et al. (2005) who also use this value for the double-sided decorrelation time scale. The statistical

uncertainties calculated with this integral time scale show that most mean velocities are significant. Only few mean velocities in the centre of the basins are smaller than their statistical uncertainty.

4.2. Topostrophy

It is instructive to study the topographical steering of the flow with a single scalar parameter. Killworth (1992) introduced such a parameter to measure the alignment of the flow with bottom topography. Holloway et al. (2007) termed this parameter topostrophy. The topostrophy T is defined as the vertical component of the cross product of velocity vector and bottom gradient:

$$T = (\vec{v} \times \vec{\nabla} H)_z, \tag{2}$$

Topostrophy is positive for cyclonic flow and negative for anticyclonic flow. It is zero for a current perpendicular to local isobaths. We define the normalised topostrophy $\hat{T}$ as

$$\hat{T} = \frac{(\vec{v} \times \vec{\nabla} H)_z}{|\vec{v}| \cdot |\vec{\nabla} H|}. \tag{3}$$

The normalized topostrophy derived from the float velocity data set confirms the general cyclonic circulation at mid-depth in the Nordic Seas (Fig. 9). This holds particularly for the rim currents in the basins. In the interior of the basins, gradients of local topography are weak and the flow is less aligned with bottom contours. The strongest alignment with the bottom topography is found over the Iceland Plateau and in the western and southern part of the Norwegian Basin. These two areas also show relatively strong positive topostrophy away from the rim current. Slightly negative topostrophy in the centre of the Lofoten Basin and the associated anticyclonic flow confirms the findings of Köhl (2007), who detected a permanent anticyclonic 'Lofoten Vortex' in a high resolution regional model simulation.

5. Seasonal variability

5.1. Seasonal signal in the float velocity data

Previous studies of currents in the Nordic Seas revealed considerable variability on the seasonal time scale. Jakobsen et al. (2003) find an intensification of the surface flow in winter of order of 5 cm s^{-1}. Transports calculated from mooring records in the Greenland Sea (Woodgate et al., 1999) and in the Norwegian Basin (Orvik et al., 2001) are stronger in winter than in summer. Mork and Skagseth (2005) studied the seasonal variability in bottom speeds calculated from altimeter data and hydrographic data. They find a spin-up of the gyres in winter and spring in the Greenland, Norwegian and Lofoten Basin, with the highest seasonal variability in the Norwegian Basin of about 1 to 2 cm s^{-1}.

We use our float data set to estimate the strength of the seasonal cycle of the circulation at mid-depth. At the beginning of 2009, the number of observations is yet insufficient to detect the temporal variability at the spatial resolution used for our mean circulation map (Fig. 7). We therefore calculate the monthly mean gyre velocities in a geographic frame to construct velocity time series for the individual basins. The monthly mean velocity in a basin gyre is defined here as the average over all along bathymetry velocities recorded in the rim areas of the basins during one month. Figure 10 shows the data points at the rim in each basin used for the calculation. For the Greenland and Norwegian Basin, the area between the 1000 and 3000 m isobath is chosen to represent the rim of the gyres. In the Lofoten Basin we define the rim as the area between 2800 and 3200 m

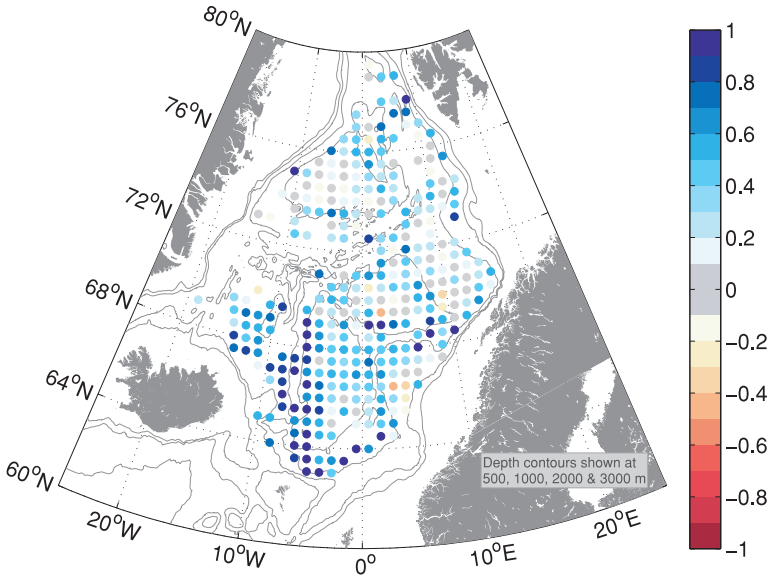

Fig. 9. Normalised topostrophy derived from the mean circulation scheme. Blue colours stand for cyclonic flow, red colours for anticyclonic flow. The closer the absolute value of the normalized topostrophy tends towards one, the more the flow is aligned to the bathymetry.

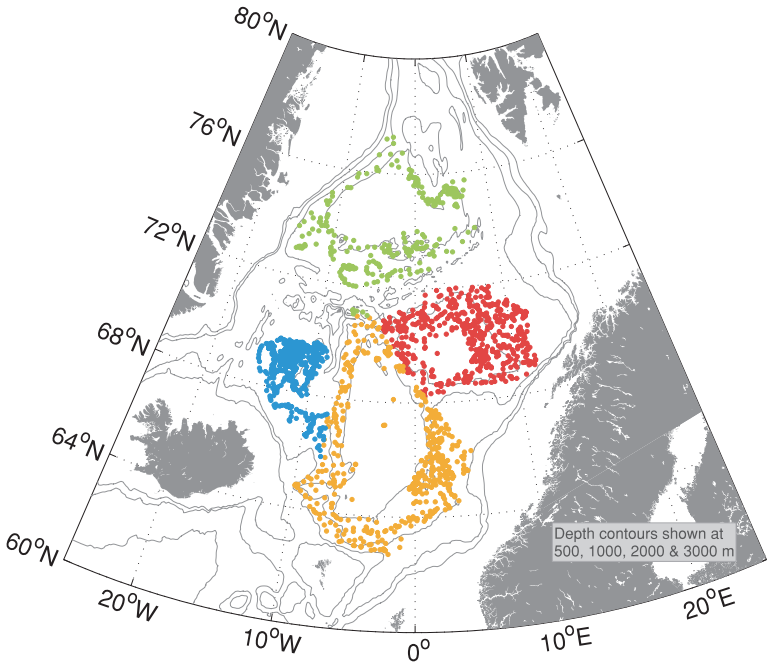

Fig. 10. Observations used to calculate mean velocities of the basin gyres. Observations between the 1000 and 3000 m isobaths were chosen to be representative for the rim in the Greenland and Norwegian Basin. In the Lofoten Basin the area between the 2800 and 3200 m depth contours defines the rim of the basin. For the Iceland Basin the whole area deeper than 1000 m is chosen.

bottom depth. This discards data at the very eastern edge of the Lofoten Basin that are not associated with the gyre circulation. For the analysis of the Iceland Plateau gyre all data are used, as it is not possible to define a rim on the relatively shallow plateau. Figure 11 shows the number of observations per month that are available for the calculation of gyre velocities in each of the basins. Using different rim definitions, as for example 2000–3000 m for the Norwegian and Greenland Basin, does not change the results in a qualitative way but only results in a small change in the amplitude of the seasonal cycle.

The rationale for using only rim data is twofold. First, velocities in the centre of the gyres are small and often not aligned with topography. This can be seen in the mean mid-depth circulation scheme (Fig. 7). Second, when analysing the forcing of the seasonal variability below, we will use a barotropic vorticity equation to describe the temporal evolution of the basin gyre velocities. In this equation, the velocities at the rim of the gyres are used.

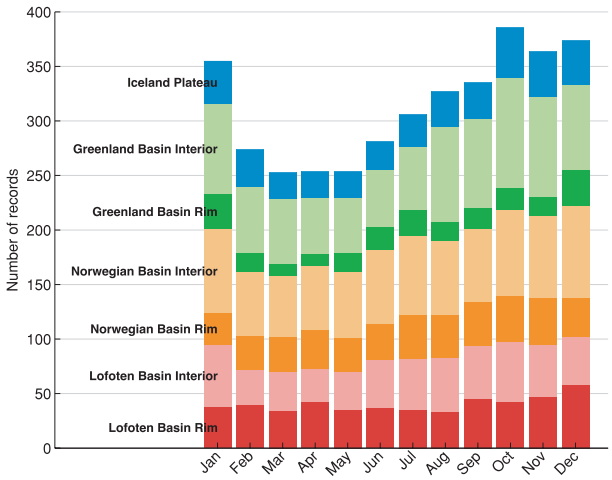

Fig. 11. Number of records used for the calculation of the monthly mean basin gyre velocities.

The method of calculating monthly mean gyre velocities from the float observations is problematic due to the position and time of the deployment of the floats. Most floats were deployed in the centres of the basins (Fig. 1) during cruises that took place between late spring and early autumn. This uneven distribution in space and time may have an influence on the calculation of monthly mean velocities. By taking observations at the rim of the basins only, the problem of the deployment positions is minimized.

The monthly mean gyre velocities for the four basins are shown in Fig. 12. A low-pass filter (weighted three point average) is used to smooth the data for the seasonal analysis. The Greenland Basin has a seasonal cycle with higher velocities in winter and a minimum velocity in late summer as has the Norwegian Basin. The peak-to-peak amplitude of the seasonal variability is about 3 cm s^{-1} for the Greenland Sea and 1.5 cm s^{-1} for the Norwegian Basin. In the Norwegian Basin, a semi-annual cycle seems to be superimposed on the seasonal cycle. The observations over the Iceland Plateau also show lower velocities in summer than in winter, but the amplitude is small with only about 0.5 cm s^{-1}. This low amplitude matches with the low mean velocities found over the Iceland Plateau (Figs 6 and 7).

In the Lofoten Basin we do not find a clear seasonal cycle as in the other basins. Here low velocities occur in winter and maxima are seen in early summer and early winter. Peak-to-peak changes

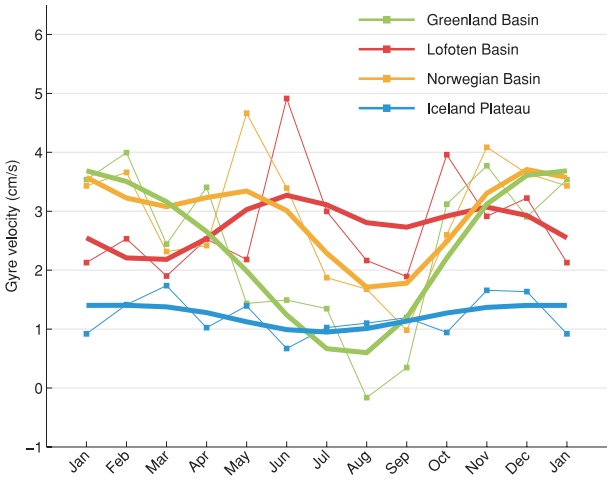

Fig. 12. Seasonal variability of the gyre velocity in the four basins. The gyre strength is defined as the mean velocity along the bathymetry at the rim of the gyre. Thin lines with markers give monthly mean values, thick lines show a low-pass filtered version (weighted three-point average) of the monthly values. The standard deviation for the monthly mean values (not shown in the figure) is about 4–6 cm s^{-1} for all months and basins. This statistical uncertainty reflects the mesoscale variability that is not resolved by the measurement cycle of the floats of around ten days.

are just over 1 cm s^{-1}. This is quite in contrast to the pattern in the other basins which may have several reasons: On the one hand, it is not clear whether this result is still influenced by the many observations from the eastern part of the basin (Fig. 10). The scheme of the time-mean circulation (Fig. 7) shows that the flow diverges in this area. In addition, the eastern part of the Lofoten Basin is an area of high eddy kinetic energy (Gascard and Mork, 2008) that could influence the calculation of the mean gyre velocity. On the other hand, the layer of warm Atlantic water spreads over the whole surface area of the Lofoten Basin and deepens considerably. This could lead to forcing mechanisms different from the other basins resulting in a different seasonal cycle. We come back to this when analysing the forcing of the seasonal variability by the wind stress below.

5.2. *Wind forcing*

The mean wind forcing over the whole Nordic Seas is cyclonic and has a pronounced seasonal cycle (Jónsson, 1991). Figure 13 shows the monthly mean wind stress curl for each basin of the Nordic Seas calculated for the period when floats were present in the basin. These periods are also representative for the complete 60 yr NCEP record except for the Iceland Plateau where the wind stress curl in March and November is considerably smaller in the float period. Overall the mean wind stress curl has a clear seasonal cycle. The maximum of the curl occurs in winter while it is almost zero in the summer months. The strength of the seasonal momentum forcing is largest in the Greenland Basin and smallest over the Norwegian Basin. Our float observations fall into a period with a moderately high (0.5) NAO Index. The state of the NAO is very important for the wintertime wind speeds in the Nordic Seas, with a high correlation between positive NAO Index and wintertime wind speeds (Kolstad, 2008). Numeric simulation results of Serra et al. (2010) also show the correspondence between decreasing NAO Index and less cylonicity of the Nordic Seas gyre circulation.

5.3. *Forcing of the circulation*

The ocean has a barotropic and a baroclinic response to the wind forcing by radiating barotropic and baroclinic planetary waves. The time scale for the adjustment of a basin of the size of the Nordic Seas at high latitudes is several years for the baroclinic waves but only some days for the barotropic waves. Thus, the seasonal variability of the wind forcing cannot be compensated by baroclinic oceanic processes and only a barotropic response of the ocean to the wind forcing can be expected.

From weather maps, Aagaard (1970) calculated monthly mean Sverdrup transports for the Nordic Seas and found transports exceeding 30 Sv (1 Sv = 10^6 m^3 s^{-1}) at the western boundary of the Nordic Seas. He assigns this strong transport to the internal gyre recirculation. The variability between different months is large in his calculations. However, the order of 30 Sv, also estimated by Jónsson (1991) from wind observations, agree with estimates from current measurements (Aagaard, 1970; Woodgate et al., 1999), suggesting that the wind field is able to maintain the internal gyre circulation, at least at the western boundary in the Greenland Sea. Mork and Skagseth (2005) study the relation of the wind forcing over the Norwegian Basin to the observed seasonal cycle of the bottom flow speed. Using a harmonic fit to both cycles, they show that the phase of the wind forcing is able to explain the observed changes in the flow speed.

To analyse the influence of the wind forcing on the seasonal variability of the flow field derived from the float data (Fig. 12) we use a vertically integrated stream function describing the vorticity input to the Nordic Seas. The use of a vertically integrated stream function is justified as the stratification in the Nordic Seas is weak. With the stream function Ψ of the vertically integrated volume transport and a rigid lid approximation, Marotzke and Willebrand (1996) obtain the equation for the barotropic vorticity

$$\frac{\partial}{\partial t}\left(\vec{\nabla}\cdot\frac{1}{H}\vec{\nabla}\Psi\right)+\vec{\nabla}\Psi\times\vec{\nabla}\frac{f}{H} = \vec{\nabla}\times\frac{\vec{\tau_w}-\vec{\tau_b}}{H}+\vec{\nabla}E\times\vec{\nabla}\frac{1}{H}+\ldots \quad (4)$$

with wind stress $\vec{\tau_w}$ divided by surface density, bottom stress $\vec{\tau_b}$, bottom depth H and the potential energy E of the stratification. The second term on the right is the bottom torque that expresses

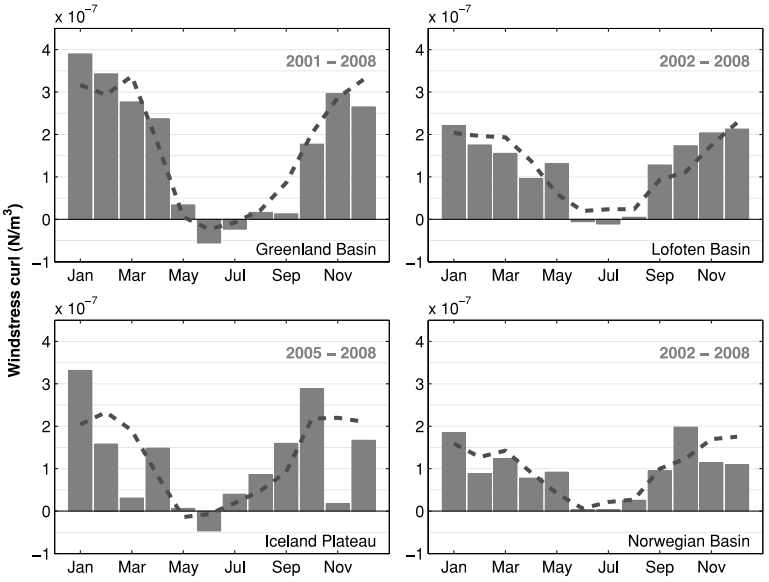

Fig. 13. Monthly mean wind stress curl integrated over the basins of the Nordic Seas (bars). The wind stress curl is calculated from NCEP/NCAR reanalysis momentum fluxes. The time periods used to calculate the mean values correspond to the time that floats stayed within the basin. The dashed lines show the seasonal cycle of the wind stress curl for the whole 60 years of the NCEP/NCAR reanalysis period 1948–2008. The area of the basins is defined by the 1200 m depth contour for the Iceland Plateau, by the 1000 m isobaths for the Greenland and Norwegian Basins and by the 2800 m depth contour for the Lofoten Basin.

the effect of potential energy gradients along lines of constant bottom depth. Non-linear terms are neglected here. The steady state solution of this equation for a basin with constant bottom depth is the well-known Sverdrup relation.

The integration around closed f/H contours simplifies the barotropic vorticity equation. The bottom torque term involves the Jacobian with $1/H$ and vanishes identically when integrated around a closed f/H contour. Isachsen et al. (2003) show in their model of the Nordic Seas that the bottom torque term is in fact small compared to the other terms. Using Stokes' theorem, the barotropic vorticity equation can be reduced to

$$\frac{\partial}{\partial t}\oint_C \vec{v}\mathrm{d}\vec{r} = \int_A \frac{\vec{\nabla}\times(\vec{\tau_w}-\vec{\tau_b})}{H\rho_0}\mathrm{d}A. \tag{5}$$

This relates the temporal change of the barotropic velocity integrated around a closed contour C to the curl of wind and bottom stress integrated over the area A confined by C.

All terms of the simplified barotropic vorticity equation can be calculated using the float measurements of the seasonal cycle of the basin gyre velocities and the reanalysis data for the wind forcing. The bottom drag is calculated from the gyre velocities observed by the floats applying a linear drag law

$$\vec{\tau}_b = R\cdot\vec{v}. \tag{6}$$

Here we assume that the observed mid-depth velocities are also representing the near bottom velocities. The unknown drag parameter R is finally derived by optimising the sum of wind and bottom drag to the observed velocity change. This gives drag parameters for each basin in the range between 5×10^{-4} and $10\times10^{-4}\,\mathrm{m\,s^{-1}}$ which is of the same order of magnitude used in the model of Isachsen et al. (2003).

As f varies only little at these high latitudes, depth contours are used instead of f/H contours for the integrals around C and over A. To be consistent with the velocity calculations we use the same basin definitions as above—1000 m for the Greenland and Norwegian Basins, 2800 m for the Lofoten Basin and 1200 m for the Iceland Plateau.

When the variability in the system is driven by the wind and bottom friction only, the sum of these two should match the observed changes of the gyres on the seasonal time scale. Figure 14 compares the observed change of the gyre velocities (left-hand side of eq. 5) with the sum of wind forcing and bottom drag (right-hand side of eq. 5). For the Greenland and Norwegian Basins, where a seasonal cycle in the gyre velocity with a minimum in summer was observed, the wind forcing explains a large part of the observed seasonal variability. The correlation between observation and the sum of wind and bottom drag is about 0.8 in the Greenland Basin with a time lag of 2 months and also about 0.8 in the Norwegian Basin with a time lag of 1 month. This mismatch in the phasing of the signal may stem from processes not considered in our analysis. Mixed layer deepening and convection is strongest during late winter, about 3–4 months after the maximum momentum forcing. At least in the Greenland Basin this buoyancy forcing leads to an enhanced doming of the deeper water column inducing cyclonic rotation of the layer. This enhances the local baroclinic flow, acting against the weakening barotropic gyre circulation.

Processes other than the wind forcing seem to play an even more important role in the Lofoten Basin where the correlation between observed velocity change and the sum of wind and bottom drag terms is always below 0.5, no matter which time lag is applied. For the Iceland Plateau the match between observation and wind forcing is small in our analysis. The velocity change was calculated over the whole area of the Iceland Plateau and not just at the rim as should be used in eq. (5). Therefore we cannot tell whether the misfit for the Iceland Plateau is due to

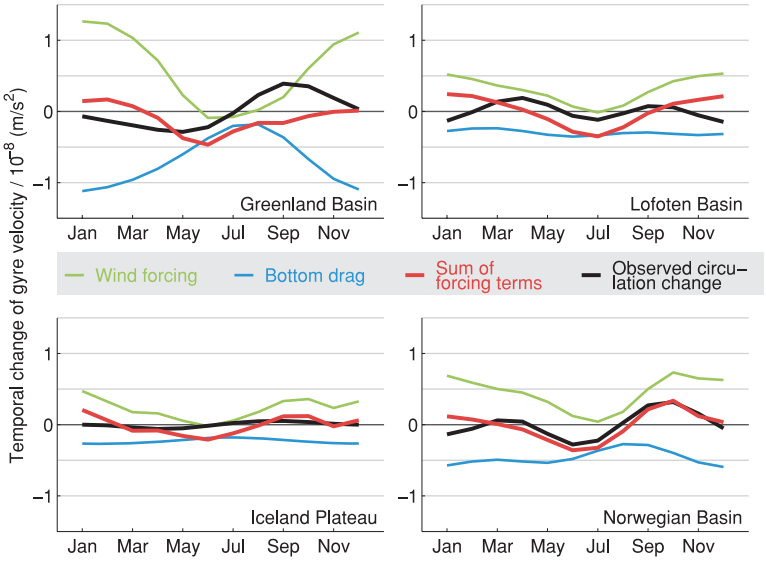

Fig. 14. Comparison of observed seasonal changes of the basin gyre circulation (black) and calculated changes from forcing terms (red). The wind forcing term is shown with the green line and the bottom friction with the blue line. The three-point weighted average version was used for all terms shown here.

the wrong velocity observation used in the analysis or associated with real oceanic processes.

The importance of the wind forcing, at least for the Norwegian and Greenland Basins, is supported by the model study of Isachsen et al. (2003) who find wind forcing more important than hydrographic (thermal wind shear) forcing for flow along f/H-contours on time scales from monthly to annual.

6. Summary and conclusions

In this paper, we have analysed the trajectories of 61 autonomous profiling floats that were deployed within the international Argo programme in the Nordic Seas between 2001 and 2009. Based on 10-d subsurface drifts between consecutive surfacing of the floats we have studied both the mean circulation at mid-depth (1000–1500 m) and its seasonal variability.

The floats were initially deployed near the centres of the four basins—the Greenland, Lofoten and Norwegian Basins and the Iceland Plateau (Fig. 1). It turned out that float diffusion between the basins was small and most floats stayed within their home topographic structure throughout their lifetime (2–5 yr). There were regional differences, though. The Greenland Basin appears to be very isolated while the two eastern basins, being swept by the northward flowing Atlantic water, suffered a larger loss of floats to their neighbours. In all, however, only 25% of the floats escaped and moved to another basin or region. This certainly indicates that the overall mean advection in the Nordic Seas is limited to the narrow boundary currents and the exchanges between the gyres and the boundary flow are dominated by diffusive processes, such as mesoscale or submesoscale processes rather than advection.

The forcing for the Nordic Seas circulation consists of three mechanisms that are drivers for a cyclonic circulation: momentum forcing, heat fluxes and freshwater input. The Nordic Seas are exposed to strong momentum forcing, with the Greenland High and the Icelandic Low being the permanent features of the atmospheric pressure pattern. Both, buoyancy and momentum forcing, drive the cyclonic circulation internal to the Nordic Seas that may be viewed as a northern extension of the North Atlantic's Subpolar Gyre, albeit with regional characteristics due to the limited exchange across the Greenland–Scotland Ridge. Momentum and buoyancy forcing are both characterized by large seasonal variability. Winter heat fluxes to the atmosphere may reach 300–400 W m^{-2} whereas during summer the ocean is gaining heat at a rate of up to 150 W m^{-2}. River run-off is largest in spring, after snow melt. Likewise, the momentum fluxes, expressed as the curl of the wind stress, range between 0 and 4×10^{-7} N m^{-3} in summer and winter, respectively.

The mid-depth flow in all basins is cyclonic, which is consistent with the surface flow (Jakobsen et al., 2003). This does not really come as a surprise, given the three cyclonic forcing mechanisms. Near the rim of the basin gyres mean current speeds are 1–3 cm s^{-1} whereas in the centres they are reduced to less than 1 cm s^{-1}. Overall the flow pattern documents the tight topographic control of the circulation as a result of the weak stratification. The velocities (see Fig. 6) translate into mean internal gyre transports of up to 15 Sv, several times the overall exchange between the Nordic Seas and the subpolar North Atlantic.

The seasonal variability of the gyre circulation within the Greenland and Norwegian Basins is large and in magnitude comparable to that of the mean flow. The tight phase link to the momentum forcing suggests that the seasonal circulation is a barotropic response to the winds and that baroclinic effects like convection only play a minor role for setting up the currents on the basin scale. When balancing the vorticity input by the winds with the losses due to linear bottom friction we estimate drag coefficients between 5 and 10×10^{-4} m s^{-1},

reasonable values that fall into the same range as those used in numerical model simulations. Estimated transport variability is up to 15 ± 10 Sv, a value confirmed by earlier direct current measurements using moored instrumentation (Woodgate et al., 1999). Over the Iceland Plateau the seasonal wind forcing is less pronounced compared to the Greenland Sea. Here the gyre circulation shows the smallest seasonal variations, consistent with the forcing. Also, the topographic gradients are much weaker than in the other basins and the flow may not be subject to as rigorous a topographic control as in the other regions. In addition, our database here is smallest and it may not be sufficient to detect the variability.

The largest deviation from our simple barotropic response model occurs in the Lofoten Basin. The gyre circulation here contains a strong semi-annual component comparable in magnitude to the seasonal signal. The reason for this is not clear to us. The forcing, wind and bottom friction, is clearly seasonal, but the float exchange with the Norwegian Basin in the South and the continental slope region in the West Spitsbergen Current in the North suggest a weaker topographic control of the flow. Results from a numerical model simulation confirm this behaviour (Serra et al., 2010). The Lofoten Basin is a region of enhanced mesoscale variability generated by baroclinic instabilities of the flow, first described by Helland-Hansen and Nansen (1909) as puzzling waves and also observed in drifter studies (Poulain et al., 1996; Jakobsen et al., 2003; Rossby et al., 2009). These baroclinic effects may also play a role in setting up the circulation, but our data set does not allow to explore such mechanisms.

The Nordic Seas are a region of intense water mass transformation. Here, through heat loss, freshwater input and melting and freezing of sea ice, buoyant Atlantic Water is transformed into buoyant (cold, low salinity) near surface waters and dense (cold, intermediate salinity) intermediate and deep waters. The surface waters leave the Nordic Seas via Denmark Strait and enter the subpolar North Atlantic as a narrow and shallow boundary current (about 2 Sv, Sutherland and Pickart, 2008) on the East Greenland shelf and continental slope. The dense waters exit into the subpolar Atlantic in different pathways via the overflows across the Greenland–Scotland Ridge, mainly through Denmark Strait and the Faroe Bank Channel. This exchange is limited by topographic (hydraulic) control and presently the Nordic Seas contribute only about 6 Sv (Quadfasel and Käse, 2007) to the North Atlantic Deep Water.

Direct current measurements over the Greenland–Scotland Ridge show that the Nordic Loop of the Subpolar Gyre of the North Atlantic has a strength of about 8 Sv. Seasonal variability of these exchanges across the ridge is small and amounts to 1 Sv at most (Hansen and Østerhus, 2007). In contrast, the internal horizontal circulation cells in the Nordic Seas that are linked to the four topographic basins are at least twice as strong as the overall exchange, with their seasonal variability exceeding that of the ridge exchanges by an order of magnitude.

The main role of the Nordic gyres thus is the transformation of buoyant surface water into dense deep and intermediate water. This process and the associated circulation set up and maintain fronts. Instabilities of the fronts then provide the energy for meso- and submesoscale stirring and mixing, transferring the transformed water masses from the gyres' interior to the boundary currents. These eventually feed the overflows into the North Atlantic.

7. Acknowledgments

Rolf Käse provided valuable comments on the first draft of this manuscript. The financial support for this study by Deutsche Forschungsgemeinschaft (SFB 512 E2) and the European Commission (Euro-Argo and Mersea) is gratefully acknowledged. These funding agencies also provided most of the Nordic Seas floats. Globally Argo data are collected and made freely available by the International Argo Project and the national programs that contribute to it (http://www.argo.ucsd.edu, http://argo.jcommops.org). Argo is a pilot program of the Global Ocean Observing System.

References

Aagaard, K. and Coachman, L. K. 1968. The East Greenland Current north of Denmark Strait. Part I. *Arctic* **21**(3), 181–200.

Aagaard, K. 1970. Wind-driven transports in the Greenland and Norwegian Seas. *Deep-Sea Res.* **17**, 281–291.

Davis, R. E. 1998. Preliminary results from directly measuring mid-depth circulation in the tropical and South Pacific. *J. Geophys. Res.* **103**(C11), 24619–24639.

Gascard, J.-C. and Mork, K. A. 2008. Climatic Importance of Large-Scale and Mesoscale Circulation in the Lofoten Basin Deduced from Lagrangian Observations. In: *Arctic-Subarctic Ocean Fluxes*, (eds R. R., Dickson, J., Meincke and P., Rhines), Springer, Dordrecht, 131–143.

Gould, W. J. 2005. From Swallow to Argo—the development of neutrally buoyant floats. *Deep-Sea Res. Part I* **52**, 529–543.

Hansen, B. and Østerhus, S. 2000. North Atlantic-Nordic Seas exchanges. *Prog. Oceanogr.* **45**, 109–208.

Hansen, B. and Østerhus, S. 2007. Faroe Bank Channel Overflow 1995-2005. *Prog. Oceanogr.* **75**, 817–856.

Helland-Hansen, B. and Nansen, F. 1909. The Norwegian Sea: Its Physical Oceanography based on Norwegian Researches. Report on Norwegian Fishery and Marine Investigations 11, 390 pp. + 25 plates.

Holloway, G., Dupont, F., Golubeva, E., Häkkinen, S., Hunke, E. and co-authors. 2007. Water properties and circulation in Arctic Ocean models. *J. Geophys. Res.* **112**(C4), C04S03.

Isachsen, P. E., LaCasce, J. H., Mauritzen, C. and Häkkinen, S. 2003. Wind-driven variability of the large-scale recirculating flow in the Nordic Seas and Arctic Ocean. *J. Phys. Oceanogr.* **33**, 2534–2550.

Jakobsen, P. K., Ribergaard, M. H., Quadfasel, D., Schmith, T. and Hughes, C. W. 2003. Near-surface circulation in the northern North Atlantic as inferred from Lagrangian drifters: variability from the mesoscale to interannual. *J. Geophys. Res.* **108**(C8), 3251.

Jakobsson, M., Cherkis, N., Woodward, J., Coakley, B. and Macnab, R. 2000. New grid of Arctic bathymetry aids scientists and mapmakers. *EOS, Trans. Am. Geophys. Un.* **81**(9), 89.

Jónsson, S. 1991. Seasonal and interannual Variability of Wind Stress Curl Over the Nordic Seas. *J. Geophys. Res.* **96**(C2), 2649–2659.

Kalnay, E., Kanamitsu, M., Kistler, R., Collins, W., Deaven, D. and co-authors. 1996. The NCEP/NCAR 40-Year Reanalysis Project. *B. Am. Meteorol. Soc.* **77**(3), 437–472.

Killworth, P. D. 1992. An equivalent-barotropic mode in the fine resolution antarctic model. *J. Phys. Oceanogr.* **22**, 1379–1387.

Köhl, A. 2007. Generation and stability of a quasi-permanent vortex in the Lofoten Basin. *J. Phys. Oceanogr.* **37**, 2637–2651.

Kolstad, E. W. 2008. A QuikSCAT climatology of ocean surface winds in the Nordic seas: identification of features and comparison with the NCEP/NCAR reanalysis. *J. Geophys. Res.* **113**, D11106.

Lavender, K. V., Owens, W. B. and Davis, R. E. 2005. The mid-depth circulation of the subpolar North Atlantic Ocean as measured by subsurface floats. *Deep-Sea Res. Part I* **52**, 767–785.

Lebedev, K. V., Yoshinari, H., Maximenko, N. A. and Hacker, P. W. 2007. YoMaHa'07: Velocity data assessed from trajectories of Argo floats at parking level and at the sea surface. *IPRC Tech. Rep.* **4**(2), 16 pp.

Machín, F., Send, U. and Zenk, W. 2006. Intercomparing drifts from RAFOS and profiling floats in the deep western boundary current along the Mid-Atlantic Ridge. *Sci. Mar.* **70**(1), 1–8.

Marotzke, J. and Willebrand, J. 1996. The North Atlantic mean circulation: combining data and dynamics. In: *The Warm water sphere of the North Atlantic Ocean* (eds W. Krauss et al.), Borntraeger, Berlin, Stuttgart, 55–90.

Mauritzen, C. 1996. Production of dense overflow waters feeding the North Atlantic across the Greenland-Scotland Ridge. Part 1: evidence for a revised circulation scheme. *Deep-Sea Res. Part I* **43**, 769–806.

Mork, K. A. and Skagseth, Ø. 2005. Annual Sea Surface Height Variability in the Nordic Seas and Arctic Ocean estimated from simplified dynamics. In: *The Nordic Seas: An Integrated Perspective* (eds H. Drange, T. Dokken, T. Furevik, R. Gerdes and W. Berger), Geophys. Monogr. Ser. **158**, AGU, Washington DC, 51–64.

Nøst, O. A. and Isachsen, P. E. 2003. The large-scale time-mean ocean circulation in the Nordic Seas and Arctic Ocean estimated from simplified dynamics. *J. Mar. Res.* **61**, 175–210.

Orvik, K. A. 2004. The deepening of the Atlantic water in the Lofoten Basin of the Norwegian Sea, demonstrated by using an active reduced gravity model. *Geophys. Res. Lett.* **31**, L01306.

Orvik, K. A. and Niiler, P. 2002. Major pathways of Atlantic water in the northern North Atlantic and Nordic Seas toward Arctic. *Geophys. Res. Lett.* **29**, 1986.

Orvik, K. A., Skagseth, Ø. and Mork, M. 2001. Atlantic inflow to the Nordic Seas: current structure and volume fluxes from moored current meters, VM-ADCP and SeaSoar-CTD observations, 1995–1999. *Deep-Sea Res. Part I* **48**, 937–957.

Park, J. J., Kim, K., King, B. A. and Riser, S. 2005. An advanced method to estimate deep currents from profiling floats. *J. Atmos. Ocean. Tech.* **22**, 1294–1304.

Poulain, P.-M., Warn-Varnas, A. and Niiler, P. P. 1996. Near-surface circulation of the Nordic seas as measured by Lagrangian drifters. *J. Geophys. Res.* **101**(C8), 18237–18258.

Quadfasel, D. and Käse, R. 2007. Present-Day Manifestation of the Nordic Seas Overflows. In: *Ocean Circulation: Mechanisms and Impacts* (eds A. Schmittner, J. C. H. Chiang and S. R. Hemmings), Geophys. Monogr. Ser. **173**, AGU, Washington DC, 75–89.

Roemmich, D., Boebel, O., Desaubies, Y., Freeland, H., Kim, K. and co-authors. 1999. Argo: the global array of profiling floats. In: *Observing the Oceans in the 21st Century* (eds C. J. Koblinsky and N. R. Smith), GODAE Project Office and Bureau of Meteorology, Melbourne, 248–257.

Rossby, T., Prater, M. D. and Søiland, H. 2009. Pathways of inflow and dispersion of warm waters in the Nordic seas. *J. Geophys. Res.* **114**, C04011.

Serra, N., Käse, R. H., Köhl, A., Stammer, D. and Quadfasel, D. 2010. On the low-frequency phase relation between the Denmark Strait and the Faroe-Bank Channel overflows. *Tellus* **62A**.

Smith, W. H. F. and Sandwell, D. T. 1997. Global sea floor topography from satellite altimetry and ship depth soundings. *Science* **277**, 1956–1962.

Søiland, H., Prater, M. D. and Rossby, T. 2008. Rigid topographic control of currents in the Nordic Seas. *Geophys. Res. Lett.* **35**, L18607.

Sutherland, D. A. and Pickart, R. S. 2008. The east Greenland coastal current: structure, variability, and forcing. *Prog. Oceanogr.* **78**, 58–77.

Thomson, R. E. and Freeland, H. J. 2003. Topographic steering of a mid-depth drifter in an eddy-like circulation region south and east of the Hawaiian Ridge. *J. Geophys. Res.* **108**(C11), 3341.

Woodgate, R. A., Fahrbach, E. and Rohardt, G. 1999. Structure and transports of the East Greenland Current at 75°N from moored current meters. *J. Geophys. Res.* **104**(C8), 18059–18072.

2.2 Paper II: Entrainment in the Denmark Strait overflow plume by meso-scale eddies

Ocean Sci., 6, 301–310, 2010
www.ocean-sci.net/6/301/2010/

Ocean Science

Entrainment in the Denmark Strait overflow plume by meso-scale eddies

G. Voet and D. Quadfasel

Institut für Meereskunde, KlimaCampus, University of Hamburg, Hamburg, Germany

Received: 14 October 2009 – Published in Ocean Sci. Discuss.: 11 November 2009
Revised: 16 February 2010 – Accepted: 21 Februay 2010 – Published: 1 March 2010

Abstract. The entrainment of buoyant ambient water into the overflow plume of Denmark Strait and the associated downstream warming of the plume are estimated using time series of currents and temperature from moored instrumentation and classical hydrographic data. Warming rates are highest (0.4–0.5 K/100 km) within the first 200 km of the sill, and decrease to 0.05–0.1 K/100 km further downstream. Stirring by mesoscale eddies causes lateral heat fluxes that explain the 0.1 K/100 km warming, but in the first 200 km from the sill also vertical diapycnal fluxes, probably caused by breaking internal waves, must contribute to the entrainment.

1 Introduction

The Meridional Overturning Circulation in the North Atlantic Ocean is the system of southward flow of cold and dense water at depth and the compensating northward flow of warm and buoyant water at the surface. This circulation is maintained by meridional density gradients in the deep ocean. The transformation of the buoyant surface component to the dense deep component takes place in the Labrador Sea (Schott et al., 2004) and the Nordic Seas (Mauritzen, 1996) where convective processes lead to the production of dense waters that contribute to the North Atlantic Deep Water, the principal component of the lower limb of the Meridional Overturning Circulation. The total amount of North Atlantic Deep Water leaving the subpolar North Atlantic southward is around 18 Sv (1 Sv=10^6 m^3/s) (Stahr and Sanford, 1999).

The deep water formed in the Labrador Sea enters the abyssal North Atlantic without topographic constraints. It contributes 4–6 Sv (Schott et al., 2004) to the North Atlantic Deep Water corresponding to around one third of its total transport. About another 6 Sv are supplied as source waters from the Nordic Seas. These water masses pass the Greenland-Scotland Ridge and enter the abyssal North Atlantic mainly in the two overflows through the Faroe Bank Channel and Denmark Strait. After crossing the sills of the two straits, the dense overflow plumes are subject to strong entrainment of ambient water (Dickson and Brown, 1994). The plume transport is almost doubled by entrainment. Thus, entrainment processes are involved in the formation of North Atlantic Deep Water and contribute about another third or 6 Sv to it (Hansen et al., 2004).

Entrainment in the Denmark Strait overflow plume was apparent early from hydrographic sections, showing that the mean density contrast between plume and ambient water decreased with increasing distance from the sill (Smith, 1976). However, the amount of entrained water could not be quantified until direct current measurements at the sill and different sites downstream became available. First measurements with current meters showed an overflow volume transport of around 3 Sv at the Denmark Strait sill (Worthington, 1969). More recent measurements with moored Acoustic Doppler Current Profilers yield approximately the same transport (Macrander et al., 2005). Current meter measurements downstream of the sill show a transport increase to 5.2 Sv within 300 km distance from the sill (Dickson and Brown, 1994). Different entrainment regimes regarding the strength of entrainment were found along the path of the overflow plume. From velocity and hydrography surveys, entrainment rates were estimated that increased by about one order of magnitude from the sill to 125 km downstream from the sill where the overflow plume enters steeper topography (Girton and Sanford, 2003).

What are the processes that drive the strong entrainment? Both, turbulent mixing and lateral stirring, can lead to the mixing of ambient water into the overflow plume. Mixing through Kelvin-Helmholtz instabilities is induced by strong vertical velocity shear, horizontal velocity shear may lead to

Correspondence to: G. Voet
(gunnar.voet@zmaw.de)

Published by Copernicus Publications on behalf of the European Geosciences Union.

mixing through horizontal instabilities. Meso-scale eddies can induce stirring of different water masses, the strong velocities of the overflow plume may induce Ekman pumping through bottom friction. These processes all have different length scales ranging from below one meter to several kilometers. With the data available at present, only the large scale processes can be resolved from measurements. For a budget of the different entrainment processes, we can calculate the large scale eddy stirring and estimate the Ekman pumping. The effect of small-scale processes like breaking internal waves can then be estimated as the residuum in the budget.

Current measurements and temperature records of the Denmark Strait overflow plume show a high variability on timescales of 2–5 days close to the sill (Ross, 1984) and 1–12 days about 500 km downstream (Dickson and Brown, 1994). Pulses of strong current velocity are accompanied by an increase in overflow plume height. These domes of cold water are in rotation and connected to surface eddies observed in satellite infrared imagery (Bruce, 1995; Krauss, 1996) and satellite altimetry (Høyer and Quadfasel, 2001). The meso-scale eddies reach throughout the whole water column. They have a diameter of 20–40 km and travel with the velocity of the overflow plume. Similar eddies have been observed with moorings in the overflow plume downstream of the Faroe Bank Channel overflow (Geyer et al., 2006). The breakup of an overflow plume into barotropic eddies was also simulated in laboratory experiments with dense currents on a sloping bottom in rotating tanks (Whitehead et al., 1990; Cenedese et al., 2003). Generation mechanisms for the observed eddies were investigated in numerical studies. A steady streamtube model resembling the overflow showed baroclinic instabilities at a period of 2.1 days and a wavelength of 80 km, comparing well with dominant periods in mooring records (Smith, 1976). The partly barotropic outflow through Denmark Strait and the subsequent descent of the dense bottom current makes vortex stretching another possible eddy generation mechanism (Spall and Price, 1998). More complex 3-D models with realistic bottom topography explain the eddy formation with a combination of both baroclinic instability and vortex stretching (Jiang and Garwood, 1996; Krauss and Käse, 1998; Jungclaus et al., 2001).

As it almost doubles the overflow plume transport, entrainment strongly influences the formation rate of North Atlantic Deep Water. Furthermore, it modifies the final characteristics of the North Atlantic Deep Water as less dense ambient water is mixed into the overflow plume. We therefore regard entrainment as an important element of the Meridional Overturning Circulation. While the amount of entrained water into the Denmark Strait overflow plume is relatively well known, the relative contributions of horizontal and vertical turbulent processes to the entrainment are not quantified yet. This study is dedicated to the question of the importance of the horizontal turbulence associated with meso-scale eddies for the entrainment into the Denmark Strait overflow plume.

After giving an overview of the observational data used in this study in Sect. 2, we provide a theoretical basis for the calculation of eddy driven entrainment with a statistical approach in Sect. 3. We present overflow plume characteristics from time averaged quantitites and establish a mean plume warming rate along the plume pathway in Sect. 4. A warming rate from eddy driven heat fluxes is calculated in Sect. 5. Conclusions are drawn in Sect. 6.

2 Data

Mooring arrays were set across the pathway of the Denmark Strait overflow plume at four different locations over the past twenty years (Fig. 1). The array located at the Denmark Strait sill consists of bottom mounted ADCPs with the first deployment in 1999 and sustained redeployments thereafter until present (Macrander et al., 2005; Quadfasel and Käse, 2007). Arrays A and B at 200 and 360 km distance from the sill were deployed in 1990 for periods of three months and one year, respectively (Dickson and Brown, 1994). Mooring array C at 520 km distance downstream of the sill was deployed repeatedly from 1986 to 1990 (Dickson and Brown, 1994) and again from 1995 until present (Dickson et al., 2008) in one year periods. In this study we use array C data from the deployment period 2001/2002 as this provides the best spatial coverage of the overflow plume together with minimum instrument failure. All moorings at arrays A, B and C were equipped with two to four Aanderaa Rotor Current Meters measuring speed and direction of the current. In addition temperature sensors were attached to all instruments.

The coordinate system for each mooring is rotated to be aligned with the mean flow, thus each mooring is allocated its own coordinate system. The angle of rotation is given by the mean direction measured at the instrument just above the bottom Ekman layer. In these new coordinate systems, the v-component of the current points toward the mean flow direction (SW–W) while the u-component points perpendicular to the right (upslope), as in a regular right-handed coordinate system. Figure 2 shows an illustration of the rotated coordinate system together with an example for the time series recorded by an instrument at the central mooring at array C.

Hydrographic data from the overflow region is used in addition to the mooring data (Fig. 1). Six standard sections normal to the slope, of which four coincide with the location of the mooring arrays, were served annually since 1997 (Dickson et al., 2007). The hydrographic data complements the high temporal resolution mooring time series with snapshots of high spatial resolution.

3 Heat fluxes and entrainment

The entrainment of buoyant ambient water into the dense overflow plume decreases the overall density of the plume while it increases the transported volume. The mooring time

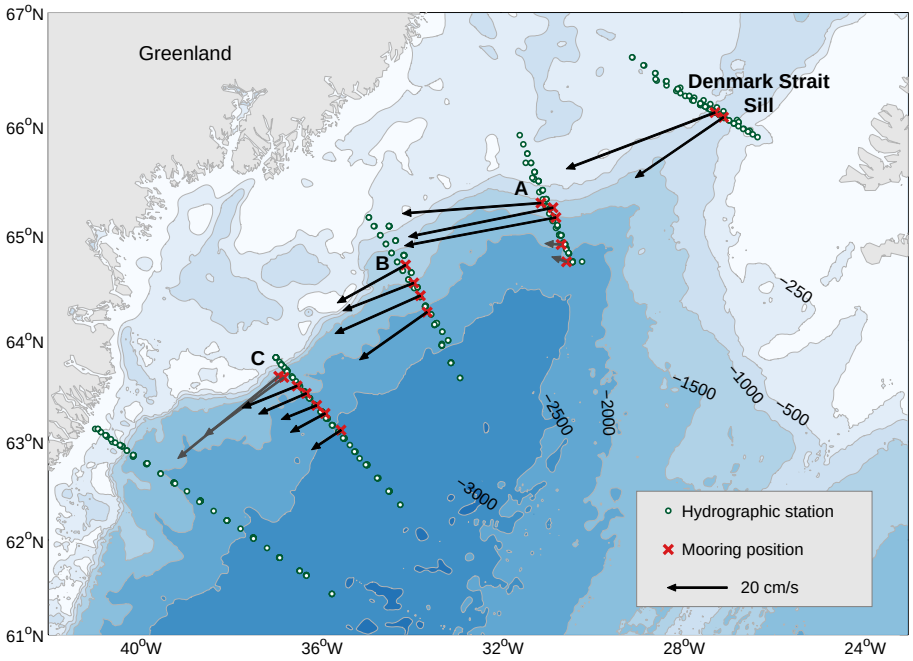

Fig. 1. Map showing the bathymetry of the Denmark Strait and the area south of it. Green circles mark the positions of hydrographic stations. One hydrographic section further south off Cape Farewell is not shown on the map. Red crosses mark the mooring positions. Mean velocities from the instruments (array A to C) or bins (sill array) just above the bottom Ekman layer are shown with the black vectors. Mean velocities from instruments that were not situated in the overflow plume are shown with grey vectors.

series only partially include density data. Instead of density fluxes we use the heat flux into the overflow plume as a proxy for the entrainment rate. This is justified with salinity values varying by only about 0.05 between the overflow plume and the ambient water (see e.g. the salinity section in Rudels et al., 1999), making density dependent on temperature only in a first approximation.

With heat defined as the product of density times specific heat times temperature, $Q = \rho c_p T$, heat fluxes per unit area in a turbulent flow are given by the heat transport equation:

$$\underbrace{\frac{\partial \overline{Q}}{\partial t}}_{\text{Local change}} \underbrace{+\overline{u}\frac{\partial \overline{Q}}{\partial x}+\overline{v}\frac{\partial \overline{Q}}{\partial y}+\overline{w}\frac{\partial \overline{Q}}{\partial z}}_{\text{Advective terms}} = \underbrace{\frac{\partial}{\partial x}\overline{u'Q'}+\frac{\partial}{\partial y}\overline{v'Q'}+\frac{\partial}{\partial z}\overline{w'Q'}}_{\text{Turbulent terms}} \quad (1)$$

Here, $\overline{Q}$ and $(\overline{u},\overline{v},\overline{w})$ are the mean heat and the mean velocity components of the flow while Q' and (u',v',w') are the fluctuations of these. Integrating this equation over a closed volume gives the change of heat within that volume.

The mooring data only provides measurements of temperature and velocity at certain points. The integration over closed plume surfaces will be done later and in the following discussion we will simply use the temperature transport equation per unit area:

$$\underbrace{\frac{\partial \overline{T}}{\partial t}}_{\text{Local change}} \underbrace{+\overline{u}\frac{\partial \overline{T}}{\partial x}+\overline{v}\frac{\partial \overline{T}}{\partial y}+\overline{w}\frac{\partial \overline{T}}{\partial z}}_{\text{Advective terms}} = \underbrace{\frac{\partial}{\partial x}\overline{u'T'}+\frac{\partial}{\partial y}\overline{v'T'}+\frac{\partial}{\partial z}\overline{w'T'}}_{\text{Turbulent terms}} \quad (2)$$

Geometry and dynamics of the overflow plume allow a simplification of the temperature transport equation. We consider the overflow to be stationary in zeroth approximation. This eliminates the time derivative of the mean temperature. Since the coordinate system is aligned with the mean flow direction, the mean velocity normal to the mean flow, $\overline{u}$, is zero by definition. We compare the order of magnitude of the remaining two advective terms against each other as follows. A vertical mean velocity $\overline{w}$ may arise from a divergent Ekman transport at the bottom. The magnitude of $\overline{w}$ can be estimated from the mean downstream velocity $\overline{v}$ as it determines the Ekman transport T_E,

$$T_\mathrm{E} = \frac{c_\mathrm{D}\overline{v}^2}{f}, \quad (3)$$

with the bottom drag coefficient $c_\mathrm{D} = 10^{-3}$ (Käse et al., 2003) and the Coriolis parameter f. Division of T_E by the

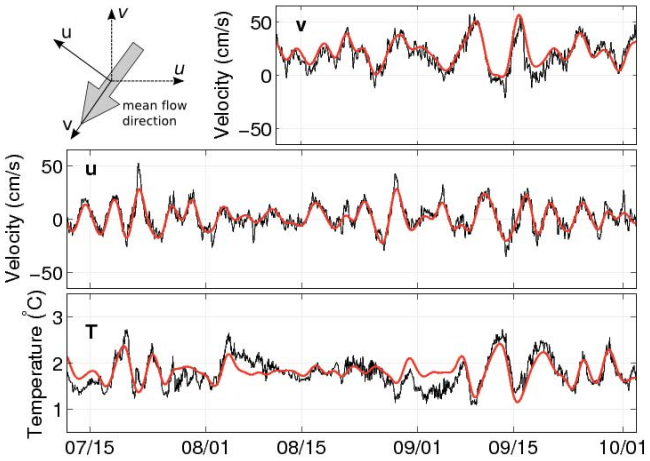

Fig. 2. Time series of temperature (lower panel), velocity perpendicular to the mean flow (middle panel) and along the mean flow direction of the overflow plume (upper panel). The time series were recorded at the central mooring at array C at a height of 102 m above the bottom. Shown here is only a part of the complete time series that has a length of one year. Black curves give the full spectrum of the data at a resolution of one hour. Red curves show bandpass filtered time series with an added mean value to make them comparable to the original data. The inset to the upper left illustrates the rotation of the original coordinate system with east and north components (dashed arrows) to a coordinate system aligned with the mean flow (full arrows) as used for u and v shown here.

Ekman layer depth d_E yields an estimate of the mean Ekman velocity $\overline{u_E}$. The Ekman velocity has its maximum at the plume core where the highest mean velocities $\overline{v}$ are reached. It decreases to the sides of the overflow plume. By making the assumption of zero Ekman velocities outside the plume $u_E(\text{edge}) = 0$, the divergence can be estimated:

$$\frac{\partial u_E}{\partial x} = \frac{u_E(\text{core}) - u_E(\text{edge})}{x(\text{core}) - x(\text{edge})} \tag{4}$$

This divergence must be balanced by a vertical velocity $\overline{w}$. It can be calculated from the equation of continuity:

$$\frac{\partial w}{\partial z} + \frac{\partial u}{\partial x} = 0 \Rightarrow w = \frac{\Delta u}{\Delta x}\Delta z \tag{5}$$

A mean downstream velocity $\overline{v} = 0.2$ m/s leads to a mean Ekman velocity of $\overline{u_E} = 0.02$ m/s. The resulting vertical velocity is $\overline{w} = 4 \times 10^{-5}$ m/s. The temperature gradients dT/dz and dT/dy can be estimated from temperature measurements in the overflow plume and the ambient water. These show a temperature difference of about 5 K over a distance of 1000 m that lead to a gradient of $dT/dz = 5 \times 10^{-3}$ K/m. The mean plume temperature in the y-direction changes by about 1.5 K over a distance of 500 km as will be shown in the next section. This leads to a temperature gradient of $dT/dy = 3 \times 10^{-6}$ K/m. With these values, the magnitude of the two remaining advective terms in the temperature transport equation is

$$\overline{w}\frac{\partial T}{\partial z} \cong 2 \times 10^{-7} \qquad \overline{v}\frac{\partial T}{\partial y} \cong 1 \times 10^{-6}. \tag{6}$$

Hence, the horizontal advective term is approximately one order of magnitude larger than the vertical advective term[1]. This indicates that the vertical advective temperature flux may be small enough to be neglected in the analysis. Variations of the drag coefficient and local fluctuations of mean velocity and vertical temperature gradient can, however, lead to considerable variations in the size of the advective terms.

The two horizontal turbulent terms can be compared to each other. The divergence of turbulent motion in the x-direction is very strong. There is a transition from (nearly) zero turbulent motion outside the plume to vigorous turbulent motion in the plume centre over a distance of less than 50 km. The eddies travel with the overflow plume in the y-direction, leading to only little changes in turbulent motion along the y-direction. We thus also neglect the term with v'.

The remaining terms show that the warming of the plume along its path is driven by turbulent temperature exchanges in the x- and z-direction and a possible contribution of neglected terms included here as ϵ:

$$\overline{v}\frac{\partial \overline{T}}{\partial y} = \frac{\partial}{\partial x}\overline{u'T'} + \frac{\partial}{\partial z}\overline{w'T'} + \epsilon. \tag{7}$$

With our data we can calculate the warming rate along y and horizontal turbulent temperature fluxes along x.

4 Structure of the overflow plume and its downstream warming

After crossing the Denmark Strait sill, the overflow plume accelerates on the first 125 km until it reaches its maximum mean velocity of about 65 cm/s (Girton and Sanford, 2003). Thereafter the mean velocity decreases to about 45 cm/s at mooring array A, 25 cm/s at array B and 20 cm/s at array C (Fig. 1). At all three arrays the flow has a baroclinic structure with highest velocities close to the bottom.

The eddy kinetic energy K_E of the flow is defined as

$$K_E = \frac{1}{2}(\overline{u'^2} + \overline{v'^2}) \tag{8}$$

where u' and v' denote the fluctuations of the mean flow. As we are interested in the energy of the meso-scale eddies, we exclude not only the mean of the time series but also variability deriving from processes other than eddies, e.g. internal waves or tides. The tidal signal is estimated by means of

[1]The estimate for $\overline{w}$ calculated here gives an upper limit. An opposite Ekman transport at the upper boundary of the plume and non-zero Ekman transports at the plume edges lead to a reduction of the estimate.

harmonical analysis (software provided by Pawlowicz et al., 2002) and substracted from the time series. This removes only about 5% of the overall velocity variance as the tides are weak in this area.

Using a bandpass filter we remove the remaining variability on long and short timescales while the signal in the frequency domain of the meso-scale eddies is kept. Figure 3 shows spectra of velocity time series recorded by the moorings. The time scale of the eddies grows with increasing distance from the sill and we therefore use different filter parameters for each mooring array to account for this increase: cut-off periods for the bandpass filter chosen are 28 h to 200 h at mooring array A, 36 h to 200 h at array B and 60 h to 300 h at array C. Thus, about 3–4 eddies are covered within the bandwidth.

We use the bandpass filtered time series u' and v' to calculate mean eddy kinetic energies. The highest eddy kinetic energies are found in the region of the plume core (Fig. 4), defined here as the part of the plume where the highest downstream velocities are reached. In contrast to the mean velocities that have their maximum close to the bottom, the mean eddy kinetic energy is highest at the top of the overflow plume at all mooring arrays. It decreases from around 200 cm^2/s^2 at arrays A and B to around 100 cm^2/s^2 at array C.

The overflow plume is generally defined as water with a density anomaly higher than 27.8 kg/m^3 (Dickson and Brown, 1994) corresponding to temperatures below 2–3 °C. For a separation of the overflow water and the overlying water masses at each array we use the temperature time series available from all moorings. The temperatures vary on approximately the same time scale as the plume velocities, reflecting the variability in plume height. When domes of cold overflow water pass a mooring the height of the plume boundary can change by several hundred meters. This makes the temperature data from the moorings, despite their low spatial resolution, a better choice for the determination of the upper limiting isotherm than data from hydrographic surveys that only consist of single snapshots once a year.

From the temperature time series and the hydrographic data set we calculate mean plume temperatures at several sites downstream of the sill. These mean temperatures provide an estimate for the mean plume warming rate with respect to the distance from the sill. One way to find the temperature change along the plume pathway is to calculate the mean temperature over the whole cross-sectional area below the limiting upper isotherm. This can be done for each hydrographic section and for the mooring arrays A, B and C. The mooring array at the sill only has bottom temperature time series that do not allow this calculation. A second way to determine a mean plume temperature is to calculate the mean bottom temperatures of the plume at each mooring array. This can also be done with the mooring array at the sill. The core of the plume is here defined as the three time series with the lowest mean temperatures from each array. The mean temperature for each mooring array is then calculated as the mean of these three values.

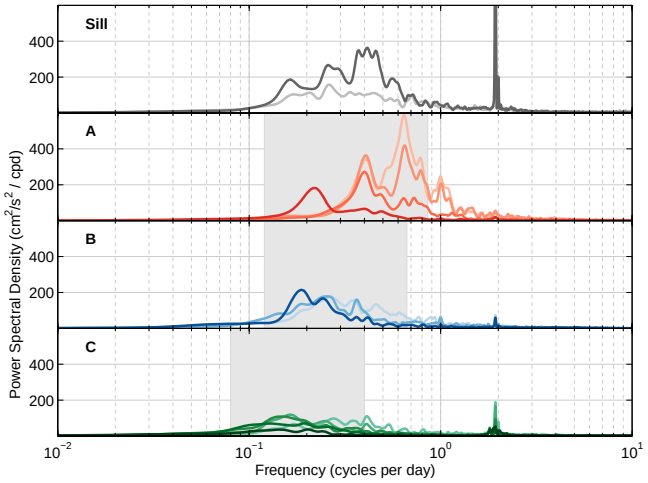

Fig. 3. Power spectral density calculated from velocity time series at each mooring and array. The velocity component perpendicular to the mean flow direction was used. Colours from light to dark correspond to mooring depth at the shelf from shallow to deep. The grey shaded areas for arrays A to C show the frequency domain that is used for the bandpass filtering.

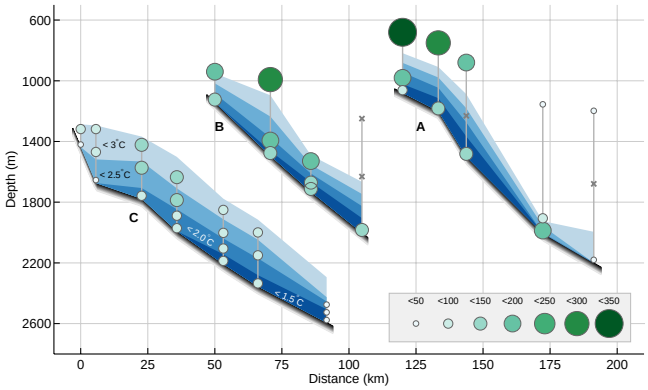

Fig. 4. Mean eddy kinetic energies (cm^2/s^2) at mooring arrays A to C. The green circles show the size of the eddy kinetic energy at each current meter. The eddy kinetic energies were calculated from the bandpass filtered velocity time series. The blue shaded area shows the mean temperature structure of the overflow plume as calculated from the temperature time series at each instrument.

The mean plume temperatures calculated in both ways are shown in Fig. 5. Both the mean bottom temperatures and the vertically averaged temperatures increase by about 1 K on the first 200 km. Farther away from the sill the warming is smaller with less than 0.1 K per 100 km for the vertical averaging method and about 0.1 K per 100 km for the bottom temperature method.

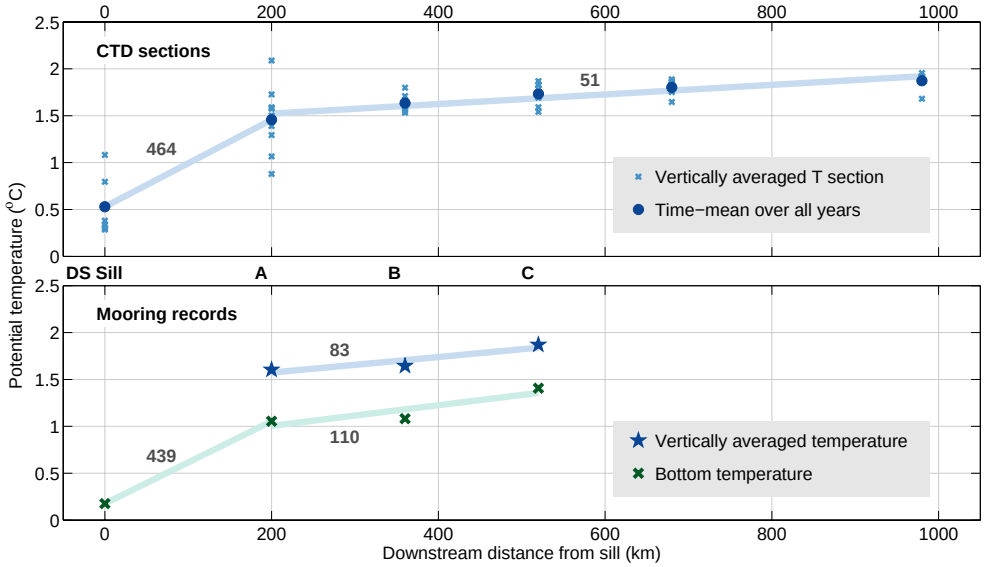

Fig. 5. Mean plume temperatures downstream of the Denmark Strait sill. The upper panel shows mean plume temperatures calculated from hydrographic sections occupied between 1997 and 2008. For each section and each year, the mean plume temperature for the cross-sectional area below the 2.5° isotherm was calculated (blue crosses). Blue dots show the mean plume temperature at each section as a time mean over the individual years. As the measurements show two different warming regimes, temperature gradients were calculated with linear fits for the distance from the sill to the first section downstream and from thereon to a section about 1000 km downstream of the Denmark Strait sill. Lines show the linear fits to the mean plume temperatures, the numbers give the temperature gradients in mK per 100 km. The lower panel shows mean plume temperatures as measured by the mooring instruments. The vertically averaged temperature was calculated as for the hydrographic sections. The bottom temperature was calculated by taking the mean over the three coldest bottom-near time series at each array. Temperature gradients are shown as in the upper panel.

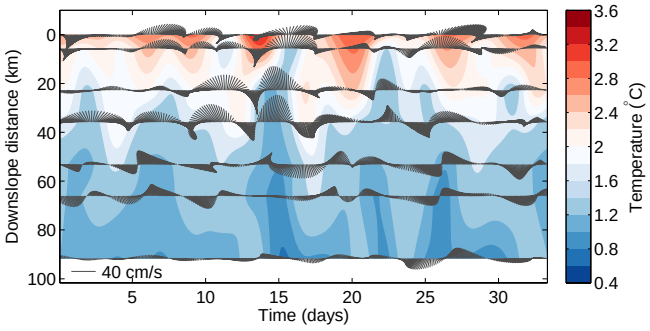

Fig. 6. Hovmoeller diagram of bottom temperatures (within 50 m of the bottom) at array C showing bandpass filtered data. Overlayn are stick plots of bandpass filtered velocity time series recorded at the same locations. A reference velocity for the stick plots is shown to the lower left.

5 Eddy heat transports

The overflow plume has high eddy kinetic energies on the time scale given by the meso-scale eddies. We now estimate the contribution of eddy stirring to the warming of the overflow plume, i.e. its contribution to the entrainment. An estimate for eddy driven heat transports into the overflow plume is first illustrated with data from mooring array C. This dataset is more comprehensive than the two other arrays from which the results will be presented thereafter.

5.1 Eddy heat transports at array C

The rotational motion of the eddies does not lead to a net water mass transport since the time mean of the current fluctuation $\overline{u'}$ is zero by definition. However, a net temperature flux $\overline{u'T'}$ can take place by the transport of warm and cold water in opposite directions. The variation of $\overline{u'T'}$ across the plume corresponds to the horizontal turbulent term in the temperature transport (Eq. 2). We focus again on the meso-scale eddies by using the bandpass filtered time series u' and T'. Figure 6 illustrates the correlation between u' and T'. The stick plot shows the rotational motion of the overflow plume and its relation with temperature fluctuations. The fluctuations of the current on the eddy time scale lead to a redistribution of warm and cold water.

Figure 7 shows the mean eddy temperature fluxes at array C. The region of highest eddy temperature flux corresponds to the region of highest eddy kinetic energy. The direction of $\overline{u'T'}$ has a similar pattern for all moorings in the array. The eddy temperature flux is directed downslope at the

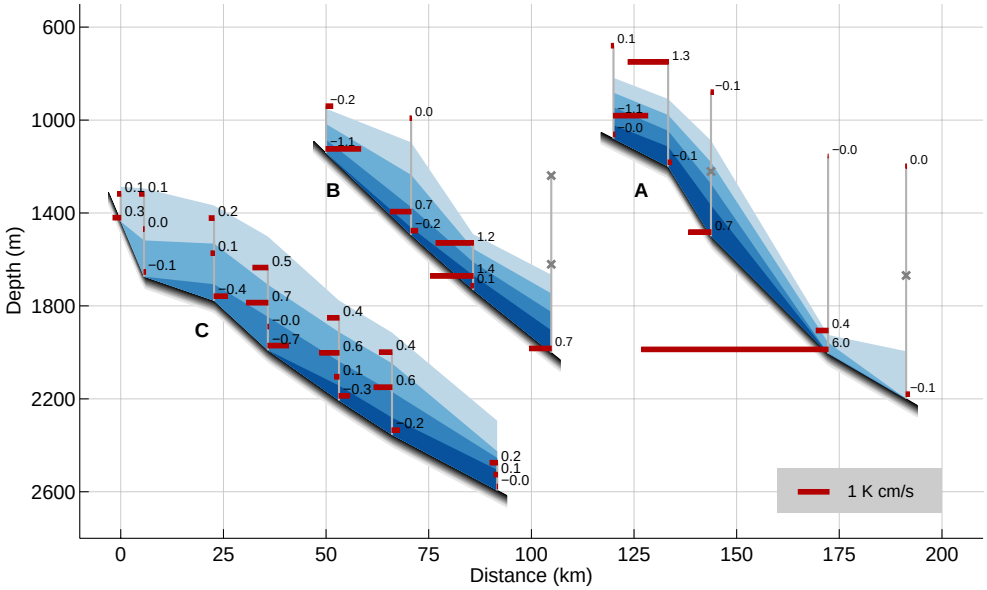

Fig. 7. Mean eddy temperature fluxes $\overline{u'T'}$ (K cm/s) at arrays A to C. The red bars give the direction and magnitude of the mean eddy temperature flux. A scale for the red bars is given to the lower right. Numbers next to the red bars give the exact magnitude of the mean eddy temperature flux. Grey crosses mark instruments where no mean eddy temperature flux could be calculated. The temperature structure of the plume is shown as in Fig. 4.

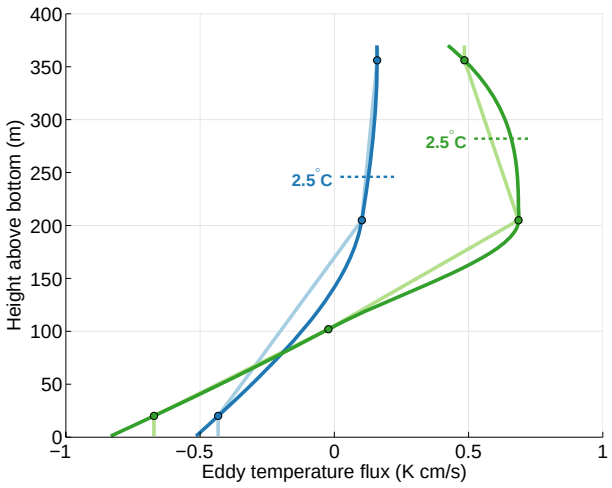

Fig. 8. Example for the interpolation of mean eddy temperature fluxes with height with data from two moorings at array C. Dots show mean eddy temperature fluxes as calulated at the height of the current meters. Lines in light color show the vertical interpolation of the mean eddy temperature flux with a linear method. Dark lines show vertical interpolation with polynomials. The dashed lines give the mean 2.5 °C isotherm at the location of the mooring that serves as upper integration boundary for the results in Fig. 9.

bottom and reverses with increasing height above seabed. In both cases, the temperature flux is opposite to the temperature gradient. Thus, not surprisingly, heat is transported from warm into cold regions. The magnitude of $\overline{u'T'}$ between 0.1 and 1 K cm/s is up to an order of magnitude smaller than the products of the standard deviations of u and T that have a magnitude of about 4 K cm/s. The product of the standard deviations may be regarded as the maximum possible temperature transport due to fluctuations of velocity and temperature. Its difference to the mean eddy temperature flux calculated here is partly due to variability outside the bandwith of the bandpass filter. Furthermore, the correlation between velocity and temperature fluctuation does not always have the same phase. Figure 6 shows positive and negative correlation of current and temperature fluctuations.

Interpolation, subsequent vertical integration of the eddy temperature fluxes from the bottom to the limiting upper isotherm and multiplication by specific heat and density gives the net eddy heat transport at a mooring line. Usually there are two to four instruments at each mooring over a vertical distance of about 300 m. Two different methods are used for the vertical interpolation between the instruments. In the first method, the profiles are interpolated linearly between the data points and taken constant elsewhere. In the second method, polynomials are used for data inter- and extrapolation. Figure 8 shows a examples for the two interpolation methods.

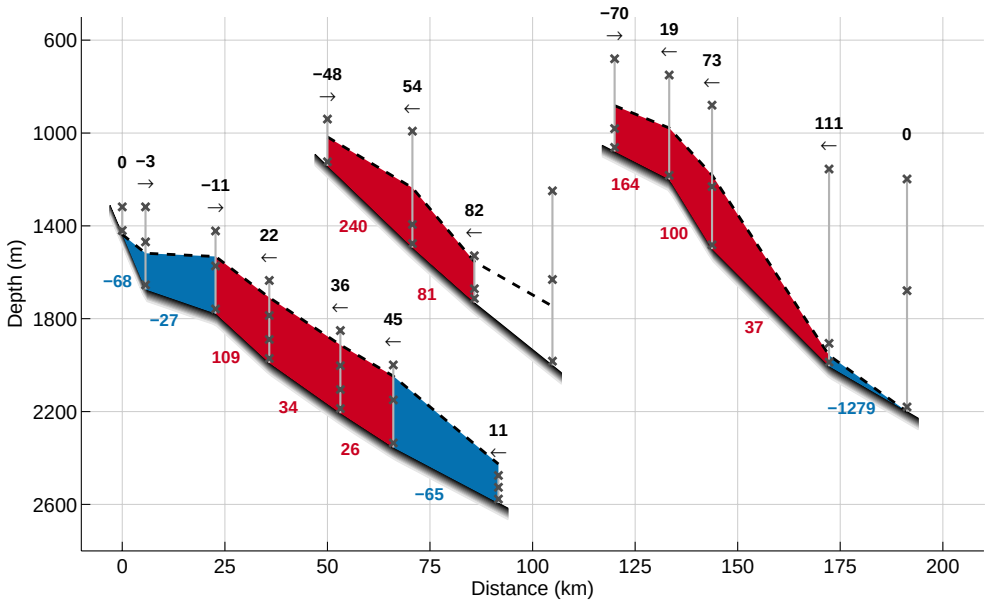

Fig. 9. Net eddy heat transports (10^5 J/ms) at the mooring lines are shown with numbers and arrows above each mooring. The net eddy heat transport was calculated by interpolating and integrating the mean eddy temperature fluxes up to the limiting 2.5 °C isotherm that is shown by the dashed black line. Red and blue colours show convergences and divergences of the net eddy heat transport in each box. Numbers below each box give the net warming rate (mK/100km) for each box.

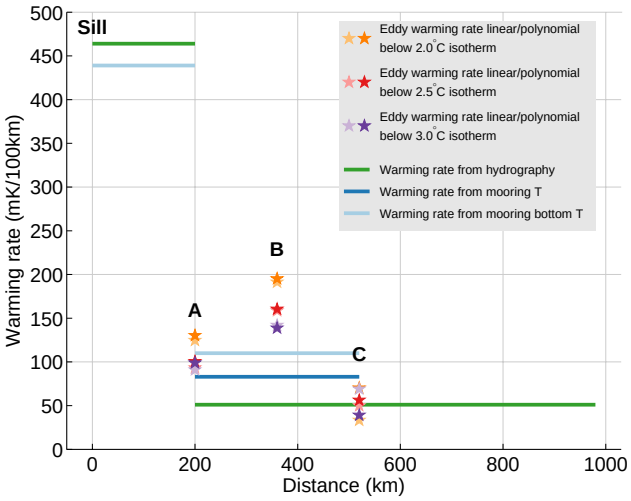

Fig. 10. Comparison of plume warming rates derived from direct temperature measurements as calculated in Fig. 5 (lines) and eddy driven warming rates of the plume core (stars). The different warming rates from direct temperature measurements stem from different calculation methods as explained in Sect. 4. Results from two different interpolation methods and three different upper limiting isotherms are shown for the eddy driven warming rates.

We use the 2.0 °C, 2.5 °C and 3.0 °C isotherms as upper integration boundaries. Together with the two vertical interpolation methods for the eddy temperature fluxes this results in six different realizations for the following calculation of net eddy heat transports.

Each pair of moorings forms a box together with the limiting upper isotherm. The net eddy heat transport into these boxes is the sum of the eddy heat transports through both sides. Figure 9 shows the vertically integrated eddy heat fluxes and the net eddy heat transport into the boxes for the 2.5 °C case. The eddy heat fluxes lead to a net warming in the centre of the plume. The region of the plume edges is cooled by the eddy heat transports. The position of the convergent region of eddy heat transport varies with the different plume boundary definitions. The region is situated downslope for the 2.0 °C-plume while it is more pronounced upslope for the 3.0 °C-plume.

By making the assumption that the eddy heat transport observed at the array C is regionally a steady process, we are able to calculate a warming rate per downstream distance. The time period for which the plume is exposed to the eddy mixing process is calculated from the mean plume velocity. We use a mean velocity of 20 cm/s at array C. This is less than the mean bottom velocity of about 25 cm/s as it gives a vertical averaged value of the whole plume. The highest warming rate for a single box is 100 mK per 100 km. The mean value for the convergent part of the plume, i.e. the part of the plume that gains heat through eddy heat transports,

is 54 mK per 100 km. The warming rates derived from the two other boundary definitions are of the same order of size, with 72 mK per 100 km for the 2.0 °C-plume area and 45 mK per 100 km for the 3.0 °C-plume area. A comparison of the results from linear and polynomial interpolation gives an estimate for the uncertainty of the calculations. The warming rates for the whole convergent plume area differ by 11% with the 2.5 and 3.0 °C-boundary and by 43% with the 2.0 °C-boundary.

5.2 Eddy heat transports at arrays A and B

The eddy heat fluxes at the two upstream arrays A and B are calulated in the same way as for array C. Only the parameters for the bandpass filters are different, as described above.

The eddy temperature fluxes at the two arrays are shown in Fig. 7. The eddy temperature fluxes at the bottom converge in the centre of the plume at both arrays. This indicates that the whole plume core is covered by the mooring arrays. The magnitude of the eddy temperature fluxes is roughly the same at both arrays and approximately twice as high as at array C. Only the eddy temperature flux at the bottom instrument of mooring four at array A is five times larger than all other eddy temperature fluxes calculated here. This is the point where the isotherms indicate the location of the plume edge. It appears to be a region of strong mixing, possibly because of the strongly inclined isotherms. Diapycnal mixing induced by horizontal eddy motion may take place here.

Net eddy heat transports into the overflow plume, limited again by the 2.5 °C isotherm, are shown in Fig. 9. The highest convergence in eddy heat transport is found at the upper part of the slope at both arrays. At the lower edge of the plume at array A strong cooling is observed. This results from the high eddy heat flux in combination with the small volume of the box. The data from array B was not sufficient for a calculation of the eddy heat transport at the lower part of the slope.

At both arrays the magnitude of the convergences in heat transports is approximately three times higher than at array C. The highest value is found upslope at both arrays. However, lowering the upper plume boundary to 2.0 °C does not shift the convergent region downslope as it was the case at array C. At array A, the region of convergent eddy heat transport for the 2.0 °C-plume is even shifted upslope as only the upper two boxes show a net warming. This indicates that the plume core has not migrated downhill yet.

To calculate plume warming rates from the eddy heat transports, the mean plume velocity is again used to estimate the time that the eddy mixing process can act on the plume. The mean plume velocity is 45 cm/s at array A while at array B the plume has slowed down to 25 cm/s (Fig. 1). These values are chosen to represent the mean velocity up to the plume boundary. Compared to array C the plume velocities are still high. They lead to shorter time periods that the eddy mixing is effective than farther downstream. We find high eddy induced plume warming rates of up to 200 mK/100 km at the upper part of the slope at both arrays. The overall warming rates per 100 km for the parts of the plume that have a convergent eddy heat transport are shown in Fig. 10. They are about 120 mK/100 km at array A and about 160 mK/100 km at array B. While the eddy heat transports are approximately the same at the two upstream arrays, the smaller mean plume velocity at array B leads to the higher eddy induced warming rates. Results from the two interpolation methods differ by 10% at both arrays.

6 Conclusions

A comparison of the overall plume warming rates with the eddy driven plume warming rate shows the relative importance of horizontal and vertical turbulent processes for the entrainment. Figure 10 compares the eddy driven warming rates calculated at the three mooring arrays A to C with the warming rates derived from the downstream development of the mean plume temperatures. From array A to array C, the eddy heat transports do explain the warming of the plume and the meso-scale eddies are thus the driving mechanism for the temperature increase in the region farther than 200 km from the sill. Unfortunately, no eddy driven warming rates between the sill and array A could be calculated in this study. However, it is questionable whether eddies alone lead to a warming rate that is three to four times larger on the first 200 km behind the sill than in the mooring arrays analysed here. Thus, on the first 200 km after the sill vertical processes should play an important role in the mixing.

From the results presented here, together with the findings from other studies (Girton, 2001; Girton and Sanford, 2003; Käse et al., 2003), a picture of three different entrainment regimes in the Denmark Strait overflow plume emerges.

The first regime is located between the Denmark Strait sill and ∼125 km downstream of the sill. Here the plume accelerates from a mean speed of about 40 cm/s at the sill to its maximum speed of 60 cm/s. The current has a barotropic structure close to the sill, i.e. there is no strong shear between the overflow plume and the watermasses above. Thus, little vertical turbulence should occur. Rudels et al. (1999) observed a capping of the overflow plume with low salinity water that survived the initial descent of the plume. This suggests that vertical mixing is weak during the initial descent as the capping would be disturbed by the mixing. The overall entrainment is estimated to be one order of magnitude smaller than beyond 125 km from the sill (Girton and Sanford, 2003). High variability in the bottom current with a dominant time-scale of 1.8 days suggests that eddies are generated in the overflow through baroclinic instability (Smith, 1976).

The region of strong entrainment into the overflow plume characterises the second regime. It reaches approximately to array A 200 km downstream of the sill as indicated by the

high plume warming rate. The high plume velocities and the transition to a baroclinic flow lead to large vertical velocity shears. This shear and low Richardson numbers indicate vertical instability.

The third regime beyond 200 km downstream distance is characterized by the dominance of eddies in the entrainment process. The vertical velocity shear provides the energy to feed baroclinic instabilities. The enhancement of the eddy field already starts at ∼125 km, but the eddy mixing becomes the dominant process for the entrainment into the overflow plume here. As the mean plume speed decreases, the velocity shear also decreases and the effect of vertical turbulence diminishes.

Acknowledgements. The financial support for this study by Deutsche Forschungsgemeinschaft (SFB 512 E2), the European Commission (VEINS, ASOF, THOR) and the German Ministry of Education and Research (Nordatlantik Projekt) is gratefully acknowledged. Thanks to Andreas Macrander for providing hydrographic data from the Denmark Strait sill.

Edited by: K. J. Heywood

References

Bruce, J. G.: Eddies southwest of the Denmark Strait, Deep-Sea Res. Pt. I, 42, 13–29, 1995.

Cenedese, C., Whitehead, J. A., Ascarelli, T. A., and Ohiwa, M.: A Dense Current Flowing down a Sloping Bottom in a Rotating Fluid, J. Phys. Oceanogr., 34, 188–203, 2003.

Dickson, B., Dye, S., Jónsson, S., Köhl, A., Macrander, A., Marnela, M., Meincke, J., Olsen, S., Rudels, B., Valdimarsson, H., and Voet, G.: Arctic-Subarctic Ocean Fluxes, chap. The Overflow Flux West of Iceland: Variability, Origins and Forcing, pp. 443–474, Springer, 2008.

Dickson, R., Rudels, B., Dye, S., Karcher, M., Meincke, J., and Yashayaev, I.: Current estimates of freshwater flux through Arctic and subarctic seas, Prog. Oceanogr., 73, 210–230, 2007.

Dickson, R. R. and Brown, J.: The production of North Atlantic Deep Water: Sources, rates, and pathways, J. Geophys. Res., 99, 12319–12341, 1994.

Geyer, F., Østerhus, S., Hansen, B., and Quadfasel, D.: Observations of highly regular oscillations in the overflow plume downstream of the Faroe Bank Channel, J. Geophys. Res., 111, C12020, doi:10.1029/2006JC003693, 2006.

Girton, J. B.: Dynamics of transport and variability in the Denmark Strait overflow, Ph.D. thesis, University of Washington, Seattle, WA, 2001.

Girton, J. B. and Sanford, T. B.: Descent and Modification of the Overflow Plume in the Denmark Strait, J. Phys. Oceanogr., 33, 1351–1364, 2003.

Hansen, B., Østerhus, S., Quadfasel, D., and Turrell, W.: Already the Day After Tomorrow?, Science, 305, 953–954, 2004.

Høyer, J. L. and Quadfasel, D.: Detection of deep overflows with satellite altimetry, Geophys. Res. Lett., 28, 1611–1614, 2001.

Jiang, L. and Garwood, R. W.: Three-Dimensional Simulations of Overflows on Continental Slopes, J. Phys. Oceanogr., 26, 1214–1233, 1996.

Jungclaus, J. H., Hauser, J., and Käse, R. H.: Cyclogenesis in the Denmark Strait Overflow Plume, J. Phys. Oceanogr., 31, 3214–3229, 2001.

Käse, R. H., Girton, J. B., and Sanford, T. B.: Structure and variability of the Denmark Strait Overflow: Model and observations, J. Geophys. Res., 108, C6, 3181, 2003.

Krauss, W.: A note on overflow eddies, Deep-Sea Res. Pt. I, 43, 1661–1667, 1996.

Krauss, W. and Käse, R. H.: Eddy formation in the Denmark Strait overflow, J. Geophys. Res., 103, 15525–15538, 1998.

Macrander, A., Send, U., Valdimarsson, H., Jónsson, S., and Käse, R. H.: Interannual changes in the overflow core from the Nordic Seas into the Atlantic Ocean through Denmark Strait, Geophys. Res. Lett., 32, L06606, doi:10.1029/2004GL021463, 2005.

Mauritzen, C.: Production of dense overflow waters feeding the North Atlantic across the Greenland-Scotland Ridge. Part 1: Evidence for a revised circulation scheme, Deep-Sea Res. Pt. I, 43, 769–806, 1996.

Pawlowicz, R., Beardsley, B., and Lentz, S.: Classical tidal harmonic analysis including error estimates in MATLAB using T_TIDE, Comput. Geosci., 28, 929–937, 2002.

Quadfasel, D. and Käse, R. H.: Ocean Circulation: Mechanisms and Impacts, vol. 173, chap. Present-Day Manifestation of the Nordic Seas Overflows, pp. 75–89, Geophys. Monogr. Ser., AGU, Washington D.C., 2007.

Ross, C. K.: Temperature – salinity characteristics of the "overflow" water in Denmark Strait during "OVERFLOW '73", Rap. Proces., 185, 111–119, 1984.

Rudels, B., Eriksson, P., Grönvall, H., Hietala, R., and Launiainen, J.: Hydrographic Observations in Denmark Strait in Fall 1997, and their Implications for the Entrainment into the Overflow Plume, Geophys. Res. Lett., 26, 1325–1328, 1999.

Schott, F. A., Zantopp, R., Stramma, L., Dengler, M., Fischer, J., and Wibaux, M.: Circulation and deep-water export at the western exit of the subpolar North Atlantic, J. Phys. Oceanogr., 34, 817–843, 2004.

Smith, P. C.: Baroclinic Instability in the Denmark Strait Overflow, J. Phys. Oceanogr., 6, 355–371, 1976.

Spall, M. A. and Price, J. F.: Mesoscale Variability in Denmark Strait: The PV Outflow Hypothesis, J. Phys. Oceanogr., 28, 1598–1623, 1998.

Stahr, F. R. and Sanford, T. B.: Transport and bottom boundary layer observations of the North Atlantic Deep Western Boundary Current at the Blake Outer Ridge, Deep-Sea Res. Pt. II, 46, 205–243, 1999.

Whitehead, J. A., Stern, M. E., Flierl, G. R., and Klinger, B. A.: Experimental Observations of Baroclinic Eddies on a Sloping Bottom, J. Geophys. Res., 95, 9585–9610, 1990.

Worthington, L. V.: An attempt to measure the volume transport of Norwegian Sea overflow water through the Denmark Strait, Deep-Sea Res., 16, supplement, 421–432, 1969.

2.3 Paper III: Intense mixing of the Faroe Bank Channel overflow

GEOPHYSICAL RESEARCH LETTERS, VOL. 37, L02604, doi:10.1029/2009GL041924, 2010

Intense mixing of the Faroe Bank Channel overflow

Ilker Fer,[1,2] Gunnar Voet,[3] Knut S. Seim,[4] Bert Rudels,[5,6] and Katrin Latarius[3]

Received 25 November 2009; revised 29 December 2009; accepted 5 January 2010; published 29 January 2010.

[1] The continuous, swift flow of cold water across the sill of the Faroe Bank Channel, the deepest passage from the Nordic Seas to the North Atlantic Ocean, forms a bottom-attached dense plume (overflow). The amount and distribution of entrainment and mixing that the overflow encounters during its descent influence the ventilation of the deep North Atlantic, however, remain poorly known due to lack of direct measurements. Using the first direct turbulence measurements, we describe the dynamic properties and mixing of the overflow plume as it descends toward the Iceland Basin. The vigorously turbulent plume is associated with intense mixing and enhanced turbulent dissipation near the bottom and at the plume-ambient interface, but with a quiescent core. Our measurements show a pronounced transverse circulation consistent with rotating plume dynamics, a strong lateral variability in entrainment velocity, and a vertical structure composed of order 100 m thick stratified interface and comparably thick well-mixed bottom boundary layer with significant transport and entrainment. **Citation:** Fer, I., G. Voet, K. S. Seim, B. Rudels, and K. Latarius (2010), Intense mixing of the Faroe Bank Channel overflow, *Geophys. Res. Lett.*, *37*, L02604, doi:10.1029/2009GL041924.

1. Introduction

[2] The export of cold, dense water from the Norwegian Sea through the Faroe Bank Channel (FBC, Figure 1) into the sub-polar North Atlantic accounts for about one third of the total overflow from the Nordic Seas [*Hansen and Østerhus*, 2007]. The FBC overflow, a bottom-attached gravity current, descends the sloping topography under the combined influence of pressure gradient, bottom friction and the Earth's rotation, and mixes with overlying water [*Saunders*, 2001; *Mauritzen et al.*, 2005]. The latter determines the end-product properties associated with the source water and needs to be properly represented in climate models for credible climate projections [*Legg et al.*, 2009]. Despite the importance of mixing of the FBC overflow, no previous measurements of turbulence have been available. Motivated by this lack of measurements we conducted such a survey in June 2008.

[1]Geophysical Institute, University of Bergen, Bergen, Norway.
[2]Bjerknes Centre for Climate Research, Bergen, Norway.
[3]Institute of Oceanography, University of Hamburg, Hamburg, Germany.
[4]Department of Marine Technology, Norwegian University of Science and Technology, Trondheim, Norway.
[5]Department of Physics, University of Helsinki, Helsinki, Finland.
[6]Finnish Meteorological Institute, Helsinki, Finland.

0094-8276/10/2009GL041924$05.00

2. Measurements and Data

[3] The obtained data set includes vertical profiles of hydrography and velocity from 63 casts with a conductivity-temperature-depth (CTD, SBE911+) package equipped with down and uplooking lowered acoustic Doppler current profilers (LADCPs, 300 kHz Workhorse), and of turbulence profiles from 90 casts with a vertical microstructure profiler (VMP, Rockland Sci. Int.). The VMP is equipped with accurate CTD sensors and a pair of microstructure shear probes used for measuring the dissipation rate of turbulent kinetic energy (ε). Turbulent shear is sampled at 512 Hz at a profiling speed of 0.6 m s^{-1}. Stations are occupied along the path of the overflow plume and along six sections starting from the sill crest (section A) to about 120 km downstream (section F, Figure 1a).

3. Technical Details

3.1 Currents, Dissipation Rate, and Eddy Diffusivity

[4] The velocity profile is calculated as 4 m vertical averages using the inverse method [*Visbeck*, 2002] constrained by accurate shipboard navigation and bottom tracking by the LADCP, and detided using a barotropic tidal model [*Egbert et al.*, 1994] for the European Shelf at 1/30° resolution. Tidal velocity is within 3 to 34% (18% on the average) of the maximum velocity at a given station.

[5] The profiles of ε are produced as 1 m vertical averages to a noise level of 10^{-10} W kg^{-1} [*Fer*, 2006]. The diapycnal eddy diffusivity is calculated using three different formulations: First, an upper limit is obtained from $K_\rho = 0.2\varepsilon N^{-2}$ [*Osborn*, 1980] assuming 17% mixing efficiency. $N = [-g/\rho(\partial\rho/\partial z)]^{1/2}$ is the buoyancy frequency, g is the gravitational acceleration, and ρ is density. Second, we use $K_\rho = 2\nu(\varepsilon / \nu N^2)^{1/2}$ [*Shih et al.*, 2005], suggested for $\varepsilon / \nu N^2 > 100$, valid for our data ($\nu$ is the viscosity). This formulation, inferred from direct numerical simulation results, has been supported by field data [*Fer and Widell*, 2007]. Third, we use a gradient Richardson number (Ri) dependent mixing efficiency with the range of parameters validated against microstructure measurements [*Peters and Baumert*, 2007]. $\mathrm{Ri} = N^2/S^2$, where S is the shear. In all calculations, N is inferred from 4 m vertical gradients of sorted σ_θ (potential density referenced to nil pressure) profiles. The vertical scale is chosen to be consistent with shear calculations and the sorting approximates the background stratification against which the turbulence works.

3.2 Plume Properties and Stress

[6] The density anomaly, ρ', is obtained as deviations from an exponential background σ_θ profile fitted to observations excluding the plume. Velocity profiles are rotated into streamwise (u) and transverse (v, positive to the right of u) components with respect to the direction of the maximum

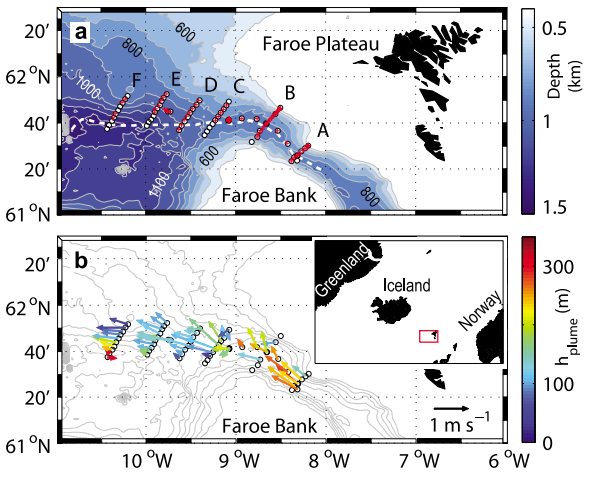

Figure 1. (a) Bathymetric contours drawn at 100 m intervals starting with 400 m, together with the thalweg (deepest point of the channel, white dashed line), sampling stations (CTD-LADCP, circles, and VMP, red crosses) and sections A to F. (b) Overflow velocity (arrows) averaged over h_{plume} (color). The salient features of the plume velocity and thickness are described in section 4. The inset shows the experiment location (red).

velocity (u_{nose}) in the bottom 200 m. The depth of the plume interface z_i and plume thickness h_{plume} are inferred from the $\sigma_\theta = 27.65$ kg m^{-3} isopycnal [*Mauritzen et al.*, 2005; *Girton et al.*, 2006]. The well-mixed bottom layer (BL) thickness is estimated as the height above bottom (HAB) where the density difference from the bottommost value exceeds 0.01 kg m^{-3}. The stratified interfacial layer (IL) is defined as the layer between the top of BL and the depth above the interface where $\partial\sigma_\theta/\partial z$ first drops below 5×10^{-4} kg m^{-4}. These thresholds robustly delineate the BL and IL. The calculation of integral plume properties and density-anomaly-weighted averages follows *Girton and Sanford* [2003]. The internal Froude number is calculated in two ways: from integral plume properties of each section using $\mathrm{Fr} = U/\sqrt{g'H}$ and using a two-layer formulation devised for transverse variations in velocity [*Pratt*, 2008]. In the former method g' is the reduced gravity, $H = A/(2W_{0.5})$ is the mean plume thickness for a section with area A and plume "half-width" $W_{0.5}$ [*Girton and Sanford*, 2003], and $U = Q_p/A$, using the section-integrated plume volume transport Q_p.

[7] The bottom shear stress, $\tau_b = \rho u_*^2$, is estimated using the friction velocity u_* from the slope of a linear fit of u against the log of HAB, assuming law of the wall (LOW). A series of fits is made for each profile, starting with 3 data points (12 m) and increasing to a maximum of BL thickness. The value with the least error, inferred from goodness of the fit, is chosen for analysis. The Ekman number $\mathrm{Ek} = u_*^2/fuh_{plume}$ and the drag coefficient $C_D = u_*^2/u_{nose}^2$ are obtained. Stress at the plume-ambient interface is estimated assuming a balance between the shear production, the dissipation rate, and the resulting buoyancy flux (0.2ε), as $\tau_i = 1.2\bar{\varepsilon}/(\rho du/dz)$, where overbars denote averaging over the interface thickness.

4. Results and Discussion

[8] The overflow plume descends the channel and the slope of the Iceland-Faroe Ridge with a typical speed of 0.5 – 1 m s^{-1}, reaching a maximum velocity of 1.35 m s^{-1} at section C (Figure 1b). Plume thickness averaged over stations is $h_{\mathrm{plume}} = 160 \pm 70$ m ($\pm$ 1 standard deviation, σ). Mean overflow thickness (H) inferred from section-integrated properties is between 110 m (section E) and 350 m (section B). All sections, however, show significant lateral variability (Figure 2).

[9] The vertical structure of the overflow is composed of a 70 ± 35 m thick well-mixed BL, overlaid by a 120 ± 60 m thick IL. With the caveat that the section-averaged transports are not synoptic with respect to variability on tidal and subtidal scales [*Geyer et al.*, 2006], the overflow is about equally distributed between the BL (0.9 ± 0.1 Sv, 1 Sv $\equiv 10^6$ m^3 s^{-1}) and the IL (1 ± 0.3 Sv). The presence of a thick IL was also observed at the Red Sea [*Peters et al.*, 2005], the Denmark Strait [*Girton and Sanford*, 2003], and the Mediterranean

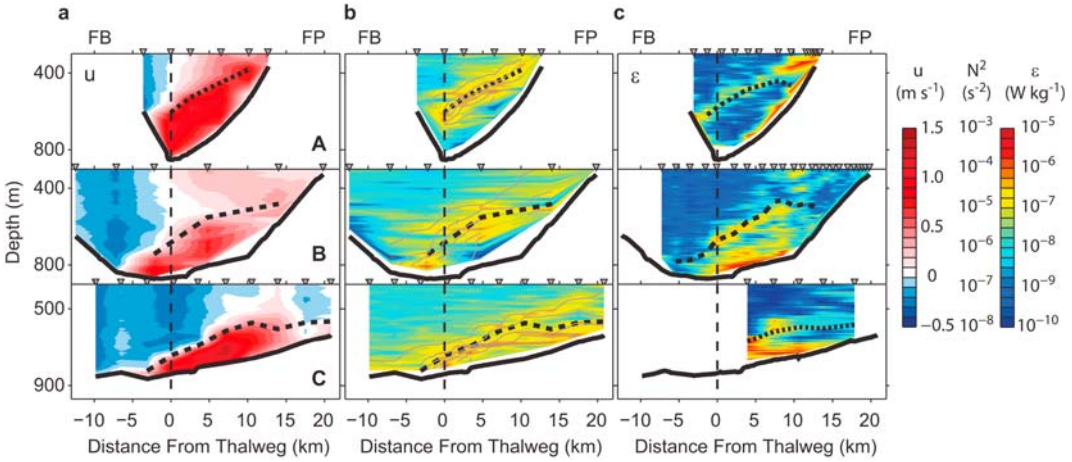

Figure 2. Contours of (a) downchannel velocity, u, (b) stratification, N^2 (color), and σ_θ at 0.1 kg m^{-3} intervals (gray), and (c) dissipation rate, ε, for sections A to C. Locations of the stations (triangles), the Faroe Bank (FB), and the Faroe Plateau (FP) are indicated. Dashed curves delineate the plume interface ($\sigma_\theta = 27.65$ kg m^{-3}).

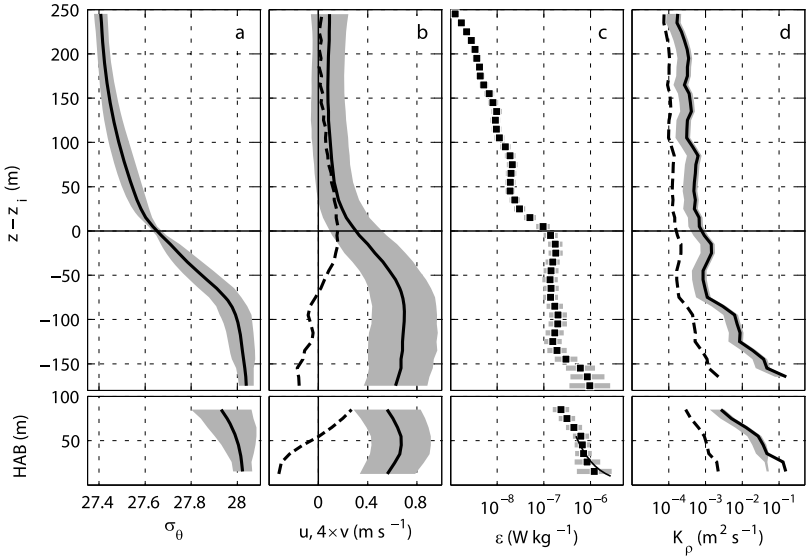

Figure 3. Survey averaged profiles of (a) σ_θ ($\pm$ 1σ, gray shading), (b) downchannel, u (solid line, $\pm$1σ, gray shading), and cross-channel, v (dashed line, multiplied by 4 for clarity), component of the velocity, (c) dissipation rate, ε (95% confidence limits, gray bars), and (d) eddy diffusivity, K_ρ, using *Osborn* [1980] (solid line), *Peters and Baumert* [2007] (gray), and *Shih et al.* [2005] (dashed line). Profiles are averaged in 10-m vertical bins referenced to (top) the interface depth, z_i, and to (bottom) bottom (HAB). Thin line in Figure 3c (bottom) is fit to LOW ($\varepsilon = u_*^3 / 0.4z$) in the bottom 55 m yielding u_* = 2.2 cm s^{-1} (τ_b = 0.5 Pa).

[*Price et al.*, 1993] outflow plumes, and suggests that bulk parameterization of entrainment [*Legg et al.*, 2009] devised for gravity currents with relatively thin interface may not be adequate.

[10] The velocity maximum is typically located deeper than the interface and is associated with weak ε as a result of weak shear production of turbulent kinetic energy (see the quiescent core at section A, Figure 2). This quiescent layer is present at all sections. The average thickness of layer with $\varepsilon < 10^{-8}$ W kg^{-1} below the interface is 40 m for the core stations and varies between 15 m (section B) and 60 m (section A). In the BL and the IL ε is exceptionally large, reaching 10^{-5} W kg^{-1} (Figure 2c). Typically BL is 20–70 m thicker than the bottom layer with enhanced dissipation. The vigorous turbulence near the bottom is due to stirring by the bottom shear stress. Enhanced mixing at the stratified and highly-sheared IL where Ri < 1 can be due to coexisting shear instabilities and internal wave-turbulence transition [*Baumert and Peters*, 2009] and vertical transport of turbulence [*Umlauf*, 2009]. The internal structure of turbulence in the FBC overflow is reminiscent of the observations in the Baltic Sea [*Umlauf et al.*, 2007], particularly the quiescent central region, and the asymmetry in ε at the sill section with enhanced ε where the interface intersects the Faroe Plateau slope (Figure 2b). A wedge-shaped interface, related to the secondary flow in the IL, as discussed by *Umlauf and Arneborg* [2009], is not resolved in our data set.

[11] Survey-averaged profiles are constructed for plume stations in 10-m thick bins relative to the interface and relative to the bottom (Figure 3). Due to variable interface depth and plume thickness, the average profiles cannot be combined (i.e., the lower part of Figure 3 (top) will not be consistent with Figure 3 (bottom) due to averaging). Dissipation rates, exceeding 10^{-7} W kg^{-1} in the plume, increase by one order of magnitude as the bottom is approached, consistent with LOW (thin line in Figure 3c). The mixing efficiency implied by the models of *Shih et al.* [2005] and *Peters and Baumert* [2007] differ significantly, particularly in weakly stratified layers (Figure 3d). The shear is strong throughout the IL, but the maximum in ε apparent in Figure 2c near the interface is smoothed out as a result of averaging. When calculated using the density and velocity profiles in Figure 3, Ri < 1 between 20 m above and 40 m below the interface, with a minimum value of 0.6 at 15 m below the interface. Ri < 1 in the entire BL with Ri < 0.25 in the bottommost 25 m. Low Ri in the BL is due to a combination of weak stratification and mean shear of the logarithmic velocity profile, whereas that in the IL is due to strong shear across the strongly stratified interface. Previous observations from a mooring near the FBC sill show frequent occurrence of low Ri in the IL, modulated by tidal and inertial flows [*Saunders*, 2001].

[12] The transverse velocity, v (Figure 3b), has a vertical structure consistent with the rotating gravity current dynamics [*Umlauf and Arneborg*, 2009]. Water in the IL is transported to the right, looking downstream (a transverse geostrophic transport due to the downchannel tilt of the plume interface), and water in the BL is transported to the left, consistent with an Ekman bottom boundary layer, leading to a flattening and broadening of the plume. Integrated across the IL and BL, the transverse flow approximately balances with 5 m^2 s^{-1} in the IL, −3.3 m^2 s^{-1} in the BL (−4.5 m^2 s^{-1} if an unresolved 15-m thick bottom layer with v = −8 cm s^{-1}, the bottommost average value, is included).

[13] The FBC overflow can be characterized by Fr between 0.5 and 1 and by Ek between 0.05 and 0.2; that is, the plume is thicker than the frictional boundary layer (Figure 4). In contrast to the Red Sea outflow [*Peters et al.*, 2005], the FBC overflow is significantly diluted in the BL. The buoy-

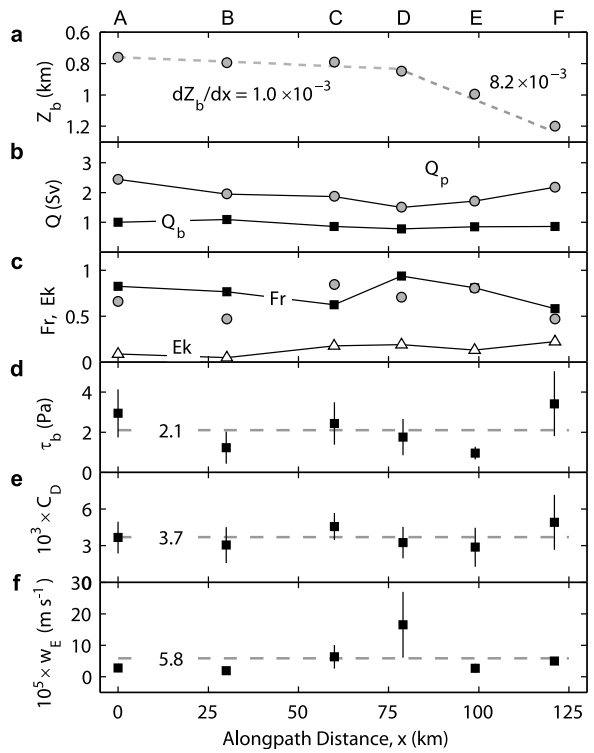

Figure 4. Downstream evolution of section-averaged properties. (a) Mass-anomaly-weighted depth of the plume, Z_b [*Girton and Sanford*, 2003]. Linear fits between sections A-D and D-F yield a descent rate of 1 m and 8.2 m per km along the path, respectively (dashed lines). (b) Volume transport in the overflow plume (Q_p, circles) and in the BL (Q_b, squares). (c) Froude number (Fr, following *Pratt* [2008], squares; and using section integral properties, circles), and Ekman number, Ek (triangles). (d) Bottom stress, τ_b, and (e) drag coefficient, C_D, from LADCP profiles, and (f) the entrainment velocity, w_E, from ε [*Arneborg et al.*, 2007]. The survey-averaged values are indicated by dashed lines. Error bars are $\sigma_e = \sigma\sqrt{n-1}$, where σ is the standard deviation and n is the number of plume stations in a section.

ancy averaged in BL (IL) increases by 1.4×10^{-3} m s^{-2} (5×10^{-4} m s^{-2}) on the first 80 km. This suggests entrainment into the BL, through, e.g., internal mixing in the plume, entrainment as a result of the transverse circulation, or lateral entrainment due to stirring by mesoscale eddies. The volume transport, however, is nearly constant in the BL (Q_b in Figure 4b), counterintuitive to the expected increase due to entrainment. Detrainment [*Baines*, 2005] might explain the lack of increase in Q_b. Nevertheless, interpreted together with the Red Sea outflow observations which show a similar vertical density structure but no dilution in BL, we suggest that the transverse circulation supplying the warmer interface water into the Ekman layer may cause the dilution in the BL. Q_b remains nearly constant due to the approximate lateral balance of the transverse circulation; that is, water entrained in the BL is transported back to the IL.

[14] Section-averaged K_ρ varies between $(2 - 10) \times 10^{-4}$ m^2 s^{-1} in the IL and between $(10 - 320) \times 10^{-4}$ m^2 s^{-1} in the BL, consistent with heat-budget considerations [*Saunders*, 1990; *Duncan et al.*, 2003]. The entrainment velocity, w_E, calculated from ε [*Arneborg et al.*, 2007] (assuming 17% mixing efficiency) varies by one order of magnitude laterally in each section (except section F). Section-averaged w_E increases fivefold from 3×10^{-5} m s^{-1} at the sill to 1.7×10^{-4} m s^{-1} at section D (Figure 4f) where Fr is accordingly at its highest, close to unity. The entrainment parameter, w_E/U, increases by one order of magnitude from 3.8×10^{-5} to 3.3×10^{-4}. The largest mixing and entrainment rates are observed at section D in the vicinity of the hot-spot of mixing identified by *Mauritzen et al.* [2005]. Detailed analysis of earlier observations suggests that FBC overflow is hydraulically controlled [*Girton et al.*, 2006] with the critical section (i.e., Fr = 1) located between 20 – 90 km down sill, comparing well with Fr $\approx$ 1 at our section D. While the overflow volume transport, Q_p, increases downstream of section D (consistent with enhanced entrainment), Q_p decreases between sections A and D. The mesoscale variability of the overflow makes the comparison of single sections complex.

[15] The overflow plume descends the slope as a result of bottom friction. The descent rate is relatively small between sections A-D and increases farther downstream (Figure 4a), comparable to that of the Denmark Strait plume [*Girton and Sanford*, 2003], but significantly larger than 2.5 m km^{-1} predicted by *Killworth* [2001]. The bottom stress $\tau_b = 2.1 \pm 0.4$ Pa, corresponding to a drag coefficient of $C_D = (3.7 \pm 0.4) \times 10^{-3}$, is large throughout the channel, and in the range of previous observations [*Mauritzen et al.*, 2005]. When tides are included, the survey-mean C_D increases by 20%. The average bottom stress inferred from the velocity profiles is about four times larger than that estimated from ε measurements near the bottom (Figure 3c), similar to observations from diverse sites and can be attributed to, e.g., the form drag. The stress at the IL is relatively weak, $\tau_i = 0.05 \pm 0.02$ Pa. Inferred from the balance of buoyancy, total drag (due to τ_b and τ_i) and Coriolis force acting on a slab of plume [*Girton and Sanford*, 2003], the total stress to account for the observed descent rates is 0.9 (sections A-D) and 4.9 Pa (D-F). Recalling that $\tau_b \approx \tau_b + \tau_i$ in our data set, Figure 4d does not show this trend, suggesting that the observed descent rates cannot be described by this simple force balance.

5. Concluding Remarks

[16] Our observations reveal the anatomy and mixing processes of the FBC overflow plume and add to our understanding of a highly sheared and stratified gravity current in a rotating system. The overflow plume is characterized by strong lateral variability in entrainment and mixing with a significant vertical structure including an about 100 m thick strongly-stratified interfacial layer. A transverse circulation actively dilutes the bottom layer of the plume. Neither the bulk entrainment parameterizations, mainly devised for non-rotating, two-layer gravity current plume dynamics, nor the traditional turbulence closure models will be adequate in representing mixing of the dense overflow plume downstream of the FBC sill.

[17] **Acknowledgments.** This study is funded by the Research Council of Norway, through Bipolar Atlantic Thermohaline Circulation (BIAC) project. Comments from an anonymous reviewer, L. Umlauf, H. Peters,

H. Z. Baumert, and T. Özgökmen are greatly appreciated. This is publication no. A 271 from the Bjerknes Centre for Climate Research.

References

Arneborg, L., V. Fiekas, L. Umlauf, and H. Burchard (2007), Gravity current dynamics and entrainment: A process study based on observations in the Arkona Basin, *J. Phys. Oceanogr.*, *37*, 2094–2113, doi:10.1175/JPO3110.1.

Baines, P. G. (2005), Mixing regimes for the flow of dense fluid down slopes into stratified environments, *J. Fluid Mech.*, *538*, 245–267, doi:10.1017/S0022112005005434.

Baumert, H. Z., and H. Peters (2009), Turbulence closure: Turbulence, waves and the wave-turbulence transition—Part 1: Vanishing mean shear, *Ocean Sci.*, *5*, 47–58.

Duncan, L. M., H. L. Bryden, and S. A. Cunningham (2003), Friction and mixing in the Faroe Bank Channel outflow, *Oceanol. Acta*, *26*, 473–486, doi:10.1016/S0399-1784(03)00042-2.

Egbert, G. D., A. F. Bennett, and M. G. G. Foreman (1994), TOPEX/POSEIDON tides estimated using a global inverse model, *J. Geophys. Res.*, *99*, 24,821–24,852, doi:10.1029/94JC01894.

Fer, I. (2006), Scaling turbulent dissipation in an Arctic fjord, *Deep Sea Res., Part II*, *53*, 77–95, doi:10.1016/j.dsr2.2006.01.003.

Fer, I., and K. Widell (2007), Early spring turbulent mixing in an ice-covered Arctic fjord during transition to melting, *Cont. Shelf Res.*, *27*, 1980–1999, doi:10.1016/j.csr.2007.04.003.

Geyer, F., S. Østerhus, B. Hansen, and D. Quadfasel (2006), Observations of highly regular oscillations in the overflow plume downstream of the Faroe Bank Channel, *J. Geophys. Res.*, *111*, C12020, doi:10.1029/2006JC003693.

Girton, J. B., and T. B. Sanford (2003), Descent and modification of the overflow plume in the Denmark Strait, *J. Phys. Oceanogr.*, *33*, 1351–1364, doi:10.1175/1520-0485(2003)033<1351:DAMOTO>2.0.CO;2.

Girton, J. B., L. J. Pratt, D. A. Sutherland, and J. F. Price (2006), Is the Faroe Bank Channel overflow hydraulically controlled? *J. Phys. Oceanogr.*, *36*, 2340–2349, doi:10.1175/JPO2969.1.

Hansen, B., and S. Østerhus (2007), Faroe Bank Channel overflow 1995–2005, *Prog. Oceanogr.*, *75*, 817–856.

Killworth, P. D. (2001), On the rate of descent of overflows, *J. Geophys. Res.*, *106*, 22,267–22,275, doi:10.1029/2000JC000707.

Legg, S., et al. (2009), Improving oceanic overflow representation in climate models: The Gravity Current Entrainment Climate Process Team, *Bull. Am. Meteorol. Soc.*, *90*, 657–670, doi:10.1175/2008BAMS2667.1.

Mauritzen, C., J. F. Price, T. B. Sanford, and D. Torres (2005), Circulation and mixing in the Faroese Channels, *Deep Sea Res., Part I*, *52*, 883–913, doi:10.1016/j.dsr.2004.11.018.

Osborn, T. R. (1980), Estimates of the local rate of vertical diffusion from dissipation measurements, *J. Phys. Oceanogr.*, *10*, 83–89, doi:10.1175/1520-0485(1980)010<0083:EOTLRO>2.0.CO;2.

Peters, H., and H. Z. Baumert (2007), Validating a turbulence closure against estuarine microstructure measurements, *Ocean Modell.*, *19*, 183–203, doi:10.1016/j.ocemod.2007.07.002.

Peters, H., W. E. Johns, A. S. Bower, and D. M. Fratantoni (2005), Mixing and entrainment in the Red Sea outflow plume. Part I: Plume structure, *J. Phys. Oceanogr.*, *35*, 569–583, doi:10.1175/JPO2679.1.

Pratt, L. J. (2008), Critical conditions and composite Froude numbers for layered flow with transverse variations in velocity, *J. Fluid Mech.*, *605*, 281–291, doi:10.1017/S002211200800150X.

Price, J. F., et al. (1993), Mediterranean outflow and mixing dynamics, *Science*, *259*, 1277–1282, doi:10.1126/science.259.5099.1277.

Saunders, P. M. (1990), Cold outflow from the Faroe Bank Channel, *J. Phys. Oceanogr.*, *20*, 29–43, doi:10.1175/1520-0485(1990)020<0029:COFTFB>2.0.CO;2.

Saunders, P. M. (2001), The dense northern overflows, in *Ocean Circulation and Climate,* edited by G. Siedler et al., pp. 401–417, Academic, San Diego, Calif.

Shih, L. H., J. R. Koseff, G. N. Ivey, and J. H. Ferziger (2005), Parameterization of turbulent fluxes and scales using homogeneous sheared stably stratified turbulence simulations, *J. Fluid Mech.*, *525*, 193–214, doi:10.1017/S0022112004002587.

Umlauf, L. (2009), The description of mixing in stratified layers without shear in large-scale ocean models, *J. Phys. Oceanogr.*, *39*, 3032–3039, doi:10.1175/2009JPO4006.1.

Umlauf, L., and L. Arneborg (2009), Dynamics of rotating shallow gravity currents passing through a channel. Part II: Analysis, *J. Phys. Oceanogr.*, *39*, 2402–2416, doi:10.1175/2009JPO4164.1.

Umlauf, L., L. Arneborg, H. Burchard, V. Fiekas, H. U. Lass, V. Mohrholz, and H. Prandke (2007), Transverse structure of turbulence in a rotating gravity current, *Geophys. Res. Lett.*, *34*, L08601, doi:10.1029/2007GL029521.

Visbeck, M. (2002), Deep velocity profiling using lowered acoustic Doppler current profilers: Bottom track and inverse solutions, *J. Atmos. Oceanic Technol.*, *19*, 794–807, doi:10.1175/1520-0426(2002)019<0794:DVPULA>2.0.CO;2.

I. Fer, Geophysical Institute, University of Bergen, N-5007 Bergen, Norway.

K. Latarius and G. Voet, Institute of Oceanography, University of Hamburg, D-20146 Hamburg, Germany.

B. Rudels, Department of Physics, University of Helsinki, FI-00561 Helsinki, Finland.

K. S. Seim, Department of Marine Technology, Norwegian University of Science and Technology, NO-7491 Trondheim, Norway.

Bibliography

Baehr, J., H. Haak, S. Alderson, S. Cunningham, J. Jungclaus and J. Marotzke. Timely Detection of Changes in the Meridional Overturning Circulation at 26° N in the Atlantic. *Journal of Climate*, **20**, 5827–5841, 2007.

Blindheim, J. and S. Østerhus. *The Nordic Seas: An Integrated Perspective*, volume 158 of *Geophys. Monogr. Ser.*, chapter The Nordic Seas, Main Oceanographic Features, pages 11–37. AGU, Washington DC, 2005.

Borenäs, K. and P. Lundberg. On the Deep-Water Flow Through the Faroe Bank Channel. *Journal of Geophysical Research*, **93**(C2), 1281–1292, 1988.

Borenäs, K. and P. Lundberg. The Faroe-Bank Channel deep-water overflow. *Deep-Sea Research II*, **51**, 335–350, 2004.

Bruce, J. G. Eddies southwest of the Denmark Strait. *Deep-Sea Research Part I*, **42**, 13–29, 1995.

Bryden, H., H. Longworth and S. Cunningham. Slowing of the Atlantic meridional overturning circulation at 25°N. *Nature*, **438**, 655–657, 2005.

Carmack, E. and K. Aagaard. On the Deep Water of the Greenland Sea. *Deep-Sea Research*, **20**, 687–715, 1973.

Cenedese, C., J. A. Whitehead, T. A. Ascarelli and M. Ohiwa. A Dense Current Flowing down a Sloping Bottom in a Rotating Fluid. *Journal of Physical Oceanography*, **34**, 188–203, 2004.

Cunningham, S., T. Kanzow, D. Rayner, M. Baringer, W. Johns, J. Marotzke, H. Longworth, E. Grant, J.-M. Hirschi, L. Beal, C. Meinen and H. Bryden. Temporal Variability of the Atlantic Meridional Overturning Circulation at 26.5°N. *Science*, **317**(5840), 935–938, 2007.

Dickson, B., S. Dye, S. Jónsson, A. Köhl, A. Macrander, M. Marnela, J. Meincke, S. Olsen, B. Rudels, H. Valdimarsson and

G. Voet. *Arctic-Subarctic Ocean Fluxes*, chapter The Overflow Flux West of Iceland: Variability, Origins and Forcing, pages 443–474. Springer, 2008.

Dickson, R. R. and J. Brown. The production of North Atlantic Deep Water: Sources, rates, and pathways. *Journal of Geophysical Research*, **99**, 12319–12341, 1994.

Dietrich, G. Überströmung des Island-Färöer-Rückens in Bodennähe nach Beobachtungen mit dem Forschungsschiff "Anton Dohrn" 1955/56. *Deutsche Hydrographische Zeitschrift*, **9**(2), 78–89, 1956.

Duncan, L., H. Bryden and S. Cunningham. Friction and mixing in the Faroe Bank Channel outflow. *Oceanologica Acta*, **26**, 473–486, 2003.

Ezer, T. Topographic influence on overflow dynamics: Idealized numerical simulations and the Faroe Bank Channel overflow. *Journal of Geophysical Research*, **111**, C02002, 2006.

Fer, I., G. Voet, K. Seim, B. Rudels and K. Latarius. Intense mixing of the Faroe Bank Channel overflow. *Geophysical Research Letters*, **37**, L02604, 2010.

Ganachaud, A. and C. Wunsch. Improved estimates of global ocean circulation, heat transport and mixing from hydrographic data. *Nature*, **408**, 453–457, 2000.

Gascard, J.-C. and K. Mork. *Arctic-Subarctic Ocean Fluxes*, chapter Climatic Importance of Large-Scale and Mesoscale Circulation in the Lofoten Basin Deduced from Lagrangian Observations, pages 131–143. Springer, 2008.

Geyer, F., S. Østerhus, B. Hansen and D. Quadfasel. Observations of highly regular oscillations in the overflow plume downstream of the Faroe Bank Channel. *Journal of Geophysical Research*, **111**, 2006JC003693, 2006.

Gill, A. *Atmosphere-Ocean Dynamics*, volume 30 of *International Geophysics Series*. Academic Press, London, 1982.

Girton, J., L. Pratt, D. Sutherland and J. Price. Is the Faroe Bank Channel overflow hydraulically controlled? *Journal of Physical Oceanography*, **36**, 2340–2349, 2006.

Girton, J. B. and T. B. Sanford. Descent and Modification of the Overflow Plume in the Denmark Strait. *Journal of Physical Oceanography*, **33**, 1351–1364, 2003.

Hansen, B. and J. Meincke. Eddies and meanders in the Iceland-Faroe Ridge area. *Deep-Sea Research*, **26A**, 1067–1082, 1979.

Hansen, B. and S. Østerhus. North Atlantic - Nordic Seas exchanges. *Progress in Oceanography*, **45**, 109–208, 2000.

Hansen, B. and S. Østerhus. Faroe Bank Channel overflow 1995-2005. *Progress in Oceanography*, **75**, 817–856, 2007.

Hansen, B., S. Østerhus, D. Quadfasel and W. Turrell. Already the Day After Tomorrow? *Science*, **305**, 953–954, 2004.

Hansen, B., S. Østerhus, W. Turrell, S. Jónsson, H. Valdimarsson, H. Hátún and S. Olsen. *Arctic-Subarctic Ocean Fluxes*, chapter The Inflow of Atlantic Water, Heat, and Salt to the Nordic Seas Across the Greenland-Scotland Ridge, pages 15–43. Springer, 2008.

Helland-Hansen, B. and F. Nansen. The Norwegian Sea: Its Physical Oceanography based on Norwegian Researches. *Report on Norwegian Fishery and Marine Investigations*, **11**(2), 390 pp. + 25 plates, 1909.

Hermann, F. The T-S diagram analysis of the water masses over the Iceland-Faroe Ridge and in the Faroe Bank Channel. *Rapports et Procés-Verbaux des Réunions - Conseil Iinternational pour l'Exploration de la Mer*, **157**, 139–149, 1967.

Høyer, J. L. and D. Quadfasel. Detection of deep overflows with satellite altimetry. *Geophysical Research Letters*, **28**, 1611–1614, 2001.

Isachsen, P., J. LaCasce, C. Mauritzen and S. Häkkinen. Wind-driven variability of the large-scale recirculating flow in the Nordic Seas and Arctic Ocean. *Journal of Physical Oceanography*, **33**, 2534–2550, 2003.

Isachsen, P., C. Mauritzen and H. Svendsen. Dense water formation in the Nordic Seas as diagnosed from sea surface buoyancy fluxes. *Deep-Sea Research I*, **54**, 22–41, 2007.

Jakobsen, P., M. Ribergaard, D. Quadfasel, T. Schmith and C. Hughes. Near-surface circulation in the northern North Atlantic is inferred from Lagrangian drifters: variability from the mesoscale to interannual. *Journal of Physical Oceanography*, **108**(C8), 3251, 2003.

Jiang, L. and R. W. Garwood. Three-Dimensional Simulations of Overflows on Continental Slopes. *Journal of Physical Oceanography*, **26**, 1214–1233, 1996.

Jungclaus, J. H., J. Hauser and R. H. Käse. Cyclogenesis in the Denmark Strait Overflow Plume. *Journal of Physical Oceanography*, **31**, 3214–3229, 2001.

Käse, R. A Riccati model for Denmark Strait overflow variability. *Geophysical Research Letters*, **33**, L21S09, 2006.

Käse, R. and A. Oschlies. Flow through Denmark Strait. *Journal of Geophysical Research*, **105**, 28527–28546, 2000.

Käse, R. H., J. B. Girton and T. B. Sanford. Structure and variability of the Denmark Strait Overflow: Model and observations. *Journal of Geophysical Research*, **108**, 12–1–12–15, 2003.

Knudsen, M. *Den Danske Ingolf-expedition*, chapter Hydrografi, pages 21–154. København, 1898.

Köller, M., R. Käse and P. Herrmann. Interannual to multidecadal variability and predictability of North Atlantic circulation in a coupled earth system model with parametrized hydraulics. *Tellus*, **62A**, 2010.

Kösters, F., R. Käse, A. Schmittner and P. Herrmann. The effect of Denmark Strait overflow on the Atlantic meridional overturning circulation. *Geophysical Research Letters*, **32**, L04602, 2005.

Krauss, W. A note on overflow eddies. *Deep-Sea Research I*, **43**, 1661–1667, 1996.

Krauss, W. and R. H. Käse. Eddy formation in the Denmark Strait overflow. *Journal of Geophysical Research*, **103**, 15525–15538, 1998.

Latarius, K. and D. Quadfasel. Seasonal to interannual variability of temperature and salinity in the Greenland Sea Gyre: heat and freshwater budgets. *Tellus*, **62A**, 2010.

Legg, S., B. Briegleb, Y. Chang, E. Chassignet, G. Danabasoglu, T. Ezer, A. Gordon, S. Griffies, R. Hallberg, L. Jackson, W. Large, T. Özgökmen, H. Peters, J. Price, U. Riemenschneider, W. Wu, X. Xu and J. Yang. Improving oceanic overflow representation in climate models: The Gravity Current Entrainment Climate Process Team. *Bulletin of the American Meteorological Society*, **90**(5), 657–670, 2009.

Macrander, A., R. Käse, U. Send, H. Valdimarsson and J. Steingrímur. Spatial and temporal structure of the Denmark Strait Overflow revealed by acoustic observations. *Ocean Dynamics*, **57**, 75–89, 2007.

Macrander, A., U. Send, H. Valdimarsson, S. Jónsson and R. H. Käse. Interannual changes in the overflow core from the Nordic Seas into the Atlantic Ocean through Denmark Strait. *Geophysical Research Letters*, **32**, L06606, 2005.

Mauritzen, C. Production of dense overflow waters feeding the North Atlantic across the Greenland-Scotland Ridge. Part 1: Evidence for a revised circulation scheme. *Deep-Sea Research Part I*, **43**, 769–806, 1996.

Mauritzen, C., J. Price, T. Sanford and D. Torres. Circulation and mixing in the Faroese Channels. *Deep-Sea Research Part I*, **52**, 883–913, 2005.

Meehl, G., T. Stocker, W. Collins, P. Friedlingstein, A. Gaye, J. Gregory, A. Kitoh, R. Knutti, J. Murphy, A. Noda, S. Raper, I. Watterson, A. Weaver and Z.-C. Zhao. *Climate Change 2007: The Physical Science Basis. Contribution of Working Group I to the Fourth Assessment Report of the Intergovernmental Panel on Climate Change*, chapter Global Climate Projections, pages 747–845. Cambridge University Press, Cambridge, United Kingdom and New York, NY, USA, 2007.

Meincke, J. *Structure and Development of the Greenland-Scotland Ridge*, chapter The modern current regime across the Greenland-Scotland Ridge, pages 637–650. Plenum, 1983.

Mork, K. and O. Skagseth. *The Nordic Seas: An Integrated Perspective*, volume 158 of *Geophys. Monogr. Ser.*, chapter Annual Sea Surface Height Variability in the Nordic Seas and Arctic Ocean estimated from simplified dynamics, pages 51–64. AGU, Washington DC, 2005.

Müller, T., F. Schott and G. Siedler. Observations of overflow on the Iceland Faeroe Ridge. *"Meteor" Forschungsergebnisse*, **A 15**, 49–55, 1974.

Nilsen, J., H. Hátún, K. Mork and H. Valdimarsson. The NISE Dataset. Technical Report 08-01, Faroese Fisheries Laboratory, Box 3051, Tórshavn, Faroe Islands, 2008.

Nøst, O. and P. Isachsen. The large-scale time-mean ocean circulation in the Nordic Seas and Arctic Ocean estimated from simplified dynamics. *Journal of Marine Research*, **61**, 175–210, 2003.

Olsen, S., B. Hansen, D. Quadfasel and S. Østerhus. Observed and modelled stability of overflow across the Greenland-Scotland ridge. *Nature*, **455**, 519–523, 2008.

Orvik, K., O. Skagseth and M. Mork. Atlantic inflow to the Nordic Seas: current structure and volume fluxes from moored current meters,

VM-ADCP and SeaSoar-CTD observations, 1995-1999. *Deep-Sea Research I*, **48**, 937–957, 2001.

Østerhus, S., T. Sherwin, D. Quadfasel and B. Hansen. *Arctic-Subarctic Ocean Fluxes*, chapter The Overflow Transport East of Iceland, pages 427–441. Springer, 2008.

Paka, V., B. Rudels, D. Quadfasel and V. Zhurbas. Turbulence measurements in strong bottom current zone in Denmark Strait (in russian). *Doklady Akademii Nauk - Geofizika*, **432**(1), 1–5, 2010.

Perkins, H., T. Hopkins, S.-A. Malmberg, P.-M. Poulain and A. Warn-Varnas. Oceanographic conditions east of Iceland. *Journal of Geophysical Research*, **103**(C10), 21531–21542, 1998.

Perkins, H., T. Sherwin and T. Hopkins. Amplification of Tidal Currents by Overflow on the Iceland-Faeroe Ridge. *Journal of Physical Oceanography*, **24**, 721–735, 1994.

Poulain, P.-M., A. Warn-Varnas and P. Niiler. Near-surface circulation of the Nordic seas as measured by Lagrangian drifters. *Journal of Geophysical Research*, **101**(C8), 18237–18258, 1996.

Price, J. and M. Baringer. Outflows and deep water production by marginal seas. *Progress in Oceanography*, **33**, 161–200, 1994.

Quadfasel, D. and R. H. Käse. *Ocean Circulation: Mechanisms and Impacts*, volume 173, chapter Present-Day Manifestation of the Nordic Seas Overflows, pages 75–89. Geophys. Monogr. Ser., AGU, Washington D.C., 2007.

Rahmstorf, S. The current climate. *Nature*, **421**, 699, 2003.

Rahmstorf, S. and A. Ganapolski. Long-term global warming scenarios computed with an efficient coupled climate model. *Climate Change*, **43**, 353–367, 1999.

Riemenschneider, U. and S. Legg. Regional simulations of the Faroe Bank Channel overflow in a level model. *Ocean Modelling*, **17**, 93–122, 2007.

Ross, C. K. Temperature - salinity characteristics of the "overflow" water in Denmark Strait during "OVERFLOW '73". *Rapports et Procés-Verbaux des Réunions - Conseil Iinternational pour l'Exploration de la Mer*, **185**, 111–119, 1984.

Rossby, T., M. Prater and H. Søiland. Pathways of inflow and dispersion of warm waters in the Nordic seas. *Journal of Geophysical Research*, **114**, C04011, 2009.

Rudels, B., P. Eriksson, H. Grönvall, R. Hietala and J. Launiainen. Hydrographic Observations in Denmark Strait in Fall 1997, and their Implications for the Entrainment into the Overflow Plume. *Geophysical Research Letters*, **26**, 1325–1328, 1999.

Saunders, P. *Ocean Circulation & Climate*, chapter The Dense Northern Overflows, pages 401–417. Academic Press, 2001.

Schmittner, A., M. Latif and B. Schneider. Model projections of the North Atlantic thermohaline circulation for the 21st century assessed by observations. *Geophysical Research Letters*, **32**, L23710, 2005.

Seager, R., D. Battisti, J. Yin, N. Gordon, N. Naik, A. Clement and M. Cane. Is the Gulf Stream responsible for Europe's mild winters? *Quarterly Journal of the Royal Meteorological Society*, **128**, 2563–2586, 2002.

Sherwin, T., C. Griffiths, M. Inall and W. Turrell. Quantifying the overflow across the Wyville Thomson Ridge into the Rockall Trough. *Deep-Sea Research I*, **55**, 396–404, 2008.

Smith, P. C. A streamtube model for bottom boundary currents in the ocean. *Deep-Sea Research*, **22**, 853–873, 1975.

Søiland, H., M. Prater and T. Rossby. Rigid topographic control of currents in the Nordic Seas. *Geophysical Research Letters*, **35**, L18607, 2008.

Solomon, S., D. Qin, M. Manning, Z. Chen, M. Marquis, K. Averyt, M. Tignor and H. Miller, editors. *Contribution of Working Group I to the Fourth Assessment Report of the Intergovernmental Panel on Climate Change*. Cambridge University Press, Cambridge, United Kingdom and New York, NY, USA, 2007.

Stommel, H. Thermohaline Convection with Two Stable Regimes of Flow. *Tellus*, **13**, 224–230, 1961.

Swift, J. The circulation of the Denmark Strait and Iceland-Scotland overflow waters in the North Atlantic. *Deep-Sea Research*, **31**, 1339–1355, 1984.

Swift, J., K. Aagaard and S.-A. Malmberg. The contribution of the Denmark Strait overflow to the deep North Atlantic. *Deep-Sea Research*, **27A**, 29–42, 1980.

Van Aken, H. and G. Becker. Hydrography and through-flow in the north-eastern North Atlantic Ocean: the NANSEN project. *Progress in Oceanography*, **38**, 297–346, 1996.

Voet, G. and D. Quadfasel. Entrainment in the Denmark Strait overflow plume by meso-scale eddies. *Ocean Science*, **6**, 301–310, 2010.

Voet, G., D. Quadfasel, K. Mork and H. Søiland. The mid-depth circulation of the Nordic Seas derived from profiling float observations. *Tellus*, **62A**, 2010.

Wessel, P. and W. Smith. Free software helps map and display data. *EOS Transactions AGU*, **72**, 441, 1991.

Whitehead, J. Topographic control of oceanic flows in deep passages and straits. *Reviews of Geophysics*, **36**, 423–440, 1998.

Whitehead, J., A. Leetmaa and R. Knox. Rotating hydraulics of strait and sill flows. *Geophysical Fluid Dynamics*, **6**, 101–125, 1974.

Wilkenskjeld, S. and D. Quadfasel. Response of the Greenland-Scotland overflow to changing deep water supply from the Arctic Mediterranean. *Geophysical Research Letters*, **32**, L21607, 2005.

Woodgate, R., E. Fahrbach and G. Rohardt. Structure and transports of the East Greenland Current at 75° N from moored current meters. *Journal of Geophysical Research*, **104**(C8), 18059–18072, 1999.

Acknowledgements

First and foremost I want to thank my supervisor Detlef Quadfasel for his outstanding support, constant guidance, and enlightening and inspiring discussions.

I want to thank my colleagues in our research group for stimulating discussions and a vivid research environment.

My position at the Institut für Meereskunde, Universität Hamburg was funded for three years by Deutsche Forschungsgemeinschaft (SFB 512 E2). An extension of half a year was financed through the Euro-Argo project by the European Commision.

The data used in this thesis were collected within the framework of several projects by the European Commission (ASOF, Euro-Argo, MERSEA, MOEN, THOR, VEINS), by the German Ministry of Education and Research (Nordatlantik Projekt) and by Deutsche Forschungsgemeinschaft (SFB 512). The hydrographic data in section 1.4.2 were provided by: The Marine Research Institute, Iceland; Institute of Marine Research, Norway; the Faroese Fisheries Laboratory; the Arctic and Antarctic Research Institute, Russia, and Geophysical Institute, University of Bergen, Norway, through the NISE project.

Many thanks to Ulrich Drübbisch, Andreas Welsch and all other technicians and sailors who do a great job in collecting oceanographic data.

Finally, I received great help during the final days of this thesis from Katrin Latarius, Matthias Köller and Olga Fischer.